

Doctoral Dissertation

博士論文

Development of a Microwave SQUID Multiplexer for a TES X-ray
Microcalorimeter Array for Future Astrophysical Observations

(将来の宇宙観測を目指した TES 型 X 線マイクロカロリメータアレイ読み出しのためのマイクロ波 SQUID マルチプレクサの開発)

A Dissertation Submitted for the Degree of Doctor of Philosophy
December 2019

令和元年12月博士(理学)申請

Department of Physics, Graduate School of Science,
The University of Tokyo

東京大学大学院理学系研究科物理学専攻

Yuki Nakashima

中島 裕貴

Acknowledgements

I have been supported by many people and learned a lot of things from them for these five years in ISAS/JAXA and AIST. I would like to take this opportunity to express my great appreciation to them.

My advisor Professor Noriko. Y. Yamasaki kindly led me to the right way in my thesis and gave me helpful advice with her flexible thoughts when I got stuck on my studies. Without her support, I would never have been able to finish this work. I could not have had a better advisor than her. I also thank Prof. Kazuhisa Mitsuda for his encouragement. He gave many opportunities for me to consider the study contents deeply by his insightful questions at our laboratory meetings. Additionally, I appreciate the daily support of Noriko Takahashi, the secretary in ISAS. Her help was possible things going smoothly and made me concentrate my study without spending effort on trivial duties for procurement and paperwork.

My four years in AIST were exciting, curious, and passionate every day. I have been fortunate to associate with Drs. Satoshi Kohjiro and Fuminori Hirayama. Dr. Kohjiro taught me about the basic knowledge of superconductivity and microwave circuits, the way how to write a paper and present at an academic conference, and life in general. Dr. Hirayama introduced me to how to design MWMUX and patiently instructed me on how to handle refrigerator, equipment, and everything about measurement. The things learned from them will become the foundation of my scientist's life in the future. Apart from them, I have been supported by many persons in AIST. I also thank Dr. Akira Sato for his helpful advice with his outstanding knowledge of low-temperature physics and refrigerator. Dr. Hirotake Yamamori kindly supported my employment in AIST. I am very thankful to him. The MWMUXes used in this thesis were fabricated in CAVITY with the great help of Dr. Shuichi Nagasawa and the technical staff, including Michiyo Isaka. I would also like to thank Sachiko Kobayashi, the secretary in AIST, for her kind support for my lab life.

I was able to spend a fruitful time during my five years, thanks to Drs. Tomoya Irimatsugawa, Tasuku Hayashi, Haruka Muramatsu, Ryo Yamamoto, and Takahiro Kikuchi, and Ryota Hayakawa, Ryota Takaku, Ryohei Konno, Yuta Yagi, and Kosuke Hirano. I would like to thank them for fruitful discussions and experimental

support. The TESs used in this thesis were fabricated by Drs. Hayashi and Muramatsu in ISAS, and Dr. Kenichiro Nagayoshi in SRON. Dr. Yamada financially and technically supported us when we installed an adiabatic demagnetization refrigerator.

I would like to thank my thesis committee members, Prof. Takashi Uchiyama, Prof. Shingo Katsumoto, Prof. Naoki Kawashima, Prof. Aya Bamba, and Prof. Hiroaki Myoren for valuable comments and suggestions that helped polish this thesis. I would also like to express my deep appreciation to Dr. Damian Audley for the English proofreading.

Last but far from least, I am even very thankful to my father, mother, and sister for their support and encouragement. They gave me the opportunity and motivation to study in the doctoral course and emotionally supported throughout my five years.

Yuki Nakashima

Abstract

The transition-edge sensor (TES) X-ray microcalorimeter is a promising detector for realizing an X-ray camera with a high precision spectrometer on each pixel for future X-ray astronomical observatories such as *sDIOS*. In the future, X-ray detectors with fine energy resolution of less than 2 eV and a large field-of-view (FoV) are required to reveal physics of dark baryons and to resolve soft X-ray background. The detector works at a very low temperature (< 100 mK), thus the resolving power $E/\Delta E$ is typically greater than 1,000. From the size of the detector, to cover the large FoV of the telescope, more than 10^4 TES pixels are required. So, a multiplexing readout is a must to operate such large-format TES arrays in space. However, there are so far no mature multiplexing techniques to read out more than 10^4 pixels simultaneously. To resolve this situation, we have developed a microwave superconducting quantum interference device (SQUID) multiplexer (MWMUX). MWMUX is a promising technique, being capable of reading out 1–2 orders of magnitude more pixels, compared with conventional methods with bandwidths of several MHz, i.e., TDM, CDM and FDM.

This thesis is concerned with the development of a microwave SQUID multiplexer to read out transition-edge sensor X-ray microcalorimeter arrays for future astrophysical observations. For the development, we set the targets to read out the fast signal of TES X-ray microcalorimeters by using MWMUX with low readout noise and several tens of pixels. First, we have developed MWMUX with a larger resonance bandwidth (BW), more than ~ 2 MHz, in order to read out TESs with sufficient sampling frequency. Second, we have developed MWMUX with a lower noise level than that of TESs. The typical sensor noise is ~ 30 pA/ $\sqrt{\text{Hz}}$, thus we aimed at a readout noise value below that. Finally, we have developed MWMUX with many channels to demonstrate readout of large-format TES arrays. We aimed at a number of channels more than 40, which is the same as the state-of-the-art design of the future *Athena* X-IFU instrument.

We have developed 40ch MWMUX with resonator bandwidth of ~ 2 MHz and low readout noise of around 10 pA/ $\sqrt{\text{Hz}}$. Using the developed MWMUX, we simultaneously read out 38 TES X-ray microcalorimeter pixels, and successfully detected Mn $K\alpha$ X-ray signals from all 38 pixels. Furthermore, we obtained the 38

spectra with the best and median energy resolution of 2.8 eV and 3.3 eV FWHM at 5.9 keV, respectively. The contribution of readout noise of MWMUX to the energy resolution was calculated to be not more than 1.8 eV. These results surpass the performance of the SXS instrument, which was onboard the *Hitomi* satellite and operated in orbit in 2016, in both the energy resolution and the number of pixels. Furthermore, the obtained results are comparable to the requirement of 2.5 eV with a 40-pixel FDM multiplexing readout for the *Athena* satellite to be launched in 2031. Through the researches of this thesis, we demonstrated microwave multiplexed readout of large-format TES arrays with fine energy resolution. The results in this thesis will impact X-ray astronomy by showing the feasibility of an X-ray camera with high precision spectrometer on each pixel for future X-ray astronomical observatories.

List of Publications

Three papers related to this dissertation have been published as follows.

1. Yuki Nakashima, Fuminori Hirayama, Satoshi Kohjiro, Hirotake Yamamori, Shuichi Nagasawa, Noriko Y. Yamasaki and Kazuhisa Mitsuda. Adjustable SQUID-resonator direct coupling in microwave SQUID multiplexer for TES microcalorimeter array. *IEICE Electronics Express*, 14(11):20170271–20170271, 2017.
2. Y. Nakashima, F. Hirayama, S. Kohjiro, H. Yamamori, S. Nagasawa, A. Sato, T. Irimatsugawa, H. Muramatsu, T. Hayashi, N. Y. Yamasaki, and K. Mitsuda. Readout of X-ray Pulses from a Single-pixel TES Microcalorimeter with Microwave Multiplexer Based on SQUIDs Directly Coupled to Resonators. *Journal of Low Temperature Physics*, 193(3):618–625, Nov 2018.
3. Y. Nakashima, F. Hirayama, S. Kohjiro, H. Yamamori, S. Nagasawa, A. Sato, N. Y. Yamasaki, and K. Mitsuda. Investigation of Large Coupling Between TES X-Ray Microcalorimeter and Microwave Multiplexer Based on Microstrip SQUID. *IEEE Transactions on Applied Superconductivity*, 29(5):1–5, Aug 2019.

Contents

Acknowledgements	i
Abstract	iii
List of Publications	v
List of Figures	xii
List of Tables	xiii
1 Introduction	1
2 Review	3
2.1 Imaging Spectroscopy in X-ray Astrophysics	3
2.2 Requirements for Microcalorimeters and Future X-ray Imaging Spectroscopic Mission	4
2.3 Transition-Edge Sensor (TES) Microcalorimeter	5
2.4 Conventional Multiplexing Techniques	8
2.5 Microwave SQUID Multiplexer (MWMUX)	10
3 Theory of the Microwave SQUID Multiplexer	12
3.1 Microwave Resonator	12
3.1.1 Simple Lumped <i>RLC</i> Parallel Resonant Circuit	12
3.1.2 Quarter-Wave Transmission Line Resonator	14
3.2 Microwave Resonator Capacitively Coupled to a Feedline	16
3.2.1 Scattering Matrix of a Symmetric 3-Port Capacitive Coupler	16
3.2.2 Reflection Coefficient Γ_r of a $\lambda/4$ -Resonator Terminated by a SQUID	18
3.2.3 Transmission Coefficient t_{21}	18
3.3 Transmission Coefficient Model of a MWMUX	20
3.3.1 Network Model of an Asymmetric Resonator	20
3.3.2 Modification of <i>S</i> -parameters	20

3.3.3	Transmission Coefficient t'_{21} under Impedance Mismatches	21
3.3.4	Measured Transmission Coefficient T_{21}	22
3.3.5	Property of the Transmission Coefficients	22
3.4	Dissipationless Radio Frequency (RF) SQUID	23
3.4.1	Flux Quantization	23
3.4.2	Josephson Inductance	25
3.4.3	RF-SQUID: Superconducting Loop with One Junction	26
3.4.4	SQUID Inductance $L(\Phi)$: Flux-Variable Inductance	28
3.5	Resonance Frequency Variations with Respect to Flux Signal Input	30
3.6	Flux-Ramp Modulation (FRM)	31
4	MWMUX01: Conceptual Design of MWMUX for Readout of a TES X-ray Microcalorimeter	33
4.1	Key Component: SQUID Directly Coupled to Resonator	33
4.1.1	Background	33
4.1.2	SQUID Design	33
4.1.3	Experimental Evaluation & Validity of Design	36
4.2	Overall Design of MWMUX Chip for Readout of X-ray TES	38
4.2.1	Frequency Allocation	38
4.2.2	Coupling Capacitor: Resonator-Feedline Coupling	39
4.3	Performance Evaluation	40
4.4	Single-pixel TES Readout with MWMUX01	40
4.4.1	Experimental Setup	40
4.4.2	Result: Pulse Detection with MWMUX01	42
4.4.3	Result: Noise & Integrated Noise Equivalent Power Resolution	43
4.4.4	Result: Single-Pixel Performance with MWMUX01	44
4.4.5	Discussion	45
4.5	Summary	46
5	MWMUX02: Low Current Noise MWMUX	47
5.1	Objective of Development	47
5.2	Design	48
5.2.1	Resonance frequency and BW	48
5.2.2	SQUID, Input coil and Mutual Inductance	49
5.3	Fabrication	49
5.4	Measurement Setup	51
5.5	Results	52
5.5.1	Resonances and SQUID characteristics	52
5.5.2	Flux and Current Noise	52
5.6	Discussion	55
5.7	Summary	56

6	MWMUX03 and Low-Temperature Components for 80-Pixel TES Readout	57
6.1	Design	57
6.2	Fabrication	59
6.3	Performance Evaluation	60
6.3.1	Results	60
6.3.2	Importance of Airbridge to Avoid Undesirable Resonances	63
6.4	Development of a 40-Channel Bias Chip for Activating TES Microcalorimeters	64
6.5	Summary	65
7	Measurement Setup for Readout of TES X-ray Microcalorimeters with 38ch MUX	67
7.1	Measurement System	67
7.2	Low-temperature Setup	70
7.3	TES Microcalorimeter: SRON Kilo-pixel Uniform Array	71
7.4	MWMUX Setup	72
8	Readout of TES X-ray Microcalorimeters with 38ch MUX	77
8.1	Optimization of Magnetic Field	77
8.1.1	IV Characteristic on Magnetic Field	77
8.1.2	Pulse Shape Dependence on a Magnetic Field	78
8.2	Optimization of TES Bias Point	78
8.3	Pulse Collection	82
8.3.1	Optimal Filtering	84
8.3.2	Construction of <i>PHA</i> Data Sets	86
8.3.3	Gain-drift Correction	88
8.3.4	Hölzer Fit to Mn $K\alpha$ Line Complex	88
8.3.5	Result	90
8.4	Summary	90
9	Discussion	95
9.1	Energy Resolution	95
9.2	Number of Multiplexed Pixels	96
9.3	Summary	98
10	Conclusion	99
A	List of Instruments and Components	101
B	Superconducting Microstrip Line Inductance	103

C Energy Spectra and Gain-Drift Correlations of All 38 Pixels	105
Bibliography	128

List of Figures

2.1	Transition-edge sensor (TES) microcalorimeter	6
2.2	TES readout of single pixel and 64-pixels non-multiplexing with DC-SQUID	7
2.3	Conventional multiplexing techniques	8
2.4	Microwave SQUID multiplexer (MWMUX)	10
3.1	<i>RLC</i> parallel resonant circuit	13
3.2	Quarter-wavelength transmission line resonator	15
3.3	Capacitive coupler and signal-flow graph	17
3.4	Signal-flow graph under condition of impedance mismatches	21
3.5	Example plots of the transmission coefficients	24
3.6	Schematic and circuit symbol of Josephson junction	25
3.7	Schematic and circuit symbol of RF-SQUID	27
3.8	Total flux Φ and the applied one Φ_a	28
3.9	Circuit diagram of an RF-SQUID with fractional parameter a	29
3.10	SQUID inductance versus input magnetic flux	29
3.11	Variation of resonance frequency and transmission coefficient	30
3.12	Flux-ramp modulation (FRM)	31
4.1	Two ways of SQUID-resonator coupling	34
4.2	A photograph and the equivalent circuit schematic of the SQUID	35
4.3	Experimental SQUID inductance vs. l_{JJ} and designed a	37
4.4	Experimental and designed fractional parameter a vs. l_{JJ}	38
4.5	Micrograph of coupling capacitor and relation between C_c and D_c	39
4.6	The measured $ S_{21} ^2$ and maximum resonance frequency shift	40
4.7	Setup for single-pixel TES readout with MWMUX	41
4.8	Pulses expected from Mn $K\alpha$ for nine different bias points	42
4.9	Current noise and NEP spectra for nine different bias points	43
4.10	The integrated NEP as a function of the bias point	44
4.11	The energy spectrum obtained by single-pixel TES readout with MWMUX	45

5.1	The mask design of MWMUX02	48
5.2	Micrograph, design drawing, and cross-section of SQUID and schematic of the input coil	50
5.3	Transmitted power, variances of resonance frequencies and θ	53
5.4	Voltage/ θ v.s. input flux characteristics of DC-SQUID/RF-SQUID	54
5.5	Flux and current noise spectra	54
5.6	Comparison between current-noise spectra of MWMUX01 and MWMUX02	55
6.1	Mask designs of two 40-channel MWMUX chips	59
6.2	Micrograph of a SQUID, an RF filter, and pads for airbridges.	60
6.3	Measured 40ch resonances and spacings	61
6.4	Measured maximum resonance frequency shifts and bandwidth	61
6.5	Measured quality factors	62
6.6	Measured noise spectra	62
6.7	White-noise level extracted from the measured noise spectra	63
6.8	Importance of airbridge to evade parasitic resonances	64
6.9	Mask design of the bias chip	65
6.10	Circuit schematic of the bias chip	65
7.1	Overview of the measurement system in AIST	68
7.2	ADR system and temperature fluctuation	68
7.3	Photo of the room-temperature electronics	69
7.4	Circuit diagram of MWMUX readout testbed	70
7.5	Low-temperature setup	71
7.6	TES X-ray microcalorimeter array developed by SRON	72
7.7	The pixel map of the TES X-ray microcalorimeter array	74
7.8	Transmission $ S_{21} $ of all 80ch resonances	75
7.9	The SQUID response in the I/Q plane with respect to DC signals	75
7.10	Averaged SQUID response with respect to a 500 kHz flux-ramp wave	76
7.11	White noise levels with respect to comb power per comb injected into the ADR	76
8.1	The IV characteristic of all 40 TESs	79
8.2	The IV of Ch41 with respect to different magnetic fields	80
8.3	The dissipation of 38-pixel TES at the bias point of 20%	80
8.4	Averaged pulses of Ch48 under different fields	81
8.5	Amplitudes & fall time constants of Ch48 under different fields	81
8.6	NEP resolution of Ch72 at different bias points	82
8.7	The averaged pulses of all 38 pixels	83
8.8	The noise spectra of all 38 pixels	83

8.9	Flowchart of the signal processing with optimal filtering	85
8.10	Templates of all 38 pixels used in this experiment	87
8.11	An example of the effects of the three corrections	87
8.12	The gain drift and correlation between baseline and <i>PHA</i>	89
8.13	The obtained energy spectra from all 38 TES microcalorimeters . . .	91
8.14	The energy spectra with the best-recorded energy resolution	92
8.15	The combined energy spectrum from 38 pixels	93
8.16	The histogram of the energy resolutions among all 38 pixels	94
8.17	The energy resolutions on the TES pixel map	94
9.1	The noise spectra taken at a bath temperature of 125 mK	97
9.2	The readout noise contributions to the energy resolutions	97
9.3	The slew rate of Mn $K\alpha$ pulses of all 38 TES pixels	98
B.1	Superconducting microstrip line	104
C.1	The energy spectra and anti-correlations between energy and base- line of all 38 pixels	118

List of Tables

5.1	Summary of SQUID's properties	56
6.1	Design parameters of two MWMUX03 chips	58
6.2	Design targets and measurement results of developed MWMUX . . .	66
8.1	Mn $K\alpha$ line complex	90

Chapter 1

Introduction

X-ray imaging spectroscopy is a powerful tool to explore the Universe. In the early Universe, the source of re-ionizing radiation whose energy should be larger than 13.6 eV is still unresolved. Even in the current Universe, the origin of the soft X-ray background is not fully understood. Not only astronomical objects like stars and galaxies but a large part of the baryons in the Universe emits X-rays because they are also now in the form of diffuse and ionized plasma as warm or hot intergalactic medium. X-ray spectroscopy gives us plenty of information on such plasma, i.e., temperature, ionized status, chemical composition, velocity field, and so on.

As the emission is diffuse in nature, a non-diffractive method is required. Position-sensitive proportional counters on *Einstein*, *Tenma*, and *ASCA*, and X-ray CCDs on *ASCA*, *Chandra*, and *XMM-Newton* were used in astrophysical observations, increasing both the energy and spatial resolutions. *Hitomi* was the first to use an X-ray microcalorimeter array in orbit, and revealed the velocity field and placed a limit on the non-thermal energy in the Perseus cluster of galaxies, with an energy resolution less than 5 eV. The number of pixels in the array detector on *Hitomi* was only 32, and the future *Athena* X-IFU will have 3840 pixels, but still they are much smaller than those of X-ray CCDs, typically 1000×1000 . The main reason for this barrier is that the excellent energy resolution of microcalorimeters is only available at a low temperature less than 0.1 K and that the number of wires to such a cold stage is limited by their heat flow from room-temperature electronics. *Athena* X-IFU will use a signal multiplexing technique, which is known as Frequency-Division Multiplexing (FDM), and will read 40 pixels in one signal channel.

Recently, microwave multiplexing (MWMUX) method utilizing superconducting quantum interference devices (SQUIDs) has been invented to read cryogenic detectors, including KIDs and transition-edge sensors (TES) that detect γ -rays. Application of MWMUX to X-ray TESs poses a challenge to handle fast signals

due to the small heat capacity in the sensor or to extend the signal bandwidth in high-Q resonance circuits.

In this thesis, we investigate the application of MWMUX to X-ray TES by newly designed and fabricated multiplexing and de-multiplexing circuits. In chapter 2, we review past studies, and in chapter 3, the principles of MWMUX resonators are summarized. From chapter 4 to 6, step-by-step developments of MWMUX are described. For the development, we set the targets to read out the fast signal of TES X-ray microcalorimeters by using MWMUX with low readout noise and several tens of pixels. First, we have developed MWMUX with a larger resonance bandwidth (BW), more than ~ 2 MHz, in order to read out TESs with sufficient sampling frequency. Second, we have developed MWMUX with lower noise levels than those of TESs. The typical sensor noise is ~ 30 pA/ $\sqrt{\text{Hz}}$, thus we aimed at a readout noise value below that. Finally, we have developed MWMUX with many channels to demonstrate readout of a large-format TES array. We aimed at a number of channels more than 40, which is the same as the state-of-the-art design of the future *Athena* X-IFU instrument. In chapter 7, a set up for the combined evaluation of a newly-developed MWMUX with 40 channels and a TES array is presented, and experimental results and analysis are shown in chapter 8. After a discussion on chapter 9, the conclusion of this thesis will be given in chapter 10.

Chapter 2

Review

2.1 Imaging Spectroscopy in X-ray Astrophysics

From the beginning of X-ray astrophysics, very complex energy spectra with many emission and/or absorption lines have been investigated, because highly ionized plasma with $T = 10^{6-8}$ K or $k_B T = 0.1-12$ keV emits many characteristic lines in the X-ray energy band. For example, Tanaka & Bleeker (1977) [1] studied the diffuse soft X-ray emission distributed over the entire sky, which is called the Soft X-ray Diffuse Background (SXDB), by rocket-borne proportional counters, and proposed the existence of a hot gas of $T \sim 10^6$ K in the interstellar space. The SXDB was observed again by a microcalorimeter array, and OVII (561, 568, and 574 eV at rest frame), OVIII (653 eV at rest frame), and a few other emission lines were clearly resolved with an energy resolution of ~ 9 eV (McCammon et al. 2002 [2]).

Such diffuse and complex emission is considered to be caused by many layers in the Universe and is not understood completely even now. Supernova remnants in our Galaxy, elliptical and spiral galaxies, and clusters of galaxies are well-known sources of diffuse X-rays. The emissions caused by the charge exchange interaction between solar wind and neutral particles existing at the neighborhood [3] and in Earth's Solar system objects (e.g., [4]) are considered to be the part of the SXDB. Recently a possibility was claimed that a highly redshifted ($z > 6$) component associated with the strong X-ray emission by the rapid evolution of supermassive black holes (SMBH) in the early Universe could contribute to the SXDB [5]. Also, very dim emission from large-scale filamentary structure called WHIM (Warm-Hot Intergalactic Medium) has been suggested by hydrodynamical simulations (e.g., Cen & Ostriker 1999 [6]), and its location could be identified by redshifted Oxygen emission energy [7, 8].

According to the baryon budget described in Fukugita et al. 1998 [9], the ma-

majority of baryons in the present universe are still unexplored. Cosmological simulations and recent observations indicate that approximately 30–50% of the total baryons in the local Universe ($z = 0$) take the form of WHIM with a temperature of 10^5 to 10^7 K and exist along the large-scale filamentary structure [6, 7].

Since oxygen is the most abundant metal in the universe and highly ionized oxygen, or OVII and OVIII, is the most significant component in the 10^5 to 10^7 K gas, we could study the large-scale structure of WHIM by detecting OVII and OVIII emission lines at the various redshifts. However, the current observations do not have enough energy resolution to separate emissions from WHIM and our Galaxy from the redshift. As well as energy resolution, a large “effective-area times field-of-view ($S\Omega$)” and sufficient spatial resolution are also required to detect enough photons and separate the contaminating point sources in order to detect and survey the large-scale structure of WHIM. Thus, a more powerful imaging spectroscopy tool, i.e., sensors with a wide field of view (FoV), and fine spatial and energy resolution are required for future observations.

In the following section, we describe the requirements for the detector and the next generation X-ray space mission.

2.2 Requirements for Microcalorimeters and Future X-ray Imaging Spectroscopic Mission

Following the calculation of the detectability of oxygen emission from WHIM by Mitsuda [10] and Takei et al. [8], the significance σ_{line} of a line detection can be given by

$$\sigma_{\text{line}} = \frac{f_{\text{line}}}{\sqrt{f_{\text{line}} + f_{\text{BG}}\Delta E}} \sqrt{S\Omega t_{\text{exp}}}, \quad (2.1)$$

where f_{line} , f_{BG} , S , Ω , t_{exp} , and ΔE are the source line flux in units of photons/s/cm²/sr, background intensity in units of photons/s/cm²/sr/keV, effective area, FoV, the exposure time, and the energy resolution of the detector, respectively. At the energy of OVII and OVIII emission lines, the Galactic emission dominates the background continuum spectrum, and the typical intensity is 30 photons/s/cm²/sr/keV. Meanwhile, according to the estimation of the surface brightness of an oxygen emission line of a filament by Mitsuda [10], the source line flux f_{line} is 0.05 photons/s/cm²/sr. Therefore, the equivalent width of the oxygen emission lines (~ 600 eV) can be estimated to be $0.05/30$ keV ~ 2 eV. An energy resolution of less than 2 eV makes the sensitivity limited by photon statistics rather than by background/continuum emissions. Moreover, some studies of the detectability of WHIM emission with cosmological simulations indicate that an energy resolution of less than $\Delta E \sim 2$ eV makes the OVII and OVIII emissions separate from other

prominent Galactic lines [7, 8]. Thus, the energy resolution of a detector is required to be $\Delta E < 2 \text{ eV}$, and the transition-edge sensor (TES) X-ray microcalorimeter is the only option to realize such high resolution. As well as energy resolution, a large $S\Omega$ is required from Eq. 2.1 to detect and survey WHIM emission with sufficient significance (e.g., $> 5\sigma$) under the flux detection limit of $0.05 \text{ photons/s/cm}^2/\text{sr}$.

The future Japanese X-ray satellite mission, Super Diffuse Intergalactic Oxygen Surveyor (*sDIOS*), is planned to search for dark baryons in the form of WHIM by detecting those oxygen emissions from redshift of 0.3 to the present. The energy resolution, effective area S and FoV Ω are planned to be less than 2 eV at 1 keV, larger than 1000 cm^2 and $\sim 30 \text{ arcmin}$, respectively. The goal for the angular resolution is 10–15 arcsec to separate out WHIM emission from contaminating point sources. Thus, the requirement for the number of pixels of TESs is ~ 30000 . In future space missions such as *sDIOS*, the energy resolution $< 2 \text{ eV}$ and the number of pixels > 30000 are required for the TES X-ray microcalorimeter.

2.3 Transition-Edge Sensor (TES) Microcalorimeter

A superconducting transition-edge sensor (TES) [11] is the most sensitive calorimeter, taking advantage of the high temperature sensitivity of resistance, α , within the superconducting phase transition. TESs are used as a thermal detector in various applications over a span of more than ten orders of magnitude in wavelength and energy. For example, TES can be applied to analysis of nuclear material by alpha spectroscopy [12], X-ray spectroscopy in material analysis [13], hadronic-atom X-ray spectroscopy [14], optical biological imaging [15], and astronomical missions such as *LiteBIRD* [16] and *SPICA* [17], or future X-ray satellites such as *Athena* [18], *sDIOS* [19], *Lynx* [20], and *Cosmic Web Explorer* [21].

Figure 2.1 shows schematics of a TES, a transition edge, and a pulse in temperature excited by incident energy. A TES generally consists of an absorber, a thermometer, and a thermal link to a heat sink. The absorber and thermometer with heat capacity C are heated to a temperature of $T = T_{\text{bath}} + E/C$ by an incident X-ray or γ -ray photon with energy E , and relax to the bath temperature T_{bath} with a time scale of $\tau = C/G$, where G is the thermal conductance between the heat capacity and the heat sink. Compared with γ -ray TESs, the absorbers in X-ray TESs strongly couple to the thermometers due to the thickness of the absorbers. Therefore, heat in the absorber diffuses to the thermometer much faster in the case of X-rays than *gamma*-rays, and that yields a small rise-time constant in X-ray TESs. The energy resolution ΔE is limited by thermal fluctuations in the heat capacity at temperature T due to the exchange of energy with the heat

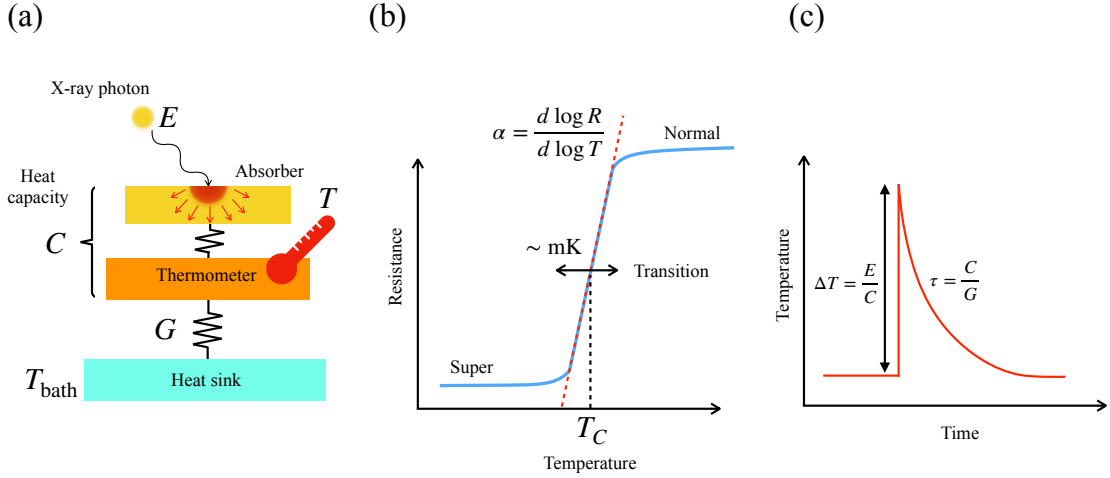


Figure 2.1: (a) Schematic of transition-edge sensor. An incident X-ray of energy E heats a capacitor consisting of an absorber and a thermometer above the temperature of a heat reservoir. (b) A superconducting resistive transition edge. (c) A pulse in temperature excited by an incident energy deposition.

sink at T_{bath} :

$$\Delta E = 2.35\xi\sqrt{k_{\text{B}}T^2C}, \quad (2.2)$$

where ξ is a parameter determined by the thermometer sensitivity [11]. The best TES energy resolutions achieved to date are 1.58 eV FWHM at 5.9 keV [22] and 0.72 eV FWHM at 1.5 keV [23].

The suppression of thermal noise at low temperatures allows TESs to measure energy with great precision. In the case of X-rays, the resolving power $E/\Delta E$ can achieve greater than 10^3 , which is significantly better compared with conventional CCDs used for X-ray imaging spectroscopy in astrophysics. The transition temperature T_c is usually tuned to around 50–100 mK in order to obtain a desirable resolution, by using a variety of thin films as TESs. For films, elemental superconductors (e.g., W), alloys (e.g., Mn-doped Al), and proximity-coupled superconducting/normal-metal bilayers or multilayers (e.g., Mo/Cu, Mo/Au, Ti/Au) are fabricated for TESs. The TES film is electrically contacted by superconducting leads (such as Nb and Al) so as to connect to the external world.

In actual operation, TES should always be biased at a working point within the transition edge. The transition edge is quite narrow (e.g., $\sim \text{mK}$); however, biasing can be realized by the use of a voltage-biased readout achieved by placing the TES in parallel with a shunt resistor whose resistance is much smaller than that of the

TES [24]. In this regime, the current through TES is measured. The resistance of TES, the variation of the current, and the current noise are very small, typically 1–100 m Ω , $\sim 10 \mu\text{A}$ and $\sim 30 \text{pA}/\sqrt{\text{Hz}}$.

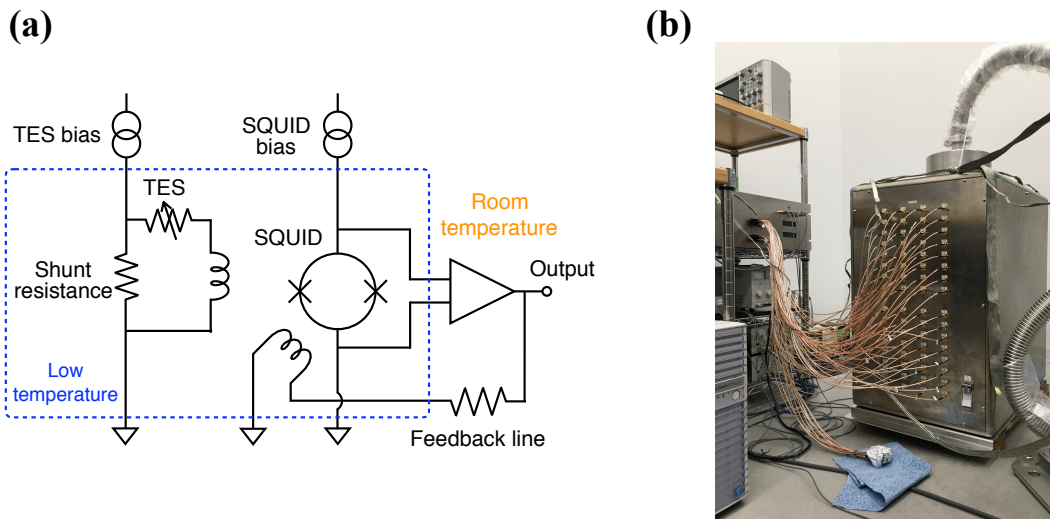


Figure 2.2: (a) Schematic of a voltage-biased TES readout with DC-SQUID. (b) Photo of 64-pixel non-multiplexing readout with DC-SQUID. Photograph courtesy of Dr. Tasuku Hayashi, ISAS/JAXA.

A superconducting quantum interference device (SQUID) is a suitable ammeter for TESs because of its low impedance, high current (or flux) resolution, and low input-referred noise. Figure 2.2 (a) shows a circuit schematic of the general voltage-biased readout with a direct current (DC) SQUID. The TES and SQUID are placed at the low-temperature stage. The current through the TES is converted to a magnetic flux at an input coil coupled to the SQUID, and then converted to a voltage across the SQUID and read out by voltmeters at room temperature. Since the SQUID has a periodic response, the SQUID is generally operated under negative feedback. The feedback keeps the flux threading the SQUID ring constant and is therefore called a flux-locked loop (FLL). In the FLL, the SQUID output is fed back to the SQUID itself through a feedback line. When we read out a TES with a single DC-SQUID, we generally need four pairs of wires; one for TES bias, another for SQUID bias, another for SQUID feedback, and the other for SQUID output, as shown in Fig. 2.2 (a). For a single TES or TES array with a small number of pixels, signal wires for output of individual SQUID corresponding to each TES pixel can be connected in parallel between the cryogenic stage and room-temperature electronics. This approach cannot be scaled up to large-format arrays

to image and/or boost collection efficiency and count rate, since this increases the heat flow from room-temperature to the cryogenic stage through signal and/or bias wires to prohibitive levels and complicates electronic handling as shown in Fig. 2.2 (b). Thus, the SQUID multiplexing technique is potentially needed for the readout of large-format TES arrays. In what follows, we provide summaries of the three conventional methods of SQUID multiplexing and the promising microwave SQUID multiplexing.

2.4 Conventional Multiplexing Techniques

For more than a decade, time-division multiplexing (TDM) [25], code-division multiplexing (CDM) [26], and frequency-division multiplexing (FDM) with several-MHz bandwidth [27] have been developed [28]. Figure 2.3 shows example modulation functions for four channels in three different conventional multiplexing techniques.

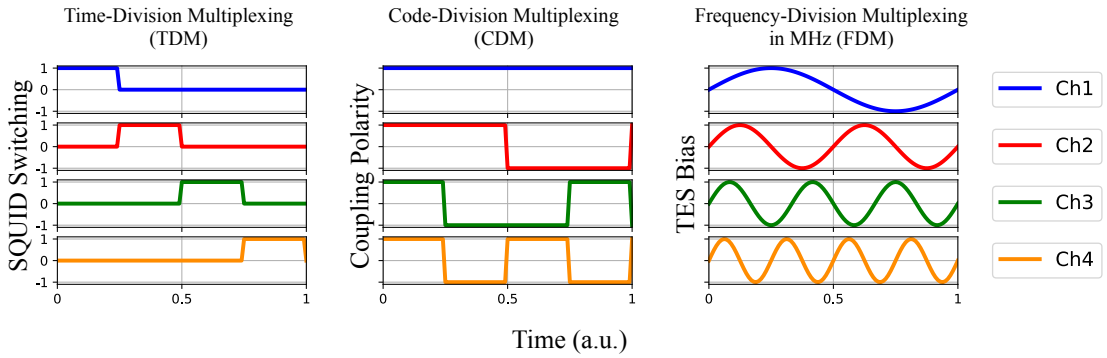


Figure 2.3: Modulation functions for four channels in three different conventional multiplexing techniques.

TDM consists of N current-bias lines (*rows*) and M output lines (*columns*). M first-stage SQUIDS in each row are electrically connected in series, and N first-stage SQUIDS in each column are magnetically coupled to each common second-stage SQUID. Each DC-voltage biased TES is connected to its own first-stage SQUID, thus signals from TESs in each column can be multiplexed into each output line. TDM can reduce the number of signal wires $\mathcal{O}(M \times N)$ to $\mathcal{O}(M + N)$ in comparison to the non-multiplexing readout. As shown in Fig. 2.3 (*left*), each row is turned on sequentially, and columns of SQUIDS are read out in parallel. The bandwidth of each measurement is determined by the boxcar modulation function (see Fig. 2.3 (*left*)). To date, the shortest time demonstrated for turning on and measuring

a SQUID is 320 ns [28]. Thus, the bandwidth of TDM is in the MHz range, and N is limited to several dozen in the case of X-ray TESs whose typical signal band is 10–100 kHz. Due to the dead time of measurement, or to aliasing, the effective SQUID current noise scales as \sqrt{N} . That also makes it difficult to increase N . TDM is the most mature multiplexing technique compared to the others and is used in many applications. For example, 30-row \times 8-column TDM is used to read out 240-pixel X-ray TESs for beamline science [29].

In CDM, TESs are magnetically coupled to all the SQUIDs with polarity defined by the appropriate column of the Walsh basis set [28], and the polarity of the signals from the TESs are modulated by a switch as shown in Fig. 2.3 (*middle*). During each time step, the signals from all DC-biased TESs in a readout column are summed with equal weight but different polarity patterns [30]. All the TESs are measured all the time in contrast to TDM, thus CDM does not suffer from the \sqrt{N} noise penalty. With a 32-channel CDM circuit, Morgan et al. 2016 [30] have achieved a 30-pixel combined energy resolution of 2.77 eV FWHM at 5.9 keV and a best single-pixel resolution of 2.28 eV FWHM.

In FDM, the LCR filter circuits are used to apply a different oscillating voltage bias to each TES. The modulated currents through the TESs are summed into a common SQUID amplifier and demodulated by room-temperature electronics to reconstruct the TES signals of each channel. The TESs are usually biased at several MHz, therefore, the output signals should be fed back as fast as several μ s from room-temperature electronics to the SQUID at the low-temperature cryogenic stage. However, it is difficult to realize stable operation due to the parasitic capacitance on electrical wires from room to low temperature. To achieve a stable FLL even at MHz frequencies, a feedback scheme called baseband feedback (BBFB) [31] is always used. The feedback bandwidth restricts frequency band used in FDM to MHz. Thus the number of pixels employed in a readout SQUID is limited to several dozen in the case of X-ray TES whose typical signal band is 10–100 kHz. FDM has been used for many existing instruments and has been actively developed to be on board *Athena* satellite in 2031. In the mission, 3840 X-ray TESs will be measured by using 92 readout SQUIDs on each of which 40 X-ray TESs will be multiplexing.

The overall system bandwidth of those multiplexing is limited in the MHz range. Thus the number of multiplexed pixels is restricted to below 100 in the case of X-ray TES. However, for future astrophysics observations, there is a need for a multiplexing technique capable of reading out thousands of detectors in a single output channel. As the promising SQUID multiplexing to meet this requirement, microwave SQUID multiplexer (MWMUX) is very attractive because of its much larger bandwidth than those of three conventional methods, potentially several GHz. In the following section, we present the summary of microwave readout.

2.5 Microwave SQUID Multiplexer (MWMUX)

Irwin & Lehnert 2004 [32] first proposed and demonstrated the microwave SQUID multiplexer (MWMUX). The first demonstration used lumped element resonator circuits and DC-SQUIDS to modulate the quality factor Q of the resonator. They measured a flux noise of $\sim 0.5 \mu\Phi_0/\sqrt{\text{Hz}}$, where Φ_0 is the flux quantum with the value of 2.07×10^{-15} Wb, and demonstrated the multiplexed readout of two DC-SQUIDS at frequencies ~ 500 MHz. Also, they proposed the use of lithographically fabricated resonators in order to operate MWMUX at a much higher frequency. Mates et al. 2008 [33] and Mates Ph.D. thesis [34] established the foundations of the current device, which uses the change in inductance of a dissipationless radio frequency (RF) SQUID to modulate the resonance frequencies, and demonstrated multiple designs, noise as low as $0.17 \mu\Phi_0/\sqrt{\text{Hz}}$, and a naturally linear readout scheme based on flux modulation, called flux-ramp modulation (FRM) [35].

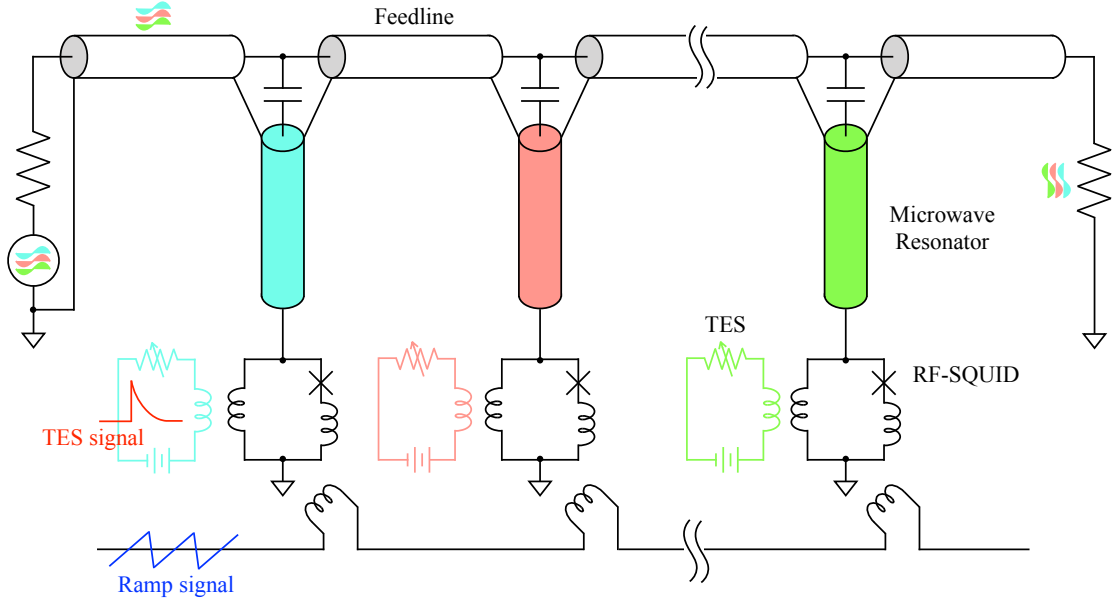


Figure 2.4: Circuit schematic of microwave SQUID multiplexer.

Figure 2.4 shows the circuit schematic of the microwave SQUID multiplexer. MWMUX consists of a number of high quality-factor (Q) microwave resonators, each employing a unique resonance frequency, terminated by an RF-SQUID. The injected powers are modulated by the resonators, and the transmitted powers are summed into the input of one cryogenic high electron mobility transistor (HEMT). Each SQUID acts as a flux-variable inductor responding to the magnetic flux

threading the SQUID loop in a flux-quantum cycle. And each SQUID is coupled to each TES. Thus, the TES signal can be read out by monitoring the shift of the resonance frequency depending on the magnetic flux activated by the change of current through the TES at energy irradiation. For multiplexing, those elements are capacitively coupled to a feedline. As with the readout system of microwave kinetic inductance detectors (MKIDs) [36], each signal can be simultaneously obtained by injecting multiple microwave tones into the feedline and monitoring the amplitude and phase of transmitted signals. For practical application, a flux-ramp signal is always applied to all the SQUIDs to linearize the SQUIDs' periodic responses.

Recently, Dober et al. 2018 [37] have developed a 512-channel multiplexer with 100 kHz resonator bandwidth, uniform 1.8 MHz frequency spacing, and an input-referred current noise of $35 \text{ pA}/\sqrt{\text{Hz}}$ for future submillimetre observations. Mates et al. 2017 [38] demonstrated microwave readout of 128 γ -ray TES pixels and achieved 89-pixel combined energy resolution of $55 \text{ eV}@97 \text{ keV}$. They developed MWMUX with a readout noise level of $2 \mu\Phi_0/\sqrt{\text{Hz}}$ ($19 \text{ pA}/\sqrt{\text{Hz}}$), and 300 kHz resonator bandwidth for 62.5 kHz flux-ramp modulation. Hirayama et al. 2013 [39] developed a microstrip-type SQUID with a vertical loop for accurate design of small SQUID inductance L_S , a MWMUX based on SQUID-resonator direct coupling and introduced the fractional parameter a . Using the MWMUX, Irinatsugawa Ph.D. thesis [40] read out two γ -ray TESs with energy resolutions of 118 and 128 eV@184 keV. As above, the developments of MWMUX for bolometers and γ -ray TESs are successful, while development for X-ray TESs is behind them due to the larger signal band of X-ray TESs. However, the development for this region is progressing. Yoon et al. 2018 [41] demonstrated 28-pixel simultaneous microwave readout with a flux-ramp frequency of 160 kHz, using an X-ray TES array and MWMUX respectively developed by GSFC/NASA and NIST. They have achieved a median spectral resolution of 3.4 eV FWHM at 5.9 keV.

Chapter 3

Theory of the Microwave SQUID Multiplexer

In this chapter, we summarize the theory of the microwave SQUID multiplexer (MWMUX), as shown in Fig. 2.4. The MWMUX consists of a set of superconducting microwave resonators terminated by either an inductance magnetically coupled to a dissipationless RF-SQUID or the SQUID itself. Each element employs a unique resonance frequency determined by both the intrinsic resonance frequency of the resonator and the SQUID inductance, depending on the magnetic flux threading its loop. First of all, let us start by exploring the resonator theory of the simple lumped RLC parallel and microwave resonator circuits in order to derive the model of the measured value. Next, we analyze the behavior of the SQUID as a magnetic-flux variable inductance. Finally, we will explain the novel modulation technique for the linearization and wide dynamic range of the input signal.

3.1 Microwave Resonator

3.1.1 Simple Lumped RLC Parallel Resonant Circuit

A resonant circuit consists of an inductor, a capacitor, and terminals for input and output. The impedance or admittance of the circuit drastically changes at a specific frequency. In general, a resonant circuit can be characterized by two main parameters, namely, the resonance frequency and the quality factor. The simplest case is shown in Fig. 3.1, and we start with analyzing this simple lumped RLC parallel resonant circuit by calculating the resonance frequency and the quality factor to understand the behavior of a transmission resonator.

In practice, a resonant circuit is always coupled to external circuitry. Therefore,

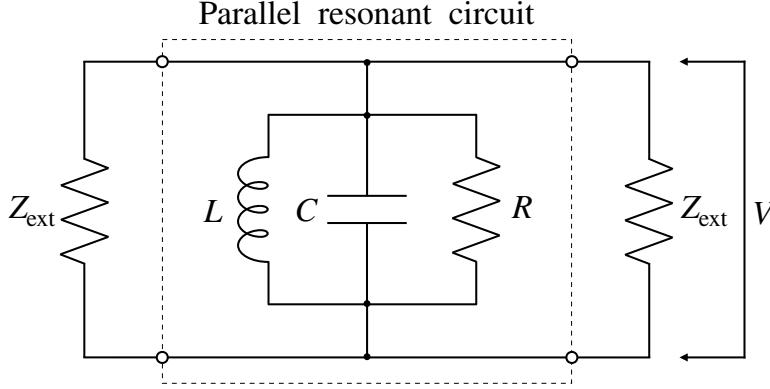


Figure 3.1: A simple RLC parallel resonant circuit. Each input and output port is terminated by an external circuit whose impedance is Z_{ext} .

let us consider the situation of the resonant circuit being coupled to the external resistance Z_{ext} , as shown in Fig. 3.1. The admittance Y of the circuit is given by

$$Y = \left(\frac{1}{R} + \frac{2}{Z_{\text{ext}}} \right) + i \left(\omega C - \frac{1}{\omega L} \right). \quad (3.1)$$

At the resonance, the susceptance is zero. Therefore, the resonance frequency can be written as:

$$\omega_0 = \frac{1}{\sqrt{LC}}. \quad (3.2)$$

The fundamental definition of the quality factor Q is

$$Q = 2\pi \frac{\text{Energy stored in the resonator}}{\text{Energy dissipated per cycle}} \quad (3.3)$$

[42, 43]. We can easily derive Q for the circuit at the resonance as follows.

The energy E stored in the resonant circuit at ω_0 is

$$E = \frac{1}{2}L|I_L|^2 + \frac{1}{2}C|V|^2 = C|V|^2, \quad (3.4)$$

where I_L and V are the current through L and the voltage across the circuit, respectively. Here, we note that the current and voltage amplitudes denote the root-mean-square (rms) values. The mean power dissipated at the interior resistance R and the external resistance Z_{ext} is

$$P = \frac{|V|^2}{R} + \frac{2|V|^2}{Z_{\text{ext}}}. \quad (3.5)$$

Finally, we find the quality factor of the parallel resonant circuit

$$Q = \frac{\omega_0 C}{\frac{1}{R} + \frac{1}{Z_{\text{ext}}}}, \quad (3.6)$$

and we can rearrange this equation to be

$$\frac{1}{Q} = \frac{1}{\omega_0 RC} + \frac{2}{\omega_0 Z_{\text{ext}} C} = \frac{1}{Q_i} + \frac{1}{Q_{\text{ext}}}, \quad (3.7)$$

where $Q_i = \omega_0 RC$ and $Q_{\text{ext}} = \omega_0 Z_{\text{ext}} C/2$ are the internal and the external quality factor, respectively.

There is an alternative method to calculate the quality factor at the resonance by using the slope parameter, defined as the frequency derivative of the impedance or the admittance of the circuit, and the quality factor is given by

$$Q = \frac{\omega_0}{2} \left| \frac{dZ/d\omega}{Z} \right|_{\omega=\omega_0} = \frac{\omega_0}{2} \left| \frac{dY/d\omega}{Y} \right|_{\omega=\omega_0}, \quad (3.8)$$

where Z and Y are the impedance and the admittance of the circuit, respectively. We note that the quality factor is invariant under the duality operation to the immittance [44], and therefore, can be written in the same form for Z and Y . By substituting Eqs. 3.1 and 3.2 into Eq. 3.8, we can easily find the same value with Eq. 3.6.

To facilitate later discussion, let us derive the input admittance Y_{in} of the parallel resonant circuit at a frequency near the resonance frequency $\omega = \omega_0 + \Delta\omega$, where $\Delta\omega/\omega_0 \ll 1$. Near the resonance, Y_{in} can approximately be written as

$$Y_{\text{in}} = \frac{1}{R} + i \left(\omega C - \frac{1}{\omega L} \right) \approx \frac{1}{R} + i2C\Delta\omega. \quad (3.9)$$

3.1.2 Quarter-Wave Transmission Line Resonator

In the microwave region, it is almost impossible to realize a reasonable resonant circuit consisting of lumped elements, due to the existence of parasitic reactances, which are practically unpredictable and whose values might be changed by the moment-to-moment experimental environment. On the other hand, a transmission line resonator, which consists of distributed elements, is useful at high frequency and makes the design simple because the resonance frequency depends only on the transmission-line length.

According to transmission line theory, the input impedance Z_{in} of a transmission line with length l is given by

$$Z_{\text{in}} = \frac{Z_L + Z_0 \tanh(\alpha + i\beta)l}{Z_0 + Z_L \tanh(\alpha + i\beta)l}, \quad (3.10)$$

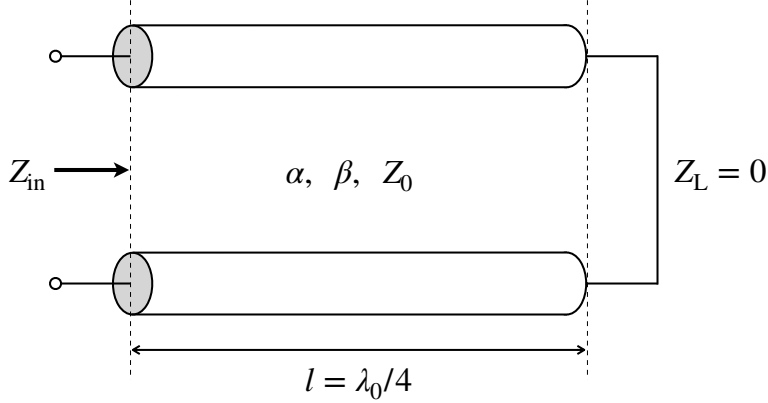


Figure 3.2: Schematic of a quarter-wavelength transmission line resonator.

where Z_0 , Z_L , α and β are the characteristic impedance of the transmission line, the load impedance terminating the transmission line, the attenuation coefficient and the phase constant, respectively. We consider a quarter-wave transmission line as shown in Fig. 3.2, hence $Z_L = 0$ and $l = \lambda_0/4$. λ_0 is equal to $2\pi v_p/\omega_0$, where v_p is the phase velocity. In this case, Eq. 3.10 is rewritten as:

$$Z_{in} = Z_0 \tanh(\alpha + i\beta)l = Z_0 \frac{1 - i \tanh \alpha l \cot \beta l}{\tanh \alpha l - i \cot \beta l}. \quad (3.11)$$

In the case where loss αl in a transmission line is small, $\alpha l \ll 1$, and the frequency $\omega = \omega_0 + \Delta\omega$ is near the resonance frequency, $\Delta\omega/\omega_0 \ll 1$, Eq. 3.11 can be reduced to

$$Z_{in} \approx Z_0 \frac{1}{\alpha l + i \frac{\pi}{2} \frac{\Delta\omega}{\omega_0}}, \quad (3.12)$$

hence the input admittance is given by

$$Y_{in} = \frac{1}{Z_{in}} = \frac{\alpha l}{Z_0} + i \frac{\pi}{2Z_0} \frac{\Delta\omega}{\omega_0}. \quad (3.13)$$

Deriving Eq. 3.12, the approximations are used as follows: $\tan \alpha l \approx \alpha l$ and $\cot \beta l \approx -\pi/2(\Delta\omega/\omega_0)$ for $\beta l = 2\pi l/\lambda = \pi/2(1 + \Delta\omega/\omega_0)$.

Due to the similar form of Eqs. 3.9 and 3.13, the quarter-wave transmission line resonator can be regarded as the equivalent circuit of a parallel RLC resonator. Comparing Eq. 3.9 with Eq. 3.13, the following relations are obtained:

$$R = \frac{Z_0}{\alpha l} \quad (3.14a)$$

$$C = \frac{\pi}{4Z_0\omega_0} \quad (3.14b)$$

$$L = \frac{1}{\omega_0^2 C}. \quad (3.14c)$$

Finally, we find the internal quality factor Q_i for the quarter-wave transmission line resonator is

$$Q_i = \omega_0 CR = \frac{\pi}{4\alpha l}. \quad (3.15)$$

This Q_i includes the contributions of all the various energy relaxation paths in the resonator.

3.2 Microwave Resonator Capacitively Coupled to a Feedline

The microwave resonator used in MWMUX is capacitively coupled to a feedline by a coupler whose equivalent circuit model is shown in Fig. 3.3 (a). The coupler plays an important role in the optimization of the bandwidth (BW) of the resonator because the coupling quality factor Q_c can be adjusted by the coupling capacitance C_c , as we can see below. Measuring transmitted power passing through the feedline, we can characterize the resonator readout circuit. Here, we derive a transmission coefficient t_{21} of the resonator readout circuit following the network analysis by Jiansong Gao [45].

3.2.1 Scattering Matrix of a Symmetric 3-Port Capacitive Coupler

As shown in Fig. 3.3 (a), the coupler is modeled by a 3-port network circuit, in which the feedline running from its port 1 to 2 is the lossless transmission line with the characteristic impedance Z_0 , and its port 3 is expected to be connected to the $\lambda/4$ -resonator with the characteristic impedance Z_r . Let us define the incident and reflected power waves of the i -th port of the coupler as: $a_i = (V_i + Z_i I_i)/2\sqrt{Z_i}$ and $b_i = (V_i - Z_i I_i)/2\sqrt{Z_i}$, where V_i and I_i are the voltage at and the current flowing into the i -th port of the coupler, and Z_i is the reference impedance of the i -th port. According to the definition of the scattering matrix S [42, 46], the scattering parameters (S -parameter) of the coupler, $S_{ij} = (b_i/a_j)_{a_k=0 (k \neq j)}$, can be calculated by terminating two of the three ports except for the j -th port with a load identical to the reference impedance Z_0 and/or Z_r . Due to the reciprocity of the network,

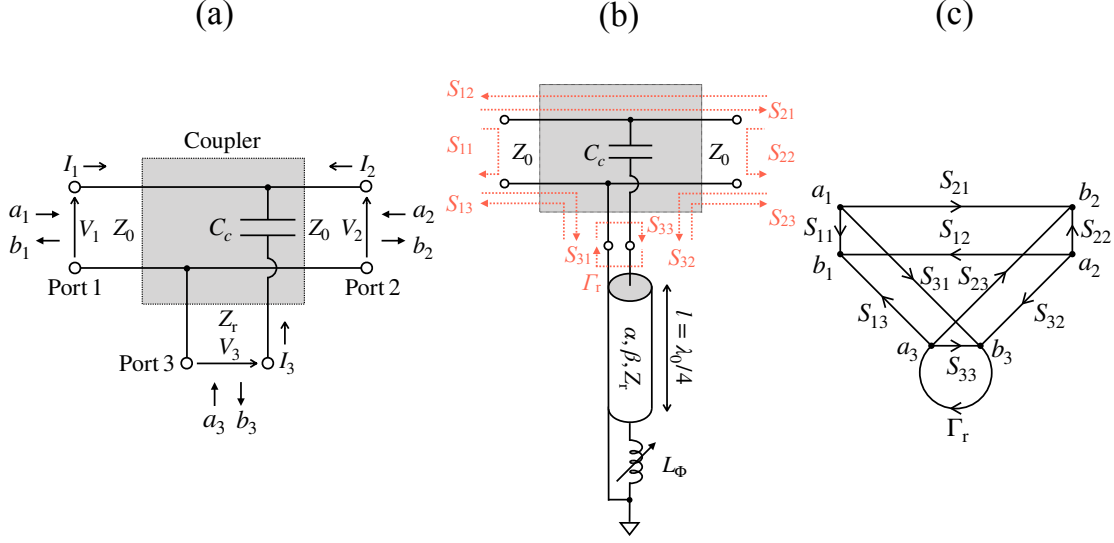


Figure 3.3: (a) An equivalent circuit model of the capacitive coupler. (b) Schematic and signal flow of the coupler terminated by $\lambda/4$ -resonator. (c) Signal flow graph of the coupler at whose port 3 power is reflected by the resonator with a Γ_r probability.

and the fact that the coupler is lossless, namely $S^\dagger S = 1^1$ [42], we can easily find the following trivial properties for S_{ij} :

$$S_{11} = S_{22}, \quad S_{12} = S_{21} \quad (3.16a)$$

$$S_{13} = S_{31} = S_{23} = S_{32} \quad (3.16b)$$

$$|S_{11}|^2 + |S_{22}|^2 + |S_{33}|^2 = 1. \quad (3.16c)$$

These equations simplify the calculation, and the scattering matrix S can be given by

$$S \approx \begin{pmatrix} -i\frac{\delta_0}{2} & 1 - i\frac{\delta_0}{2} & i\sqrt{\delta_0\delta_r} \\ 1 - i\frac{\delta_0}{2} & -i\frac{\delta_0}{2} & i\sqrt{\delta_0\delta_r} \\ i\sqrt{\delta_0\delta_r} & i\sqrt{\delta_0\delta_r} & 1 - \delta_0\delta_r - i2\delta_r \end{pmatrix}, \quad (3.17)$$

where $\delta_0 = \omega C_c Z_0$ and $\delta_r = \omega C_c Z_r$, and we assume that $\delta_0, \delta_r \ll 1$ ($\delta_0, \delta_r \sim 0.01$ in our case).

¹ S^\dagger is the adjoint matrix of S

3.2.2 Reflection Coefficient Γ_r of a $\lambda/4$ -Resonator Terminated by a SQUID

We now connect port 3 to one end of the $\lambda/4$ -resonator, the other end of which is terminated by the SQUID represented as the magnetic flux variable inductance L_Φ , namely $Z_L = i\omega L_\Phi$, as shown in Fig. 3.3 (b). For the case where $\alpha l \ll 1$, $\omega = \omega_0 + \Delta\omega$ ($\Delta\omega/\omega_0 \ll 1$) and $\omega L_\Phi/Z_r \ll 1$, in the same fashion as in Subsec. 3.1.2, the input impedance Z_{in} looking out from port 3 can be written as:

$$Z_{\text{in}} \approx \frac{Z_r}{\alpha l + i \left(\frac{\omega L_\Phi}{Z_r} + \frac{\pi \Delta\omega}{2 \omega_0} \right)}. \quad (3.18)$$

Due to the impedance mismatch, there is reflection at port 3, and the reflection coefficient $\Gamma_r (= a_3/b_3)$ from the load Z_{in} can be given by

$$\Gamma_r = \frac{Z_{\text{in}} - Z_r}{Z_{\text{in}} + Z_r} = \frac{1 - \alpha l - i \left(\frac{\omega L_\Phi}{Z_r} + \frac{\pi \Delta\omega}{2 \omega_0} \right)}{1 + \alpha l + i \left(\frac{\omega L_\Phi}{Z_r} + \frac{\pi \Delta\omega}{2 \omega_0} \right)}. \quad (3.19)$$

For later convenience, we also have the reciprocal of that in the above conditions, which can be reduced to

$$\frac{1}{\Gamma_r} \approx 1 + \frac{\pi}{2Q_i} + i2 \left(\frac{\omega L_\Phi}{Z_r} + \frac{\pi \Delta\omega}{2 \omega_0} \right), \quad (3.20)$$

where we use Eq. 3.15.

3.2.3 Transmission Coefficient t_{21}

In terms of energy flow, we can define the coupling quality factor Q_c as follows. The energy E_{stored} stored in the resonator oscillates with a frequency 2ω , and the fractions, $2(\omega/2\pi)|S_{31}|^2 E_{\text{stored}}$ and $2(\omega/2\pi)|S_{32}|^2 E_{\text{stored}}$, respectively, of E_{stored} leak from port 3 to 1 and 2, and are dissipated at the loads Z_0 terminating port 1 and 2 per second. Recall the definition of Q (see Eq. 3.6), the coupling quality factor Q_c can be defined as:

$$\begin{aligned} Q_c &= \omega \frac{\text{Energy stored in the resonator}}{\text{Energy leaked from port 3 to port 1 and 2 per second}} \\ &= \omega \frac{E_{\text{stored}}}{\frac{2\omega/2\pi|S_{31}|^2 E_{\text{stored}} + 2\omega/2\pi|S_{32}|^2 E_{\text{stored}}}{\pi}} \\ &= \frac{1}{|S_{31}|^2 + |S_{32}|^2}. \end{aligned} \quad (3.21)$$

Thus, substituting the elements of Eq. 3.17 into Eq. 3.21, the coupling quality factor Q_c can be given by

$$Q_c = \frac{\pi}{2\omega^2 C_c^2 Z_0 Z_r}. \quad (3.22)$$

From Eqs. 3.17 and 3.21, the following can be found:

$$S_{31} = i\sqrt{\frac{\pi}{2Q_c}} \quad (3.23a)$$

$$S_{33} = 1 - \frac{\pi}{2Q_c} - i2\delta_r. \quad (3.23b)$$

With the signal flow graph of the system as shown in Fig. 3.3 (c) and the relationship of Eq. 3.16, the total transmission coefficient t_{21} from port 1 to 2 can be given by

$$t_{21} = S_{21} + \frac{S_{31}\Gamma_r S_{23}}{1 - \Gamma_r S_{33}} = S_{21} + \frac{S_{31}^2}{\frac{1}{\Gamma_r} - S_{33}}. \quad (3.24)$$

Substituting Eqs. 3.17, 3.20, and 3.23 into Eq. 3.24, t_{21} can be finally written as:

$$\begin{aligned} t_{21} &\approx 1 - \frac{\frac{Q_t}{Q_c}}{1 + i2Q_t \left(\frac{2}{\pi} \frac{\omega L_\Phi}{Z_r} + \frac{2}{\pi} \delta_r + \frac{\Delta\omega}{\omega_0} \right)} \\ &= 1 - \frac{\frac{Q_t}{Q_c}}{1 + i2Q_t \frac{f-f_r}{f_r}}, \end{aligned} \quad (3.25)$$

where Q_t is the total quality factor defined as

$$\frac{1}{Q_t} = \frac{1}{Q_i} + \frac{1}{Q_c}, \quad (3.26)$$

and f_r ($= \omega_r/2\pi$) is the resonance frequency which can be derived based on the imaginary part of t_{21} being zero at frequency f ($= \omega/2\pi$) $= f_r$, and is given by

$$f_r = \frac{f_0}{1 + 4C_c Z_r f_0 + 4\frac{L_\Phi}{Z_r} f_0}. \quad (3.27)$$

We find the resonance frequency of the network f_r is very close to that of the $\lambda/4$ -resonator f_0 ($= \omega_0/2\pi$).

At the resonance, the magnitude of t_{21} is minimized, and given by

$$t_{21}^{\min} = 1 - \frac{Q_t}{Q_c}. \quad (3.28)$$

Let us introduce another important parameter, the bandwidth BW of the resonance. Equation 3.25 tells us the resonance curve has the well-known notch shape. Therefore the BW is defined as:

$$BW = \frac{f_r}{Q_t}. \quad (3.29)$$

This means that the depth of the transmission power $(1 - |t_{21}|^2)$ normalized to the incident power at the frequency of $(f_r \pm BW)$ is half of $(1 - |t_{21}^{\min}|^2)$. For $Q_t \approx Q_c$ (or $Q_i \gg Q_c$), the BW only depends on the Q_c , and in this case, the BW can be designed by adjusting the Q_c (or C_c).

3.3 Transmission Coefficient Model of a MW-MUX

3.3.1 Network Model of an Asymmetric Resonator

In the discussion so far, we assume that both of the characteristic impedances of port 1 and port 2 are identical to their termination loads Z_0 . Thus, the resonator is completely symmetric. However, it would be almost impossible to achieve such a precise matching in an actual experiment. The resonance dip we measure can be asymmetric due to impedance mismatches between the input and output ports [47, 48]. Here, we model the case where the characteristic impedances of port 1 and port 2 are different from each other and the load impedances Z_0 . In this case, the power wave from each port is reflected at each termination load, that is; we can define the reflection coefficients Γ_1 at port 1 and Γ_2 at port 2. The signal flow graph of this configuration is shown in Fig. 3.4.

3.3.2 Modification of S -parameters

Analyzing the signal flow shown in Fig. 3.4, we can easily modify the S -parameters in Eq. 3.17 to as follows:

$$S'_{11} = S_{11} + S_{21} \frac{\Gamma_2}{1 - S_{22}\Gamma_2} S_{12} \quad (3.30a)$$

$$S'_{12} = S_{12} \quad (3.30b)$$

$$S'_{13} = S_{13} + S_{23} \frac{\Gamma_2}{1 - S_{22}\Gamma_2} S_{12} \quad (3.30c)$$

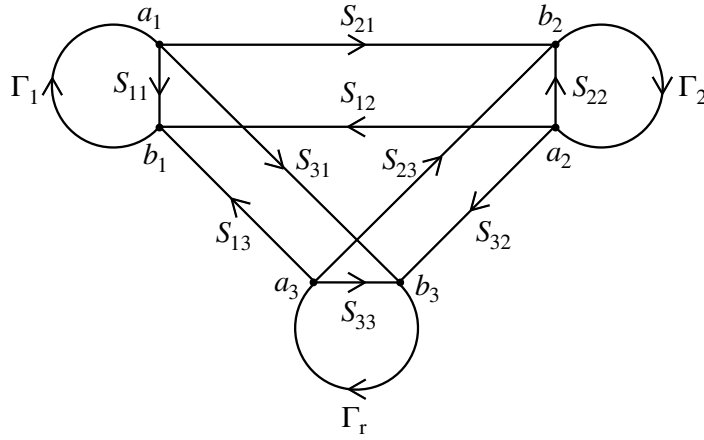


Figure 3.4: Signal flow graph under condition of impedance mismatches between port 1 and port 2.

$$S'_{21} = S_{21} \quad (3.30d)$$

$$S'_{22} = S_{22} + \frac{\Gamma_1}{1 - S_{11}\Gamma_1} S_{21} \quad (3.30e)$$

$$S'_{23} = S_{23} + S_{13} \frac{\Gamma_1}{1 - S_{11}\Gamma_1} S_{21} \quad (3.30f)$$

$$S'_{31} = S_{31} + S_{21} \frac{\Gamma_2}{1 - S_{22}\Gamma_2} S_{32} \quad (3.30g)$$

$$S'_{32} = S_{32} + S_{12} \frac{\Gamma_1}{1 - S_{11}\Gamma_1} S_{31} \quad (3.30h)$$

$$S'_{33} = S_{33}. \quad (3.30i)$$

3.3.3 Transmission Coefficient t'_{21} under Impedance Mismatches

The transmission coefficient should also be modified to

$$t'_{21} = S'_{21} + S'_{31} \frac{\Gamma_r}{1 - S'_{33}\Gamma_r} S'_{23}. \quad (3.31)$$

With Eq. 3.30, the modified transmission coefficient t'_{21} can be rewritten as

$$t'_{21} = S_{21} + \frac{S_{31}^2}{\frac{1}{\Gamma_r} - S_{33}} \left(1 + S_{21} \frac{\Gamma_1}{1 - S_{11}\Gamma_1} \right) \left(1 + S_{21} \frac{\Gamma_2}{1 - S_{22}\Gamma_2} \right). \quad (3.32)$$

Assuming the impedance mismatch is small, namely $\Gamma_1, \Gamma_2 \ll 1$, the second part in the second term in Eq. 3.32 can be reduced to

$$1 + S_{21} \frac{\Gamma_1}{1 - S_{11}\Gamma_1} = \frac{1 + \Gamma_1}{1 + i\frac{\delta_0}{2}\Gamma_1} \approx 1 - i\frac{\delta_0}{2}\Gamma_1 = e^{i\phi_1}, \quad (3.33)$$

where $e^{i\phi_1}$ is a complex number. In the same fashion, the third part in the second term in Eq. 3.32 can be expressed as the same form, or $e^{i\phi_2}$. Let ϕ be $\phi = \phi_1 + \phi_2$, thus, we can finally rewrite t'_{21} as

$$t'_{21} = S_{21} + \frac{S_{31}^2}{\frac{1}{\Gamma_r} - S_{33}} e^{i\phi} = 1 - \frac{\frac{Q_t}{Q_c} e^{i\phi}}{1 + i2Q_t \frac{f-f_r}{f_r}}. \quad (3.34)$$

We regard ϕ as the parameter that quantifies the impedance mismatch, and the resonance circle is rotated by ϕ with respect to 1, namely the off-resonant point ($t_{21}(\pm\infty) = 1$), in the complex plane.

3.3.4 Measured Transmission Coefficient T_{21}

The measured transmission coefficient model T_{21} can be given by

$$T_{21} = A e^{iB} e^{-i2\pi f\tau} \left(1 - \frac{\frac{Q_t}{Q_c} e^{i\phi}}{1 + i2Q_t \frac{f-f_r}{f_r}} \right), \quad (3.35)$$

where A , B , and τ are an additional gain and/or attenuation, a phase shift, and decay time caused by the length of the cable, respectively. A comes from the net gain or attenuation due to the cable loss and the microwave readout components such as an amplifier and an attenuator. Those components can also cause a phase shift of B . τ comes from the shift of the reference plane of the incident and reflection power waves. Equation 3.35 is our transmission coefficient model of a MWMUX in this dissertation, and used to extract the parameters, f_r , Q_t and Q_c , from the measurement of a vector network analyzer (VNA) sweep of transmitted power.

3.3.5 Property of the Transmission Coefficients

At the end of this section, we describe the properties of the transmission coefficient. In Fig. 3.5, we give an example of the plots of (a) resonance circles, (b) amplitudes,

and (c) phases of the transmission coefficients as functions of the frequency f in the following cases: (i) An ideal resonance t_{21} (Eq. 3.25), (ii) an asymmetric resonance t'_{21} (Eq. 3.34), namely the transmission coefficient under impedance mismatches, (iii) an asymmetric resonance with an additional gain A and a phase shift B , $Ae^{iB}t'_{21}$, and (iv) a measured transmission coefficient model T_{21} (Eq. 3.35).

3.4 Dissipationless Radio Frequency (RF) SQUID

The SQUID is built on the phenomena of flux quantization and the Josephson effect. In this section, we will derive the equations related to the SQUID used in MWMUX. We use an RF-SQUID as a sensitive flux-variable inductor responding to the magnetic flux threading the SQUID loop with a period of one flux quantum to detect the TES signals. The Josephson relations imply the Josephson junction (JJ) acts as the flux-variable inductor, and the flux quantization tells us its response being periodic. We start with the calculation of the flux quantization of the superconducting loop, and the derivation of the Josephson inductance.

3.4.1 Flux Quantization

The magnetic flux Φ contained in a closed superconducting loop can only take values that are integer multiples of the flux quantum $\Phi_0 = h/2e \approx 2.07 \times 10^{-15}$ Wb, where $h = 2\pi\hbar$ and e are Planck's constant and the electronic charge, respectively. It can be easily derived as follows by using the fact that a macroscopic wave function or order parameter $\Psi(\vec{r}, t)$ must be single-valued in going once around a superconducting loop. Consider the situation that a superconducting loop exists in a magnetic field. Let the order parameter $\Psi(\vec{r}, t)$ be

$$\Psi(\vec{r}, t) = \Psi_0(\vec{r}, t)e^{i\psi(\vec{r}, t)} \quad (3.36)$$

where Ψ_0^2 is the Cooper-pair density and $\psi(\vec{r}, t)$ is the phase of this wave function. According to basic quantum mechanics, the probability current \vec{J} for a system in an external electromagnetic field in SI units can be written as

$$\vec{J} = \frac{1}{2m} \left(\Psi^* \hat{p} \Psi - \Psi \hat{p} \Psi^* - 2q\vec{A}\Psi^*\Psi \right) \quad (3.37)$$

where m , q , \hat{p} and \vec{A} are the Cooper-pair mass, the Cooper-pair charge (which is identical to $2e$ in this case), the momentum operator (defined as $\hat{p} = -i\hbar\vec{\nabla}$ with gradient operator $\vec{\nabla}$), and the vector potential, respectively. Substituting Eq. 3.36 into Eq. 3.37 and using the fact that there exists a path where $\vec{J} = 0$ around the

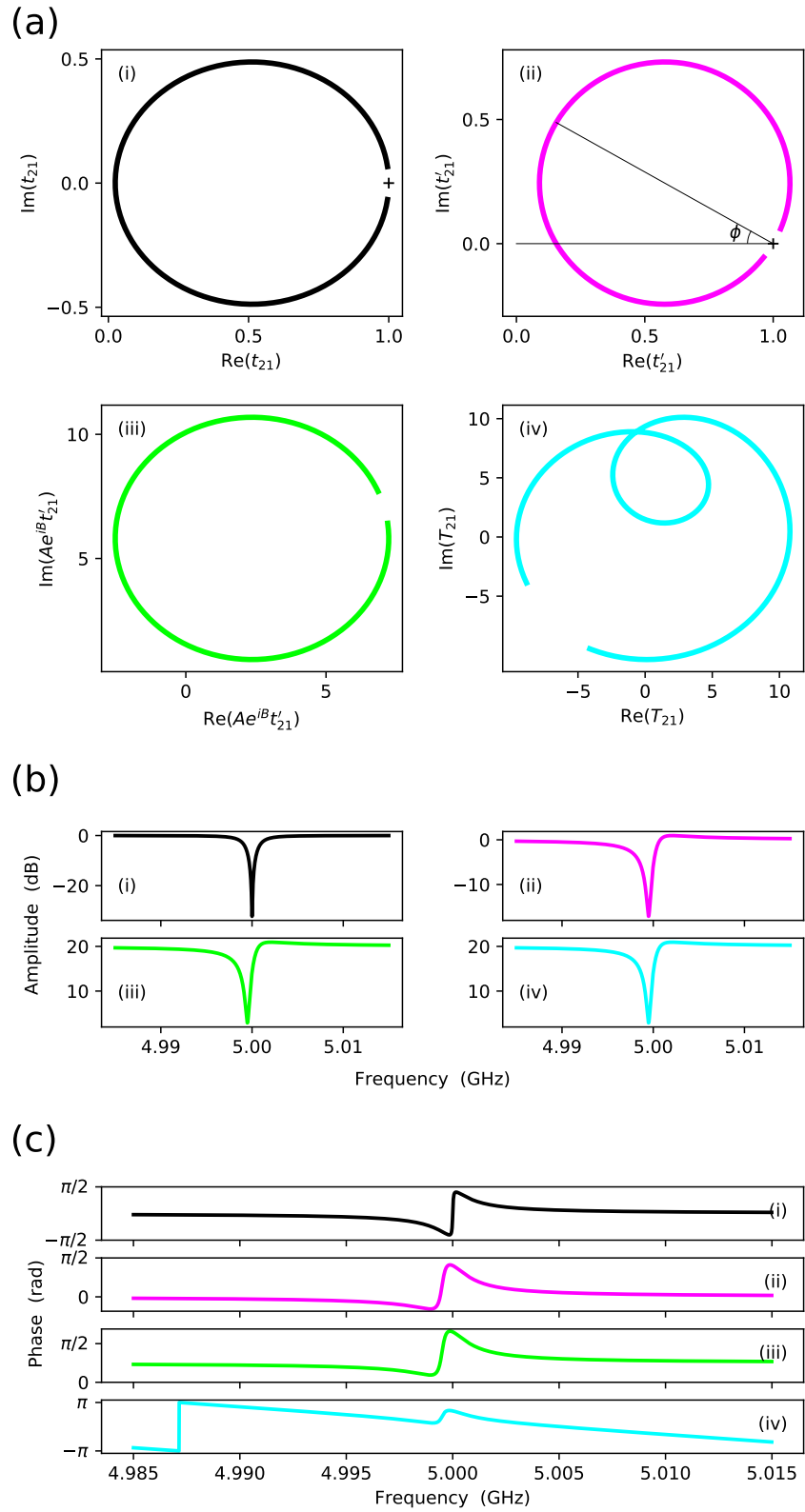


Figure 3.5: Example plots of the transmission coefficients under the assumption that $f_r = 5.0$ GHz, $Q_i = 10^5$, $Q_c = 2500$, $A = 10$, $B = \pi/4$, $\phi = -\pi/6$, $\tau = 30$ ns. (a), (b), and (c) are resonance circles, amplitudes, and phases of the transmission coefficient, respectively.

whole loop due to the supercurrent only flowing the surface of the loop, we can obtain the phase gradient

$$\vec{\nabla}\psi = \frac{2e}{\hbar}\vec{A}. \quad (3.38)$$

Moving once around a closed path inside the superconductor, the phase can only vary by multiples of 2π . Thus, the integral of the phase gradient along the path is given by

$$\oint \vec{\nabla}\psi \cdot d\vec{l} = \frac{2e}{\hbar} \oint \vec{A} \cdot d\vec{l} = \frac{2e}{\hbar}\Phi = 2\pi n \quad (n = 0, \pm 1, \pm 2, \dots), \quad (3.39)$$

and we finally find

$$\Phi = n\Phi_0, \quad (3.40)$$

where Φ is the magnetic flux threading the superconducting loop, quantized to Φ_0 .

3.4.2 Josephson Inductance

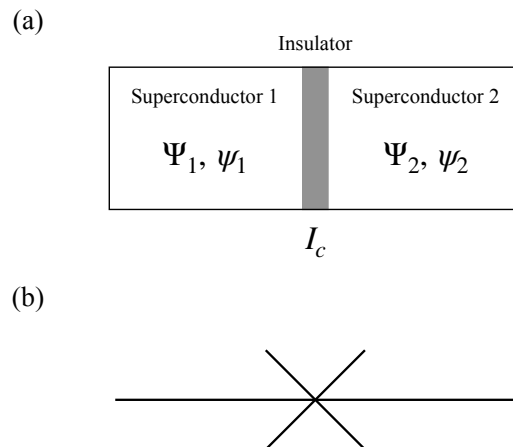


Figure 3.6: (a) Schematic of a Josephson junction (SIS; Super/Insulator/Super). Two superconductors, which are characterized by wave functions $\Psi_{1,2}$ and phases $\psi_{1,2}$, are separated by insulator. (b) Circuit symbol of the Josephson junction.

The Josephson junction [49, 50] consists of two weakly coupled superconducting electrodes as shown in Fig. 3.6. Josephson constructed the theory for Cooper pairs tunneling between two superconductors separated by a barrier in 1962. According to his theory, the *Josephson relations*, the two equations, are given as follows: the current I flowing through a junction is caused by the phase difference $\delta = \psi_1 - \psi_2$

between the two superconducting electrodes whose phases are ψ_1 and ψ_2 , and can be given by

$$I = I_c \sin \delta, \quad (3.41)$$

where I_c is the critical current of the junction. In the presence of a voltage V across the electrodes, the phase difference δ evolves with time t , and can be written as

$$\frac{d\delta}{dt} = \frac{2eV}{\hbar}. \quad (3.42)$$

These equations imply the junction has an effective self-inductance. Substituting Eq. 3.42 into the time differentiation of Eq. 3.41, we find the voltage-current relation as below

$$V = \frac{\hbar}{2eI_c \cos \delta} \frac{dI}{dt}. \quad (3.43)$$

From the relation above, the Josephson inductance $L(\delta)$ can be given by

$$L(\delta) = L_J \sec \delta, \quad (3.44)$$

where

$$L_J \equiv \frac{\hbar}{2eI_c} = \frac{\Phi_0}{2\pi I_c}. \quad (3.45)$$

3.4.3 RF-SQUID: Superconducting Loop with One Junction

The RF-SQUID employs only a single junction in a superconducting loop, as shown in Fig. 3.7. We assume that a one junction superconducting loop with its loop inductance L_S is put in an applied external flux Φ_a , as shown in Fig. 3.7 (b). The total magnetic flux Φ in the loop has contributions from the applied magnetic field Φ_a and from the circulating current I . Therefore Φ can be given by

$$\Phi = \Phi_a + L_S I = \Phi_a + L_S I_c \sin \delta. \quad (3.46)$$

Let δ be the phase difference across the junction, then using Eq. 3.39, the phase variance around the loop can be calculated as

$$\delta + \oint \vec{\nabla} \psi \cdot d\vec{l} = \delta + \frac{2e}{\hbar} \oint \vec{A} \cdot d\vec{l} = \delta + 2\pi \frac{\Phi}{\Phi_0} \quad (3.47)$$

Due to the phase variance around the loop that must be multiples of 2π from the same discussion as above, this equation must be equal to $2\pi n$. By rearranging the equation, δ can be written as

$$\delta = 2\pi n - 2\pi \frac{\Phi}{\Phi_0}. \quad (3.48)$$

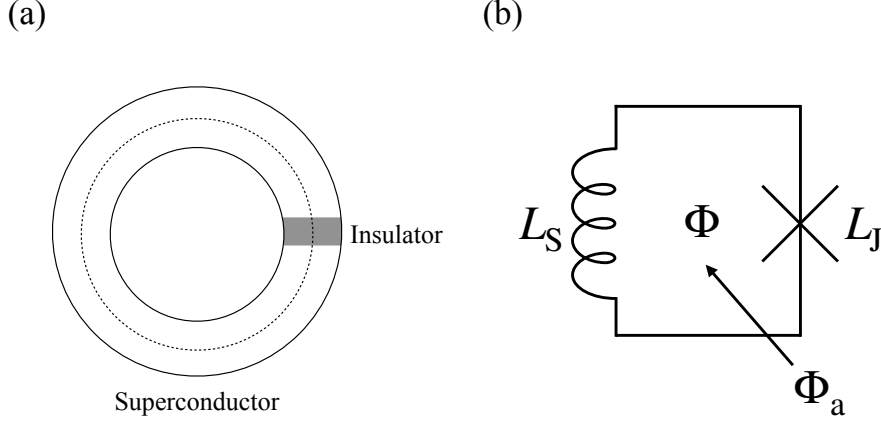


Figure 3.7: (a) Schematic of an RF-SQUID. (b) Circuit symbol of an RF-SQUID with its loop inductance L_S .

Substituting Eq. 3.48 into Eq. 3.46 and rearranging, the applied flux Φ_a into the RF-SQUID can be written as

$$\Phi_a = \Phi - L_S I_c \sin \left(2\pi n - 2\pi \frac{\Phi}{\Phi_0} \right) = \Phi + L_S I_c \sin \left(2\pi \frac{\Phi}{\Phi_0} \right). \quad (3.49)$$

Let us introduce an important parameter, the hysteresis parameter, defined as

$$\lambda \equiv L_S / L_J, \quad (3.50)$$

which quantifies whether the RF-SQUID is hysteretic or not. To avoid hysteresis, the total flux must be a single-valued function of the applied flux. On the other hand, the applied flux Φ_a must monotonically increase with respect to the total flux Φ regardless of the value of Φ , that is the minimum value of $d\Phi_a/d\Phi$ must be positive,

$$\left(\frac{d\Phi_a}{d\Phi} \right)_{\min} = \left(1 + 2\pi \frac{L_S I_c}{\Phi_0} \cos \left(2\pi \frac{\Phi}{\Phi_0} \right) \right)_{\min} \quad (3.51)$$

$$= 1 - \lambda > 0. \quad (3.52)$$

Here we use Eqs. 3.45 and 3.50. We get the boundary condition of $\lambda = 1$. Thus, when $\lambda < 1$, the RF-SQUID is non-hysteretic, and when $\lambda > 1$, the RF-SQUID is

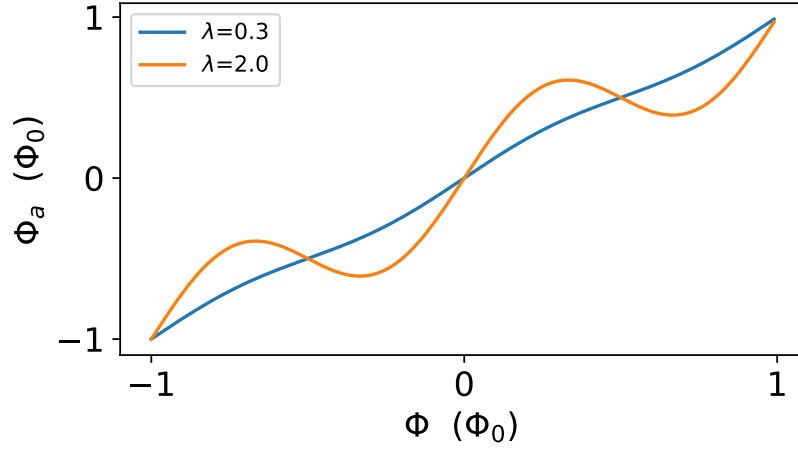


Figure 3.8: The relation between the total flux Φ and the applied flux Φ_a .

hysteretic and can enact flux jumps between metastable states. Figure 3.8 shows the relation between the total flux and the applied flux for two values of λ . In our application, $\lambda < 1$ is required, and we can adjust the two parameters, I_c and L_S , to achieve the requirement.

3.4.4 SQUID Inductance $L(\Phi)$: Flux-Variable Inductance

We use an RF-SQUID with an adjustable fractional inductance, as shown in Fig. 3.9. Here, let us introduce a fractional parameter “ a ” of the SQUID-loop inductance. The SQUID-loop inductance L_S is divided into a ratio of a to $(1 - a)$ in parallel, therefore the total SQUID inductance $L(\Phi)$ as a function of magnetic flux Φ threading the loop can be written as

$$L(\Phi) = L_S(1 - a) \frac{1 + a\lambda \cos\left(2\pi \frac{\Phi}{\Phi_0}\right)}{1 + \lambda \cos\left(2\pi \frac{\Phi}{\Phi_0}\right)}. \quad (3.53)$$

As shown in Fig. 3.10, the SQUID inductance $L(\Phi)$ nearly sinusoidally responds to magnetic flux with a period of one flux quantum (Φ_0). The peak-to-peak change in inductance L_{pp} can be given by

$$L_{pp} = L(\Phi_0/2) - L(0) = L_S(1 - a)^2 \frac{2\lambda}{1 - \lambda^2}. \quad (3.54)$$

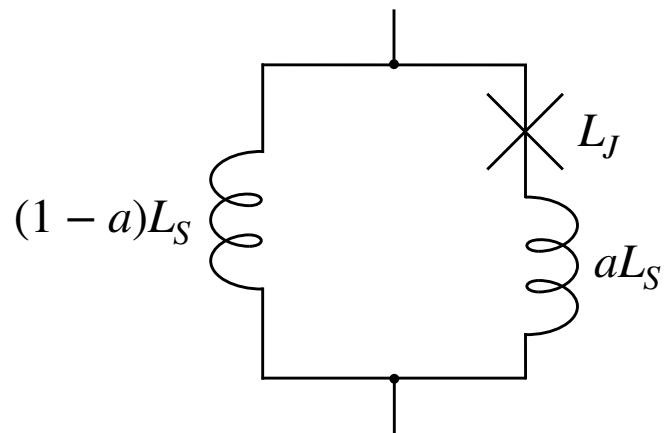


Figure 3.9: Circuit diagram of an RF-SQUID with fractional parameter a .

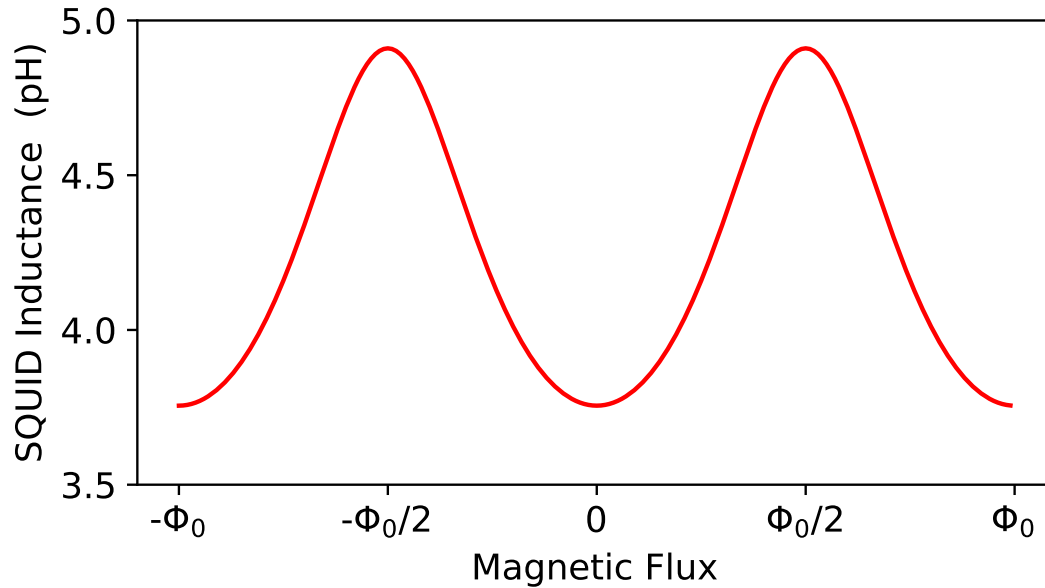


Figure 3.10: Variation of SQUID inductance with input magnetic flux for $L_S = 9.88$ pH, $a = 0.579$, $\lambda = 0.3$ which come from typical design values.

3.5 Resonance Frequency Variations with Respect to Flux Signal Input

In the discussion above, we derived the resonance frequency f_r of MWMUX, namely the quarter-wave resonator terminated by RF-SQUID in Eq. 3.27 and the SQUID inductance $L(\Phi)$ in Eq. 3.53. Here, we describe variation of resonance frequency with respect to the SQUID inductance change with input flux.

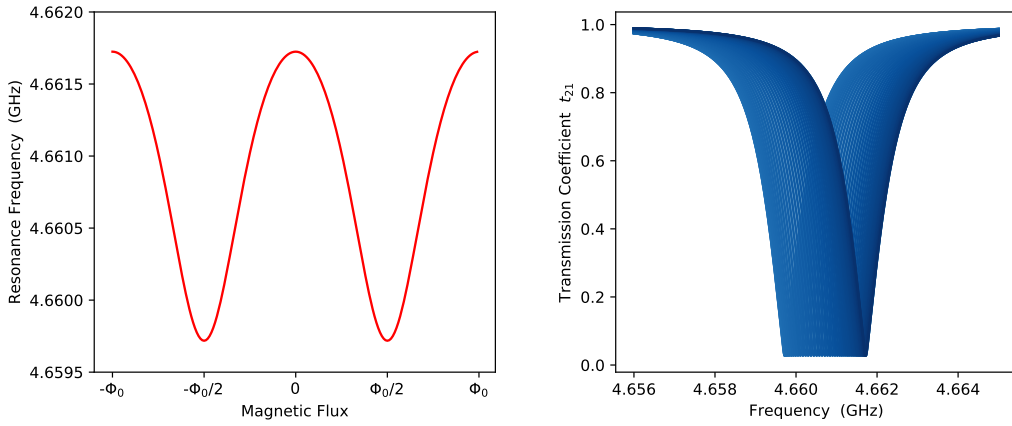


Figure 3.11: Variation of resonance frequency f_r (*left*) and transmission coefficient t_{21} (*right*) with respect to input magnetic flux for $L_S = 9.88$ pH, $a = 0.579$, $\lambda = 0.3$, $C_c = 16.21$ fF, $f_0 = 4.74$ GHz, $Z_0 = Z_r = 50 \Omega$ which come from typical design values and an assumed value of $Q_i = 10^5$.

Substituting Eq. 3.53 into Eq. 3.27, the dependance of resonance frequency on input flux can be obtained, and it is a sinusoidal function, as shown in Fig. 3.11 (*left*). The resonance frequency f_r is maximum at the input flux of $\Phi = (n+1/2)\Phi_0$ and is minimum at $\Phi = n\Phi_0$, where $n \in \mathbb{Z}$. Hence, the maximum resonance frequency shift Δf_r caused by input flux can be calculated as

$$\Delta f_r = \left| \frac{df_r}{dL} \right| L_{pp} = \frac{8\lambda L_S (1-a)^2}{Z_r (1-\lambda^2)} f_r^2, \quad (3.55)$$

where we used Eq. 3.54. This parameter is a crucial one. In general, we target the coupling strength, defined as $\eta \equiv \Delta f_r / BW$, near unity ($\eta \approx 1$) by making full use of the SQUID gain.

3.6 Flux-Ramp Modulation (FRM)

The SQUID response is periodic and, therefore, nonlinear with respect to the input signal, so a linearizing readout technique is required for SQUID operation. In the DC-SQUID regime, the SQUID response is traditionally linearized with a mature flux-locked loop (FLL) technique [51]. The FLL maintains the SQUID working point at a specific bias point by feeding the SQUID output back inverted so that an input signal is canceled out. However, the FLL requires separate feedback wires to every SQUID, and these extra wires make multiplexing more challenging. Therefore FLL is incompatible with our purpose of the reduction of cables.

An alternative method that is called *flux-ramp modulation* (FRM) has been proposed and demonstrated [35, 34]. In the FRM regime, as shown in Fig. 3.12, we constantly apply a periodic flux ramp to modulate the SQUID response. An input signal added to the flux ramp can be regarded as a flux offset and induces a phase shift in the SQUID response. Because the phase shift is linearly proportional to the input signal, we can extract the value by tracing the phase shift. We usually extract the phase shift by averaging data points in a cycle. Therefore the sampling frequency in MWMUX is the ramp frequency itself. This technique is compatible with MWMUX because all SQUIDs can be linearized with a single wire pair.

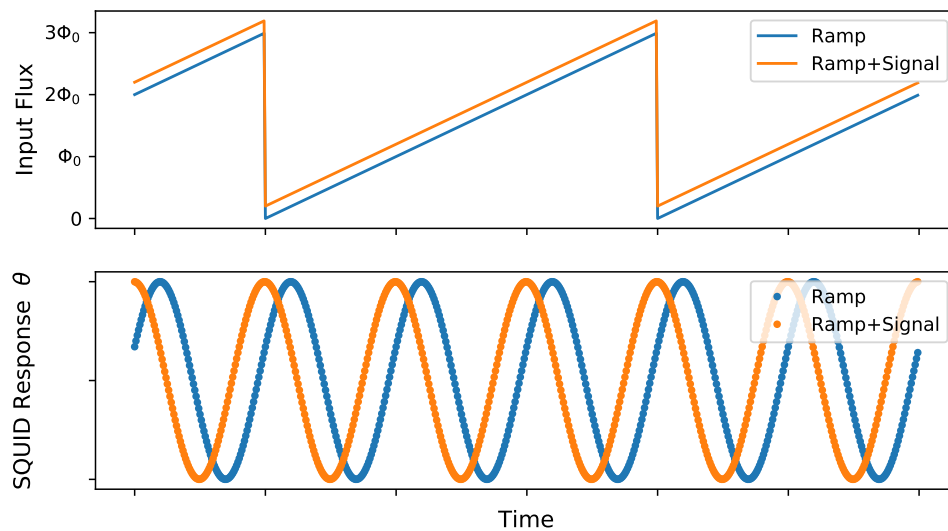


Figure 3.12: Flux-ramp modulation.

The FRM algorithm that must identify phase shifts of the SQUID response to flux ramp between ramp periods cannot distinguish a phase shift of more/less

than $\Phi/2$ in one cycle. This introduces a restriction on the input signal slew rate dI_{tes}/dt , where I_{tes} is a current-pulse height of TES signal. A flux-input signal Φ to SQUID in a ramp cycle Δt_{ramp} cannot exceed $\Phi/2$. Therefore the slew-rate restriction can be calculated as

$$\begin{aligned} \Phi = M_{\text{in}} \frac{dI_{\text{tes}}}{dt} \Delta t_{\text{ramp}} &< \frac{\Phi_0}{2} \\ \frac{dI_{\text{tes}}}{dt} &< \frac{\Phi_0}{2M_{\text{in}}\Delta t_{\text{ramp}}} = \frac{\Phi_0 f_{\text{ramp}}}{2M_{\text{in}}}, \end{aligned} \quad (3.56)$$

where M_{in} , f_{ramp} are the mutual inductance between the TES signal circuit and the SQUID, and the flux-ramp frequency ($f_{\text{ramp}} = 1/\Delta t_{\text{ramp}}$), respectively.

Chapter 4

MWMUX01: Conceptual Design of MWMUX for Readout of a TES X-ray Microcalorimeter

4.1 Key Component: SQUID Directly Coupled to Resonator

4.1.1 Background

Though MWMUX is intended as a readout circuit of the next-generation large-format TES arrays, this broadband multiplexing can be achieved only by optimizing the SQUID-resonator coupling strength to the same level at different resonance frequencies for all channels. We have investigated MWMUX with microstrip-type SQUID [39], which can be designed much more simply and accurately than the planar SQUIDs generally used [34]. Also, we have proposed direct SQUID-resonator coupling with an adjustable parameter in contrast to conventional inductive coupling (see Fig. 4.1). This has, however, never been demonstrated before. Here, we give the first demonstration that the SQUID-resonator coupling strength can be optimized simply and accurately by varying only the position of a ground-via on the microstrip loop for all channels.

4.1.2 SQUID Design

We designed 16-channel MWMUX chips including test elements on which each SQUID connected to a pair of terminals to inject current for the purpose of evaluating of aL_S , $(1-a)L_S$ and L_S [39]. The chips consisted of three Nb electrode layers with SiO_2 insulation layers stacked on the Si substrate and were fabricated by Nb-

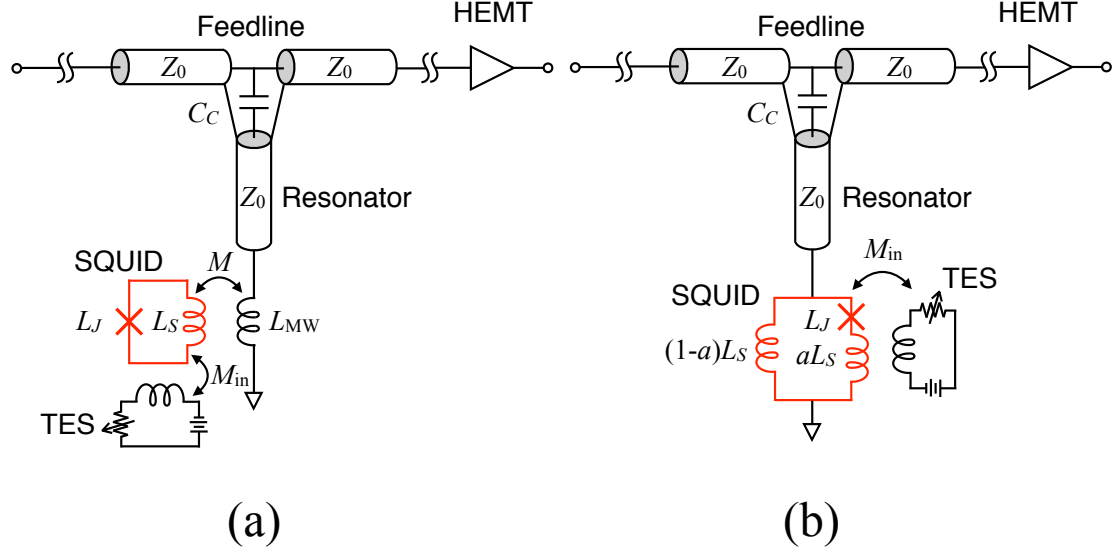


Figure 4.1: Two ways of SQUID-resonator coupling. (a) Conventional inductive coupling between SQUID and resonator. (b) Advanced direct coupling we have proposed [39]. The coupling strength can be characterized by means of a fractional parameter a [52].

based superconducting circuit technology. The critical current of the Josephson junction I_c is designed to be $10 \mu\text{A}$, which is realized by $4 \mu\text{m}^2$ area and 250 A/cm^2 critical current density. Each SQUID acts as a first-order parallel gradiometer, which is formed by two symmetric stripline loops in parallel. Figure 4.2 (a) shows a photograph of one side of the two loops, which consist of $20 \mu\text{m}$ wide Nb stripline on a ground plane. The loops are bent to prevent interference between adjacent channels. Each loop has two stripline coils; one is connected to the resonator via the junction and the other directly. The former and latter inductances are respectively denoted by aL_S and $(1 - a)L_S$ as in Fig. 4.2 (b). The inductances can be varied by adjusting the length of the microstrip line with an inductance per unit length L_{unit} given by [53]

$$L_{\text{unit}} = \frac{\mu_0 D}{w K_f} \quad (4.1)$$

with

$$D \approx h + 2\lambda_L, \quad (4.2)$$

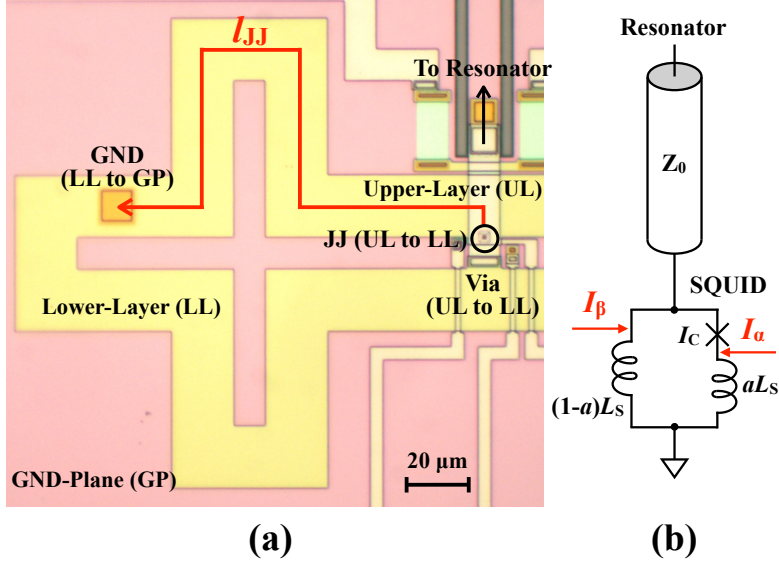


Figure 4.2: (a) A photograph of SQUID fabricated for evaluation of SQUID loop and fractional inductances. The length from Josephson junction (JJ) to the ground (GND) l_{JJ} is defined as the red arrow running through the center of the strip. (b) Equivalent circuit schematic of a SQUID. The two red arrows indicate current-injection points. The values of aL_S and $(1-a)L_S$ can be obtained by injecting current I_α and I_β , respectively [52].

for our case in which the thickness of both electrodes are sufficiently larger than λ_L . Here, μ_0 , $w = 20 \mu\text{m}$ and $K_f = 1.1$ are respectively the permeability of free space, the stripline width and the fringe coefficient. $h = 300 \text{ nm}$ and $\lambda_L = 39 \text{ nm}$ [54] are the thickness of the insulator, and the magnetic penetration depth of the electrode beneath and above the insulator, respectively. Considering the loop length l and an extra inductance L_{ext} due to the fact that the L_{unit} value of the common bridge of the parallel-loop gradiometer differs from L_{unit} of the main loop, the loop inductance L_S can be written in the form

$$L_S = L_{\text{unit}}l + L_{\text{ext}}. \quad (4.3)$$

In our case, L_{unit} and L_{ext} are calculated as $0.011 \text{ pH}/\mu\text{m}$ and 0.52 pH , respectively. To satisfy the hysteresis parameter $\lambda \approx 0.2$, we determined that the loop length must be $l = 540 \mu\text{m}$ to get the value of $L_S = 6.5 \text{ pH}$. Our goal is to demonstrate that only varying the position of the ground via on the SQUID loop can optimize the fractional parameter a . For this purpose, we prepared seven test elements which have different pairs of aL_S and $(1-a)L_S$ with a common value of $l = 540 \mu\text{m}$.

Each of the seven test elements has a different SQUID geometry on the basis of $l_{JJ} = 161, 210, 245, 318, 350, 459$ and $466 \mu\text{m}$, where l_{JJ} is the length from the junction to the ground (GND) defined as the red arrow running through the center of the stripline in Fig. 4.2 (a).

By way of extracting each pair of inductances experimentally, a set of three terminals for current injection is connected to each SQUID of seven test elements, as in Fig. 4.2. One terminal is connected to the ground plane, another is connected to the point between the junction and the fractional inductance aL_S , and the other is connected to the end between the junction and the fractional inductance $(1 - a)L_S$. The inductances can be extracted from the periodic response of the SQUID as a function of the current flowing through two of these three terminals.

In conventional inductive coupling, each pixel has unique values of M (a mutual inductance that manages SQUID-resonator coupling) and resulting coil dimensions of L_{MW} (the self inductance of coil for SQUID-resonator coupling). Especially for a large-format array, this can lead to the design complexity and deviation from the designed L_{MW} and M . In our advanced design method, we can change the fractional parameters a , keeping identical structure, shape, and dimensions of the SQUID for all pixels except only for varying the GND position. In our design regime, the fractional parameter a could be modified in the range from 0.04 to 0.87.

4.1.3 Experimental Evaluation & Validity of Design

To validate our design in terms of a , a pair of fractional inductances aL_S and $(1 - a)L_S$ was evaluated as a function of l_{JJ} . These inductances were extracted by measuring the periodic $\theta-I_\alpha$ and $\theta-I_\beta$ relations by means of the frequency-dependent transmitted signal through the microwave feedline loaded by seven kinds of the test-element SQUID on one of the 16-channel MWMUX chips we developed.

The chip was mounted on a sample holder that was screened with a magnetic shield and cooled in a Gifford-McMahon refrigerator down to 4 K. A microwave signal with power -50 dBm from a vector network analyzer (VNA) was injected into the cryostat, damped via a 30 dB attenuator, and launched along the feedline. The transmitted signal from the chip was returned to the VNA through a cryogenic HEMT amplifier with ~ 30 dB gain, and ~ 7 K noise temperature, and a ~ 40 dB gain amplifier at room temperature. A current source at room temperature was electrically connected to the terminals on the SQUID by way of a printed circuit board attached to the sample holder. By stepwise applying a static injection current in the range from -2 to 2 mA to the terminals of each test element and acquiring transmission amplitude and phase at a fixed frequency, we obtained periodic responses of the SQUID depending on the injected current and extracted the inductances by dividing those periods by Φ_0 .

Figure 4.3 illustrates the l_{JJ} dependence of both inductances of the fractional and total loop. Linearly with l_{JJ} , aL_S increases and $(1-a)L_S$ decreases. From the slope of the aL_S-l_{JJ} and $(1-a)L_S-l_{JJ}$ relations, L_{unit} is evaluated as $L_{\text{unit}} = 0.010 \text{ pH}/\mu\text{m}$ and $L_{\text{unit}} = 0.0099 \text{ pH}/\mu\text{m}$, respectively. From these L_{unit} values and Eqs. 4.1 and 4.2, the depth $h+2\lambda_L$ is estimated to be 0.34 and $0.33 \mu\text{m}$ for aL_S and $(1-a)L_S$, respectively. This difference may be due to the distribution of $h+2\lambda_L$ on the same SQUID, resulting in the weak dependence of $L_S = aL_S + (1-a)L_S$ on l_{JJ} shown in Fig. 4.3. From our experimental results in Fig. 4.3, the loop inductance of $L_S = 6.2 \text{ pH}$ with the extra inductance $L_{\text{ext}} = 0.90 \text{ pH}$ was obtained. Although the data for two of the seven test elements are incomplete, this does not affect these results.

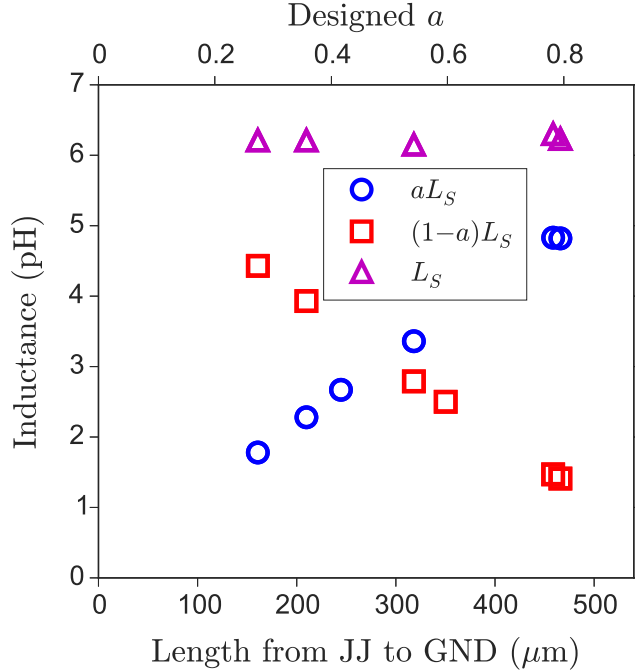


Figure 4.3: Experimental SQUID inductance vs. l_{JJ} and designed a . Blue circle, red square and magenta triangle denote aL_S , $(1-a)L_S$ and L_S , respectively [52].

Figure 4.4 shows the relationship between the fractional parameters a and the length from JJ to GND l_{JJ} . The experimental values were obtained by dividing the fractional inductance aL_S by the loop inductance L_S . Open circles denote the experimental values of a that were obtained in the range from 0.29 to 0.77 as a function of l_{JJ} ranging from 161 to 466 μm . A solid line designates the $a-l_{JJ}$ relation based on Eq. 4.3, modified by the replacement of L_S and l with

aL_S and l_{JJ} , respectively, with $L_{\text{unit}} = 0.011 \text{ pH}/\mu\text{m}$ and $L_{\text{ext}} = 0 \text{ pH}$. Figure 4.4 indicates that the experimental a is in good agreement with the design value within $-3/+10\%$. Equation 3.55 indicates that $(1 - a)$ should be proportional to $1/f_r$ in order to keep Δf_r constant.

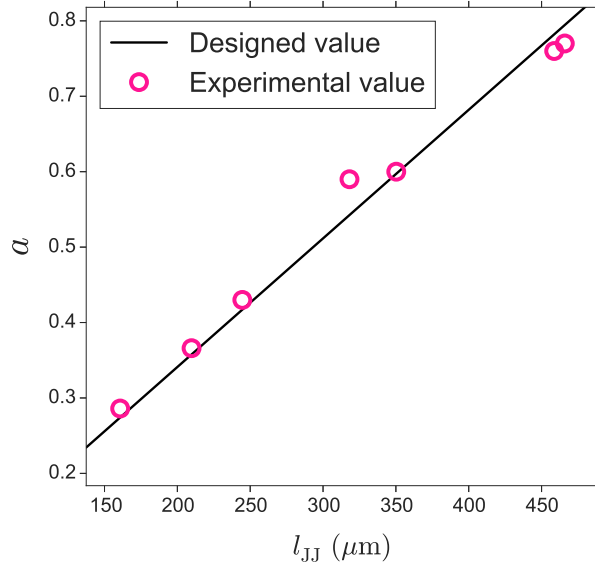


Figure 4.4: Experimental (open-circles) and designed (solid line) fractional parameter a vs. l_{JJ} . Due to the experimental setup, two of seven test elements, $l_{JJ} = 245$ and $350 \mu\text{m}$, were evaluated for only one side of the fractional SQUID loop inductance. Therefore, the other sides of these were estimated by assuming that the total SQUID loop inductance is 6.2 pH , which is the average value calculated from the others [52].

4.2 Overall Design of MWMUX Chip for Readout of X-ray TES

4.2.1 Frequency Allocation

We present a summary of the design of MWMUX01 and experimental evaluations of it. In order to take enough samples of a pulse of our TES with a rise time of $\sim 10 \mu\text{s}$ so as not to degrade energy resolution, we chose the sampling rate, namely the flux ramp frequency f_{ramp} , of 480 kHz derived from our simulation. A resonator bandwidth BW of 3 MHz allows for a $3\Phi_0$ flux ramp frequency of

480 kHz, so we targeted $BW \approx 3$ MHz. For proper readout operation, to make full use of the SQUID gain, we designed the ratio of $\Delta f_r/BW \sim 1$, where Δf_r is the maximum resonance frequency shift due to the flux applied to the SQUID; Δf_r is proportional to $\lambda L_S/(1 - \lambda^2)$ with $\lambda \equiv 2\pi I_c L_S/\Phi_0$. The experimental value of Δf_r can be shifted from the designed Δf_r if the experimental critical current of the Josephson junction I_c and/or SQUID loop inductance L_S are different from the designed values.

4.2.2 Coupling Capacitor: Resonator-Feedline Coupling

To obtain a large BW , the coupling capacitor C_c should be enlarged. We adopt an interdigital capacitor as shown in Fig. 4.5 (left). Using the electromagnetic simulation software *Sonnet*, we investigated the relationship between the finger length of the capacitor and capacitance, and found the relation as follows:

$$\left(\frac{C_c}{1 \text{ fF}}\right) = 0.23 \left(\frac{D_c}{1 \mu\text{m}}\right) + 0.91, \quad (4.4)$$

where D_c is the finger length of the interdigital coupling capacitor. Figure 4.5 (right) shows the simulation result.

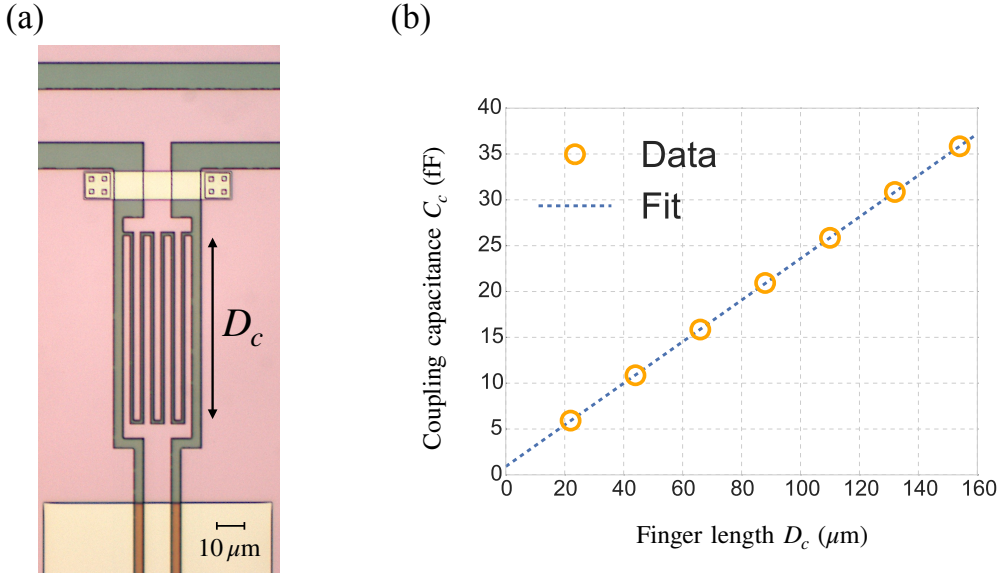


Figure 4.5: (a) Micrograph of a coupling capacitor and the definition of the finger length D_c . (b) The obtained coupling capacitance C_c with respect to D_c from electromagnetic simulation.

4.3 Performance Evaluation

Figure 4.6 (*Left*) shows a vector network analyzer sweep of the microwave SQUID multiplexer with the two-port scattering parameters for transmission ($|S_{21}|^2$) of 16 resonators. Figure 4.6 (*Right*) shows the measured resonance frequency shift Δf_r due to a flux of half of a flux quantum applied to the SQUID at the resonator with resonance frequency of ~ 5.29 GHz. The resonators were placed with a spacing of 40 ± 4 MHz. The bandwidth of the resonators was 4 ± 1 MHz except for six channels, which had values of ~ 6 MHz for the unloaded quality factor Q_i of 2000–9000. Also, the maximum resonance frequency shift Δf_r was ~ 1.5 MHz. Thus, the signal to noise ratio S/N is roughly 60–70% of the design value. With a typical input coupling of $M_{in} = 63$ pH, the upper limit of an input-signal slew rate for accurate flux-ramp demodulation [35] is about 8 A/s, which is acceptable for the TES peak slew rate of ~ 2 A/s.

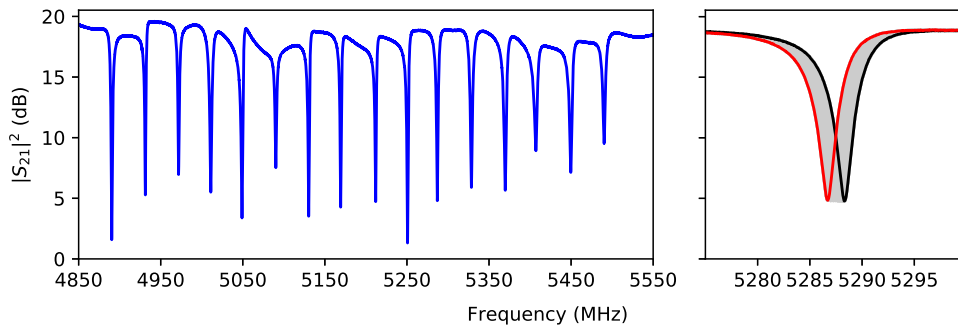


Figure 4.6: (*Left*) The measured $|S_{21}|^2$ as a function of frequency at a bath temperature of 100 mK, with -71 dBm carrier power at the input to the feedline on the chip. (*Right*) The measured maximum resonance frequency shift Δf_r due to the flux applied to the SQUID at the resonator with resonance frequency of ~ 5.29 GHz. The resonance frequency changes between the *red* and *black* lines, and the typical value of Δf_r is 1.5 MHz [55].

4.4 Single-pixel TES Readout with MWMUX01

4.4.1 Experimental Setup

Photographs of an assembled sample box for TES readout with microwave SQUID multiplexer and its equivalent circuit are shown in Fig. 4.7.

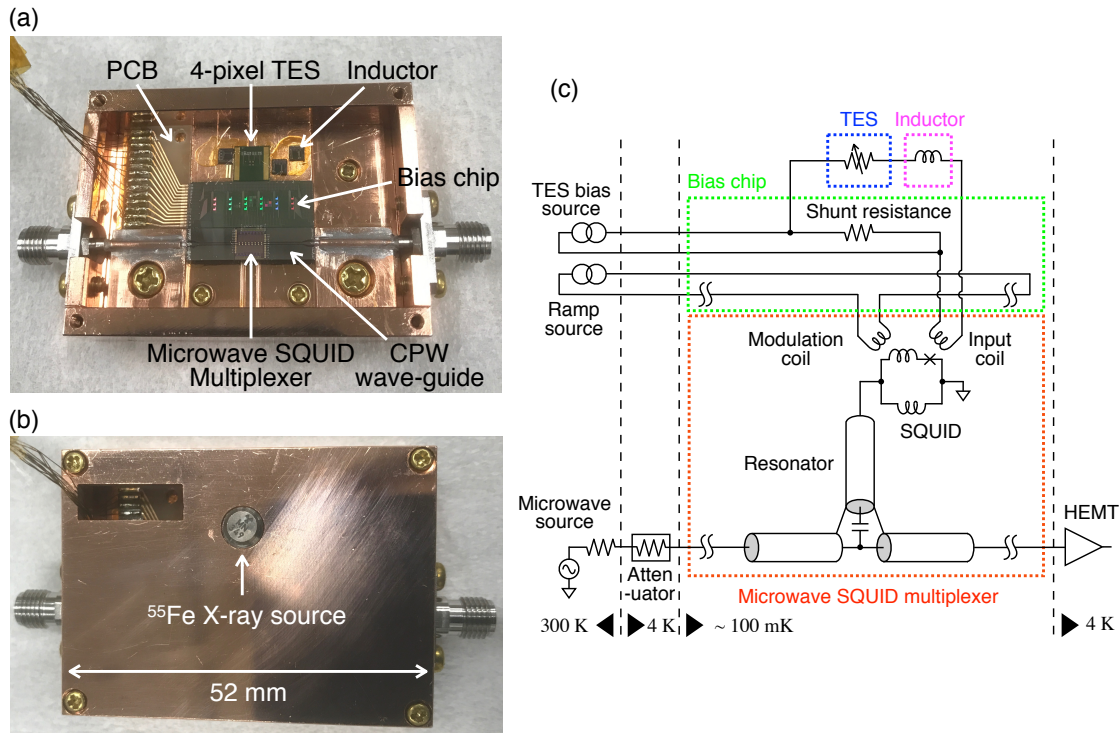


Figure 4.7: (a) Photograph of the cryogenic sample box containing the 4-pixel TES chip developed in ISAS, three inductor chips, bias chip, printed circuit board (PCB), two coplanar-waveguide (CPW) chips and the microwave SQUID multiplexer chip. The PCB is electrically connected to the TES-bias current source and ramp current source at room temperature. The bias chip consists of shunt resistances and a flux-ramp modulation (FRM) line connecting the ramp current source at room temperature with the modulation coils formed on the microwave SQUID multiplexer chip. (b) Photograph of the sample box covered with the lid on which an ^{55}Fe X-ray source is mounted. (c) Schematic representation of one channel microwave SQUID multiplexing circuit with TES. The arrangement corresponds to that of (a) [55].

The TES used in this experiment, developed by ISAS/JAXA [56, 57], is a Ti (40 nm)/Au (100 nm) bilayer with a superconducting transition temperature and a normal resistance R_n of 165 mK and 60 m Ω , respectively. The TES chip connects to an inductor chip of inductance 250 nH; to a bias-chip which consists of shunt resistances and a route for a flux-ramp signal; and finally to a MWMUX01 chip. The detector bias current and the flux-ramp signal at room temperature are respectively applied to the TES and the SQUIDS at the cold stage by way of a printed circuit board attached to the sample box. The microwave tone with ~ -71 dBm

per tone is launched along the feedline on the multiplexing chip, through the SMA connector with coax to a coplanar waveguide chip connected to the multiplexing chip. An ^{55}Fe for X-ray source is screwed on a lid of the sample box, and the typical count rate on the detector is ~ 0.8 counts/s. We mounted the sample box, screened with a magnetic shield, in an adiabatic demagnetization refrigerator (ADR) that provides a temperature of 90 mK with a typical stability of $\sim 90 \mu\text{K}$ rms that is dominated by the accuracy of the temperature controller used.

4.4.2 Result: Pulse Detection with MWMUX01

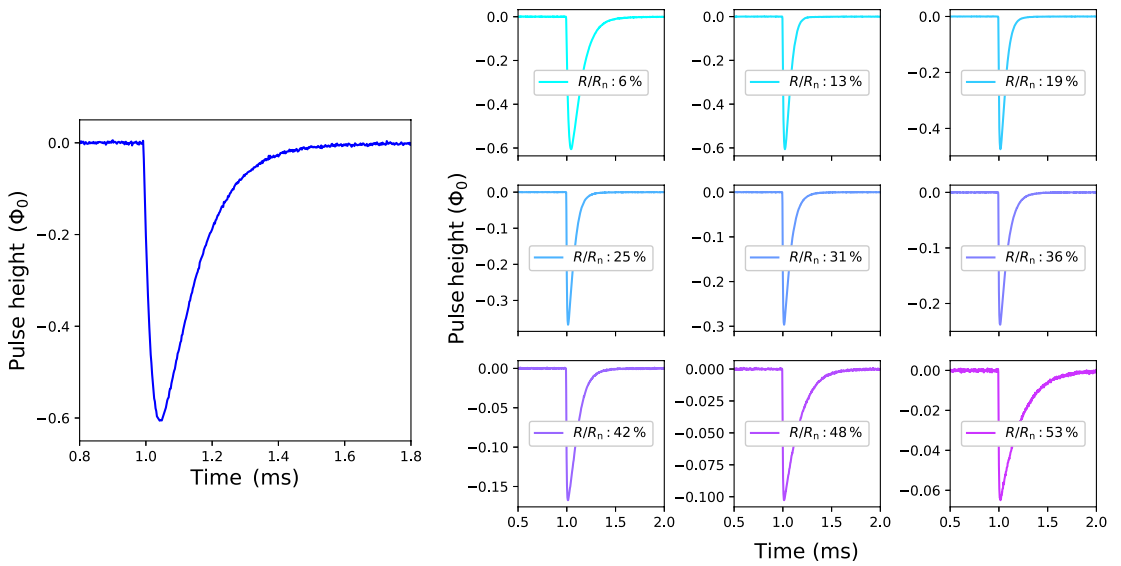


Figure 4.8: (*Left*) A pulse expected from Mn $K\alpha$ for the bias point of 6% of R_n in units of quantum flux (Φ_0). The bias point is defined as the resistance of the TES (R) as a fraction of the normal resistance of the TES (R_n). (*Right*) The average pulses expected from Mn $K\alpha$ for nine different bias points. Their rise and fall time constants were estimated as $\{39, 27, 16, 10, 8, 8, 10, 6, 5\}$ and $\{104, 49, 52, 63, 70, 78, 98, 156, 209\}$ in units of μs , respectively, in order of increasing bias point R/R_n . We note that a model function of $A \exp(-(data - t_d)/\tau_{fall})(1 - \exp(-(data - t_d)/\tau_{rise})) + offset$ was used to extract τ_{rise} and τ_{fall} , where A , t_d , τ_{rise} , τ_{fall} , and $offset$ are the amplitude, trigger time, rise time constant, fall time constant of the pulse, and the baseline offset, respectively [55].

In the following subsections, we present the results on reading out a single pixel with MWMUX01: the 11th channel whose resonance frequency and resonator

bandwidth are 5.287 GHz and 4.7 MHz, respectively. The SQUID was modulated by a 480 kHz flux-ramp with an amplitude of $3\Phi_0$, and the output signal was demodulated using the information for only $1.5\Phi_0$.

We successfully detected X-ray pulses from a single-pixel TES using the MWMUX01 for a range of bias points between 6% of R_n and 53% of R_n , as shown in Fig. 4.8, where R_n is the normal resistance of the TES. We found that this microwave SQUID multiplexer was able to read out a fast signal such as a pulse with $\sim 10\mu\text{s}$ rise time constant.

4.4.3 Result: Noise & Integrated Noise Equivalent Power Resolution

The power spectral densities of the current noise referred to the TES output for a range of bias points between 6 % of R_n and 53 % of R_n are shown in Fig. 4.9 (*Left*). The noise equivalent power (NEP) spectra for nine different bias points are also shown in Fig. 4.9 (*Right*). The NEP was estimated from the ratio of the signal to the noise at each frequency. To investigate the potential detector

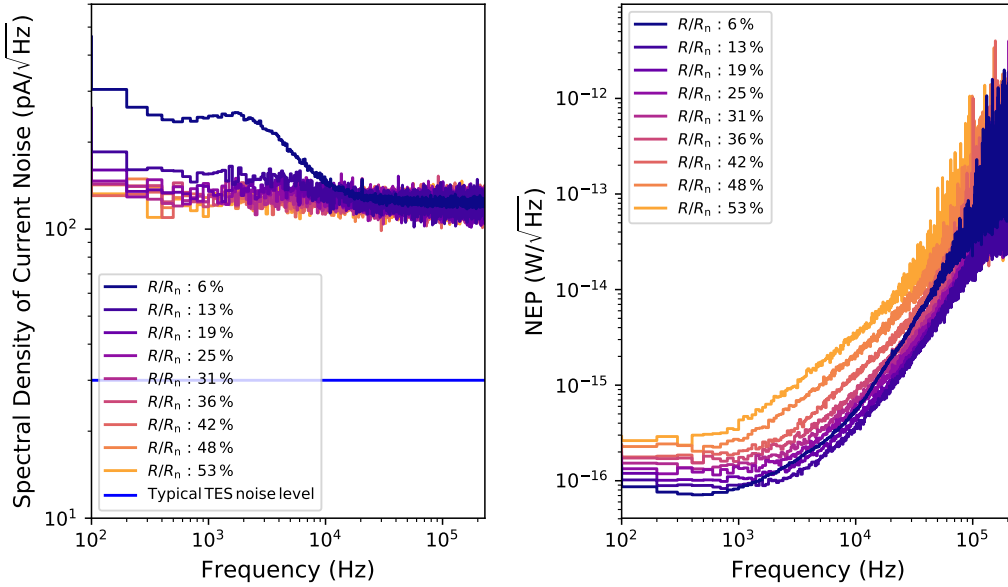


Figure 4.9: (*Left*) the current noise spectral densities for nine different bias points. Blue horizontal line indicates typical sensor noise, $30\text{ pA}/\sqrt{\text{Hz}}$ at typical bias point, 30%. (*Right*) the noise equivalent power (NEP) spectra for nine different bias points.

performance with the microwave SQUID multiplexer, we calculated an integrated NEP resolution, that allows us to determine the achievable energy resolution under given experimental conditions. The integrated NEP across all frequencies as a function of bias point is shown in Fig. 4.10. From the result, we can estimate that the achievable energy resolution is about 10–11 eV at the bias points of 6 and 13 % of R_n .

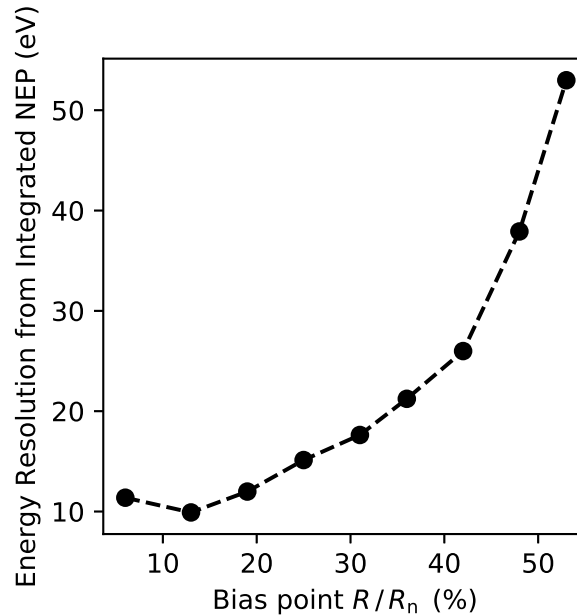


Figure 4.10: The integrated NEP, the achievable energy resolution determined from integrating the NEP across all frequencies, as a function of the bias point [55].

4.4.4 Result: Single-Pixel Performance with MWMUX01

To evaluate the detector performance, we collected 998 X-ray photons from an ^{55}Fe source at the bias point of 6% of R_n , where the integrated NEP FWHM resolution is 11.4 eV. We applied the optimal filter to all pulses and corrected the non-linearity of the response with a quadratic function passing through the zero points, Mn $K\alpha$ (5.9 keV), and Mn $K\beta$ (6.5 keV) lines. We fitted the Mn $K\alpha$ line with Gaussian-convolved Lorentzians by using the maximum likelihood method, and we finally obtained an energy resolution of 11.8 eV FWHM at 5.9 keV, as shown in Fig. 4.11. Moreover, we successfully obtained X-ray pulses with two-

pixel multiplexing, but they did not yield spectroscopic quality energy resolution due to problems with the detectors themselves.

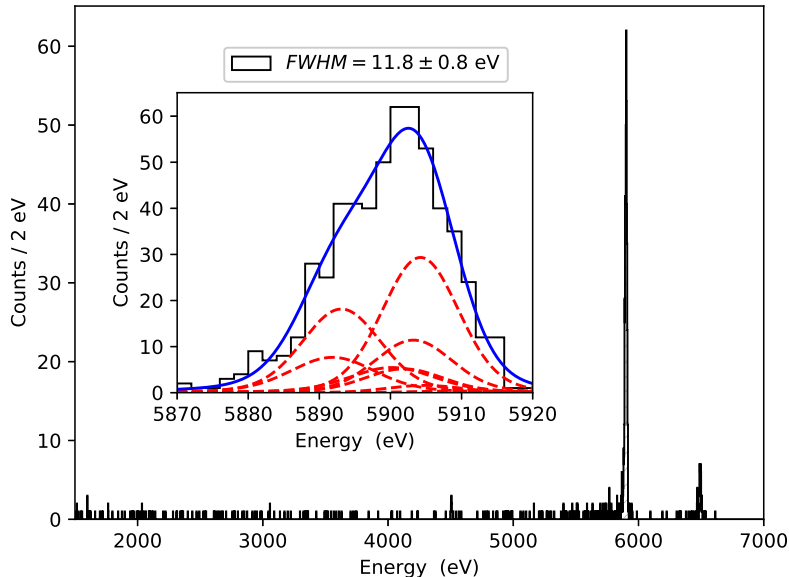


Figure 4.11: The energy spectrum of X-ray photons from an ^{55}Fe source detected by a pixel with MWMUX readout. The inset is a close-up view of the Mn $K\alpha$ line (*black*) along with a Gaussian-convolved multiple-Lorentzian fit with FWHM resolution of 11.8 eV (*blue*). The experimentally determined fine structure shapes are from Hölzer et al. [58] (*red*) [55].

4.4.5 Discussion

With the microwave SQUID multiplexing readout, we obtained an energy resolution of 11.8 eV FWHM at 5.9 keV, and the estimated achievable energy resolution from the ratio of the detector signal to the noise S/N was 11.4 eV at a bias point of 6% of R_n . The experimental noise, the thermal noise of TES, and the readout noise were ~ 250 , ~ 70 , and $\sim 120 \text{ pA}/\sqrt{\text{Hz}}$, respectively. The excess noise was therefore calculated as $> 200 \text{ pA}/\sqrt{\text{Hz}}$ at $R/R_n = 6\%$, though the origin is still under investigation. The evaluated energy resolution seems to be degraded due to large excess noise specific to low bias points such as $R/R_n = 6\%$. As can be seen in Fig. 4.10, the optimum bias points are around $\sim 10\%$ of R_n in the present case. However, the TES developed by ISAS/JAXA is typically biased at $\sim 30\%$ of R_n , where the typical thermal noise and the integrated NEP FWHM

resolution estimated from the frequency-integration of NEP shown in Fig. 4.10 are $\sim 30 \text{ pA}/\sqrt{\text{Hz}}$ and $\sim 4 \text{ eV}$ under the readout noise of $20 \text{ pA}/\sqrt{\text{Hz}}$, respectively [59]. This bias point, however, was not acceptable in the present case, since the worse integrated NEP FWHM resolution of 17.6 eV is expected at the bias point of 31 % of R_n , due to the large readout noise which is roughly a factor of four above the typical sensor noise, $\sim 30 \text{ pA}/\sqrt{\text{Hz}}$. Thus, we should develop a microwave SQUID multiplexer that has a large input coupling of $M_{\text{in}} > 180 \text{ pH}$ which improves S/N by a factor of more than 3, and increase $\Delta f_r/BW$ to ~ 1 which improves S/N by a factor of 2–3. These are achievable by adopting a wider and much longer SQUID ring, resulting in increasing both the SQUID loop inductance and the number of turns of the signal input coil. We discuss these in the following chapter.

4.5 Summary

We developed MWMUX01 for reading out a TES X-ray microcalorimeter by increasing the BW of the resonator. We give the first demonstration that the SQUID-resonator coupling strength can be optimized simply and accurately by varying only the position of the ground-via on the microstrip loop for all channels. With the developed MWMUX01, we successfully detected X-ray photons from a single-pixel TES X-ray microcalorimeter and obtained an energy resolution of 11.8 eV FWHM at 5.9 keV . By investigating the integrated NEP resolution, we conclude that the most significant component degrading the energy resolution is the readout noise which is higher than the detector noise. To overcome this situation, a MWMUX with large mutual inductance between the SQUID and TES circuit should be developed. In the next chapter, we describe the development of MWMUX with large mutual inductance and an investigation of an undesirable resonance that could degrade the SQUID characteristics.

Chapter 5

MWMUX02: Low Current Noise MWMUX

5.1 Objective of Development

In Chapter 4, with MWMUX01, we successfully detected X-ray pulses from a single-pixel TES X-ray microcalorimeter and measured an energy resolution of 11.8 eV at the 5.9 keV Mn-K α line. However, we did not exploit the detector's ability because current readout noise, $120 \text{ pA}/\sqrt{\text{Hz}}$, was four times larger than that of the sensor, $30 \text{ pA}/\sqrt{\text{Hz}}$. In order to reduce the readout-current noise level, $\sqrt{S_I}$, to less than that of the detectors, it is necessary to develop a MWMUX with a large mutual inductance, M_{in} , between the SQUID and the input coil connected to a TES microcalorimeter in series. On the other hand, a large mutual inductance can cause undesirable resonances, which affect SQUID characteristics and degrade SQUID performance significantly, because of the non-negligible length of the input-coil, l_{input} in comparison with the wavelength of an injected microwave. In the case of the DC-SQUID, two main undesirable resonances have been reported, the so-called input-coil resonance and the washer resonance [60, 61, 62, 63]. The former arises when the total length of the multi-turn input-coil on a DC-SQUID ring is equal to a multiple of the half-wavelength of microwaves generated from the voltage-biased Josephson junctions. The latter occurs when the length of the SQUID ring is equal to a multiple of the half-wavelength of the microwaves. These two resonances distort the voltage-flux characteristics and degrade the noise performance of the DC-SQUID. In the same fashion, an RF-SQUID in MWMUX could experience those two resonances, and its performance could be degraded, although the frequency range we use for each channel in MWMUX is very narrow and those undesirable resonances are expected to occur rarely.

In this chapter, we design the MWMUX with the input-coil longer than the

wavelength of the microwave-tones used for activating the MWMUX and verify whether the SQUID characteristics and performance are degraded or not. Furthermore, we develop MWMUX with low current noise.

5.2 Design

In Fig. 5.1, we show the mask-layout design of MWMUX02, which consists of eight-channel resonators directly terminated by each RF-SQUID on the $5 \times 5 \text{ mm}^2$ chip. The basic design of MWMUX01 was retained, but the number of channels was reduced from 16 to 8 because the SQUID with the larger mutual inductance takes up more space on the chip. Here, we briefly describe the design of MWMUX02 for the demonstration of low-current noise MWMUX.

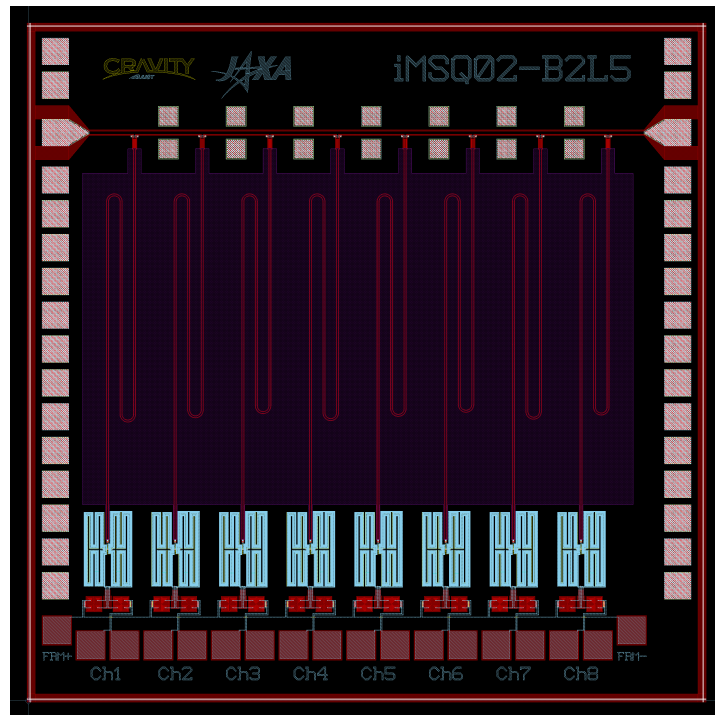


Figure 5.1: The mask design of MWMUX02.

5.2.1 Resonance frequency and BW

The design values of the resonance frequencies and their spacings were from 4.87 to 4.98 GHz and 16 MHz, respectively. The design BW is 2 MHz, which enables the resonators to respond sufficiently to a 500 kHz ramp signal.

5.2.2 SQUID, Input coil and Mutual Inductance

The SQUID forms a parallel two-loop (first-order) gradiometer, which consists of two symmetric microstrip line lobes with a super-insulation-super (Nb/AlO_x/Nb) JJ whose critical current is designed to be 10 μ A. The mutual inductance M_{in} is designed by using the relation of $M_{\text{in}} \approx 2NL_S$ [64], where N is the number of the input-coil turns formed above each SQUID loop. The factor of 2 comes from the number of parallel loops. In order to suppress the readout-current noise to below the typical detector noise, we targeted a M_{in} of 360 pH, which is six times larger than for the MWMUX01. This can be achieved by N of 11 turns and L_S of 16.5 pH, for which λ is 0.5.

Figure 5.2 (a) shows a micrograph of the RF-SQUID, and (b) shows the design drawing of the SQUID on which input and modulation coils are formed. We provided a hole in the ground plane to define the beginning and the end of the input coil. The characteristic impedance of the input coil, Z_1 , on the SQUID ring can be calculated as roughly 30 Ω . On the other hand, that on the hole is approximately ten times higher due to the absence of screening currents below the input wires. Thus, the input coil can be regarded as an open-ended transmission line.

In Fig. 5.2 (c), we show the schematic representation of a SQUID coupled to an input coil through M_{in} . A standing wave with a wavelength of $2l_{\text{input}}/m$ can occur on the input coil, where m is an integer. The input-coil length is 51.44175 mm which corresponds to an input-coil resonance frequency, $f_{\lambda/2}$, of 1.3 GHz. The SQUID-loop length is 4640 μ m, which corresponds to a washer resonance frequency of 14 GHz. Thus, the washer resonance could not occur in this configuration because its resonance frequency is higher than the 4–8 GHz frequencies used in our MWMUX. We note that those resonance frequencies were calculated based on the assumption that the dielectric constant of SiO₂ insulator, and the magnetic penetration depth of Nb were 4, and 39 nm [54], respectively. Figure 5.2 (d) shows the cross-section of one of the SQUID loop on the cut indicated in Fig. 5.2 (b). The coils had a 1.5 μ m width and were wound on the 30 μ m wide Nb SQUID loop with a 2.5 μ m pitch.

5.3 Fabrication

The MWMUC02 chip was also fabricated by the CRAVITY (Clean Room for Analog & digital superconductiVITY) of AIST (National Institute of Advanced Industrial Science and Technology) by using the *caldera planarization* [66, 67]. Irimatsugawa et al. [68] reported that this process improved the Q_i , which was degraded due to the residual metallic film, especially palladium, along the CPW

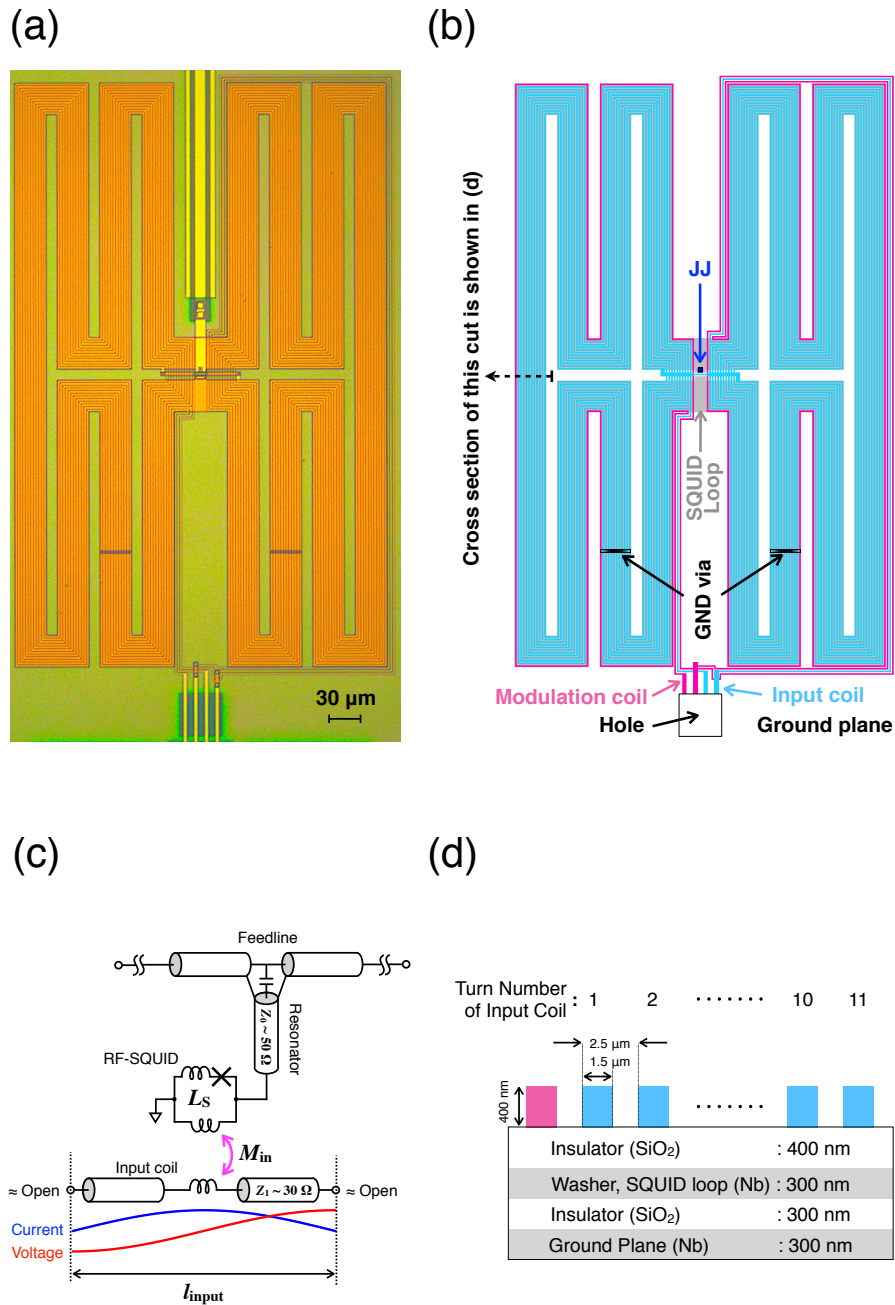


Figure 5.2: (a) Micrograph of a SQUID, which acts as a parallel two-loop (first-order) gradiometer, coupled to an 11-turn input coil on each loop. (b) Design drawing of SQUID, on which input and modulation coils are formed. A hole in the ground-plane yields characteristic-impedance gaps between the input coil on and off the hole. The length of the input coil is defined as the round-trip length of the input coil from and back to the hole. (c) Schematic representation of the SQUID coupled to the input coil. Both ends of the input coil can be regarded as approximately open. Thus, standing waves can be generated on the input coil with the half-wavelength of injected microwave tone. (d) Cross-section of the SQUID loop, with the modulation and the input coils, on the cut indicated in (b) [65].

resonator edge with the conventional fabrication process of MWMUX01, and Q_i values higher than 5×10^4 were obtained.

5.4 Measurement Setup

The MWMUX was attached to a sample holder mounted on a cold head in an adiabatic demagnetization refrigerator (ADR). Note the ADR used in this measurement is a different one than for the measurement of MWMUX03 we mention in the following chapters. The base temperature of the sample holder was cooled down to 100 mK at which our TES X-ray microcalorimeter is usually activated. To confirm resonance shapes and decide probe frequencies, the transmission, S_{21} , across the frequency including all resonances of eight channels was measured using a 1–20 GHz vector network analyzer (VNA). The input microwave was attenuated to about -71 dBm before being launched into the feedline. The transmission signal through the chip was amplified by a high electron mobility transistor amplifier (HEMT) with about 35 dB gain at the 4 K stage, and also by a room-temperature amplifier which gives about 29 dB amplification over the bandwidth of 4–8 GHz, before the signal returned to the VNA. We also measured the flux dependence of resonators by stepwise applying static (DC) injection currents into the modulation line formed on the MWMUX chip. After those experiments, we measured the mutual inductance and noise spectrum of each channel under the condition of applying the flux-ramp modulation (FRM) with a 480 kHz frequency and a $2.5 \Phi_0$ amplitude. The tones ranging from -42.72 to 68.16 MHz around a local-oscillator (LO) frequency of 4.8936 GHz were generated by a field-programmable gate array (FPGA), and up-converted to the microwave ranging from 4.85088 to 4.96176 GHz by being mixed with an LO signal in an in-phase quadrature (IQ) mixer. The transmission signals through the ADR were down-converted and processed in the FPGA. Finally, we obtain a phase angle on the resonance circle, θ , as a function of the input flux threading the SQUID loop. Applying known static injection currents into the input coils coupled to each SQUID, we obtained the periodic responses of θ of the SQUID depending on the injected currents (I - θ characteristic). We extracted the mutual inductances by dividing the flux quantum, Φ_0 , by the current interval corresponding to a single period of the I - θ characteristic. In order to apply the FRM, we made the reference signals for the flux-ramp demodulation for each channel by applying a 480 kHz flux-ramp signal to all SQUIDs. A ramp (or sawtooth) signal sharply drops at a turning point. Thus, the reference signal is distorted somewhat at the turning point. The distorted portion of the reference signal is not available for the demodulation, and we usually discard that. In the noise experiment, by using 60% of the whole reference signal, we demodulated the modulated frequency combs by tracking the phase shifts from the references.

5.5 Results

5.5.1 Resonances and SQUID characteristics

Figure 5.3 (*upper*) shows a VNA sweep of the transmitted power, $|S_{21}|^2$, of the eight-channel MWMUX. In Fig. 5.3 (*middle*), we show the trajectory of the transmitted-power variances at the fifth channel due to the input-flux applied to the SQUID. The resonators were spaced 14–17 MHz apart, and had bandwidths of 1.9–3.0 MHz which were yielded on the internal and coupling quality factors, Q_i and Q_c , of 4900–22000 and 1800–3000, respectively. In Fig. 5.3 (*bottom left*), we present the trajectory of the variances of two-port scattering parameters for transmission, S_{21} , responding to applied flux into the SQUID at a fixed frequency of the fifth resonator. We also show the phase angle on the resonance circle, θ as a function of applied flux into the SQUID loop, namely, the Φ – θ characteristic. The mutual inductances were found to be 372 ± 1 pH from applying known current into the input coils.

In Fig. 5.4 (A), we show a comparison between voltage-flux characteristics affected (*upper*) and not affected (*bottom*) by the input-coil resonance for the DC-SQUID. The input-coil resonance induces current-steps on the current-voltage characteristic and complicated structure on the voltage-flux characteristic as shown in Fig. 5.4 (A) (*upper*), resulting in unstable flux-locked-loop (FLL) operation and increased noise. Figure 5.4 (B) shows Φ – θ characteristics of all eight channels in MWMUX02. From Figs. 5.3 and 5.4 (B), we found that the shape of the $|S_{21}|^2$ – f characteristics, the trajectory of the resonance circle of the present MWMUX, and the Φ – θ characteristics were as smooth as those of the previous one (MWMUX01) and not distorted. This indicates that the SQUID with $f_{\lambda/2} = 1.3$ GHz does not suffer from input-coil resonances in the MWMUX case.

5.5.2 Flux and Current Noise

Figure 5.5 shows the flux- and current-noise spectra of all eight resonators, and their white-noise levels. The white noise in units of flux and current was respectively around $3.2 \mu\Phi_0/\sqrt{\text{Hz}}$ and $18 \text{ pA}/\sqrt{\text{Hz}}$ except for channel 1. The noise performance of channel 1 was degraded to $3.8 \mu\Phi_0/\sqrt{\text{Hz}}$ or $21 \text{ pA}/\sqrt{\text{Hz}}$ due to the lower Q_i than the other channels. The origin of the degradation of Q_i is under investigation, but there is no significant effect on the SQUID operation as the noise level is lower than that of the TES. The obtained current noises were six times better than those of MWMUX01 of $\sim 120 \text{ pA}/\sqrt{\text{Hz}}$ as shown in Fig. 5.6, and these were below the typical TES noise level of $\sim 30 \text{ pA}/\sqrt{\text{Hz}}$.

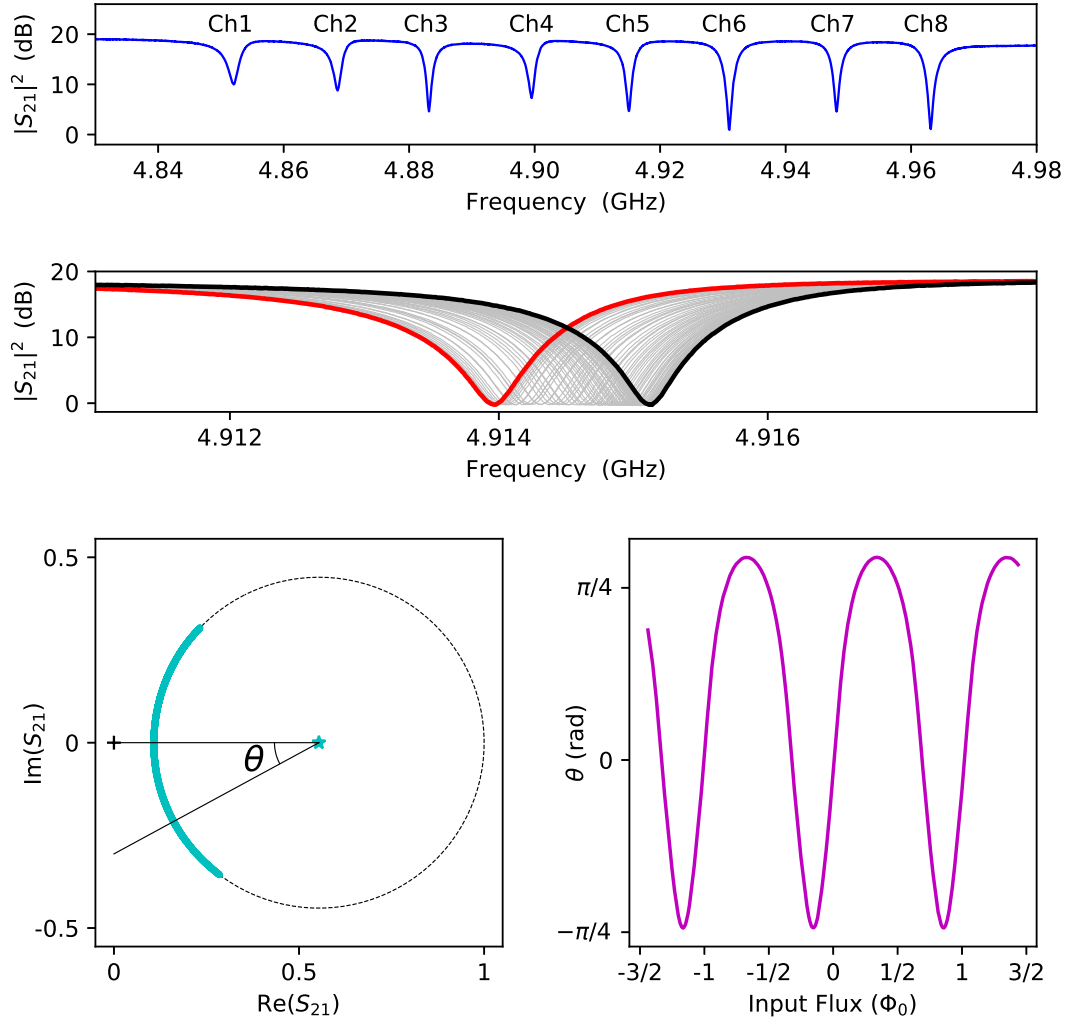


Figure 5.3: (*upper*) Transmitted power as a function of frequency in units of dB. (*middle*) The trajectory of variances of resonance frequencies at the fifth channel due to the input flux applied to the SQUID. (*bottom left*) The trajectory of the transmission coefficient, depending on input flux, on a resonance circle in the complex plane for the same channel. The data (cyan line) agree with a circle (black-dotted line), and the angle on the resonance circle, θ , is defined as the angle between the real axis and a ray passing through the center of the circle and a datum. (*bottom right*) θ of the fifth channel as a function of the input flux. [65].

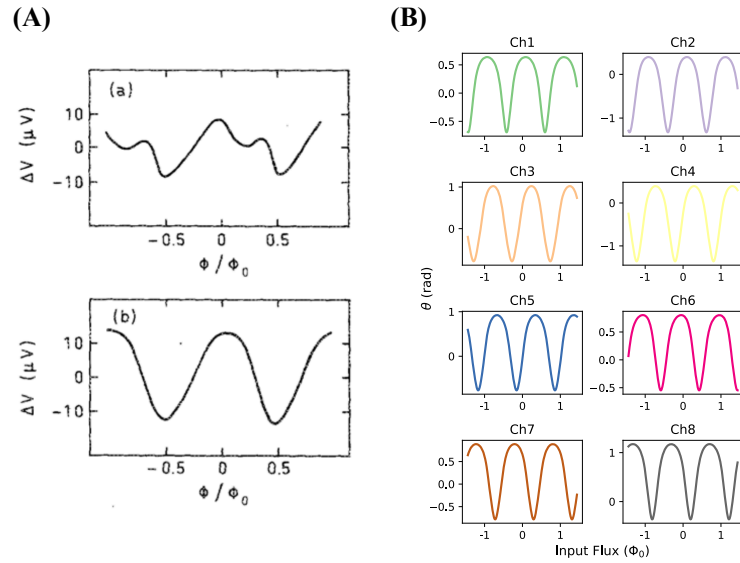


Figure 5.4: (A) Voltage v.s. input flux characteristics of DC-SQUID with (a) and without (b) resonance (Source: Fig. 10 in [69]). (B) θ v.s. input flux characteristics of the RF-SQUID in our MWMUX.

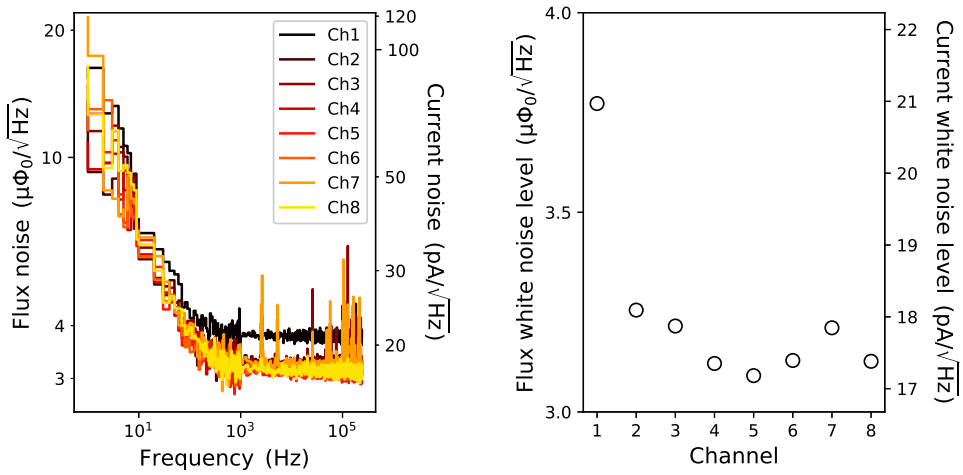


Figure 5.5: (left) Flux and current noise spectra of all eight resonators, in units of the flux quantum and the ampere. The current noise was calculated using the input-SQUID mutual inductances, M_{in} , the value of 372 pH. (right) Flux and current white noise level of each resonator. [65].

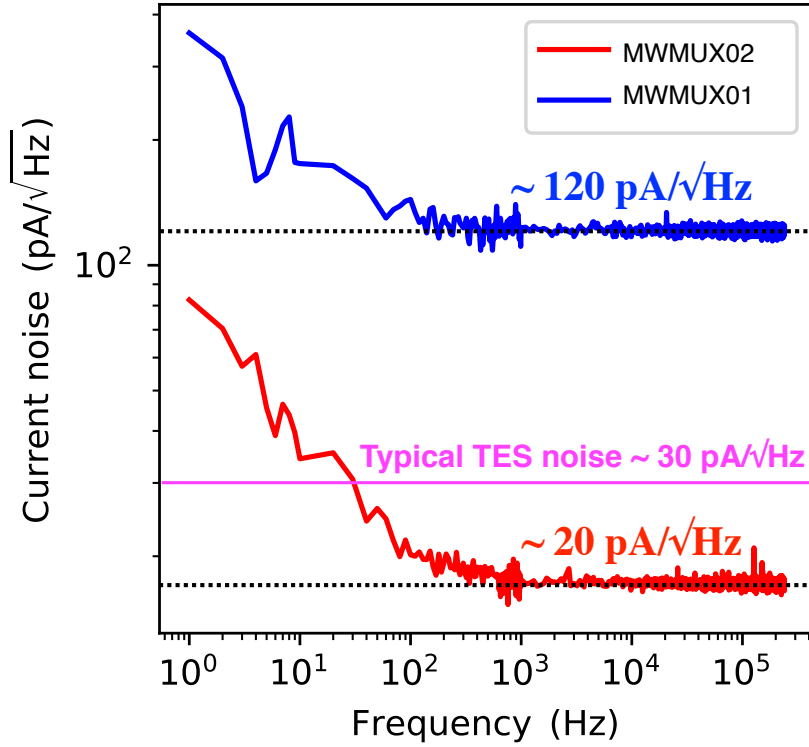


Figure 5.6: Comparison between current-noise spectra of MWMUX01 and MWMUX02 (only one typical channel is shown for each).

5.6 Discussion

In the case of MWMUX, microwaves injected into SQUIDs are monochromatic, and their frequencies are discrete, i.e., localized near the dips of the $|S_{21}|^2-f$ characteristics. Therefore, it is improbable that these discrete frequencies of the microwave tones become equal to $mf_{\lambda/2}$. Moreover, we can prevent $f_{\lambda/2}$ from corresponding with the resonance frequencies of MWMUX by tuning the resonance frequencies in the design. According to the above, we can conclude that MWMUX may not suffer from the so-called input-coil resonance. Our experimental results show that the input-coil length does not determine the upper limit of M_{in} for MWMUX contrary our prediction [70]. In the case of MWMUX based on microstrip RF-SQUID, the slew rate of MWMUX can be considered to determine the maximum M_{in} . Recall from Eq. 3.56, that the slew rate of TES X-ray microcalorimeter using MWMUX with the flux-ramp modulation must meet $(dI_{\text{TES}}/dt) \leq (\Phi_0 f_{\text{ramp}}/2M_{\text{in}})$. Thus, we can derive the restriction of M_{in} to be $M_{\text{in}} \leq \Phi_0 f_{\text{ramp}}/2(dI_{\text{TES}}/dt)$.

5.7 Summary

To suppress the current-referred readout noise, we developed MWMUX02 with a large mutual inductance of 372 pH between the RF-SQUID and input inductor connected to the TES X-ray microcalorimeter in series. We investigated the effect of the so-called input-coil resonance on RF-SQUID for MWMUX. As the results, unlike the case of DC-SQUID, the SQUID Φ - θ characteristics and the readout noise level were not clearly affected by unwanted resonances in our MWMUX. The reason is likely due to the frequency range on each channel we use in MWMUX being very narrow so that input-coil resonances are expected to occur rarely. The obtained result indicates that the upper limit of M_{in} for MWMUX is not determined by the input-coil length, but the restriction of M_{in} can be considered to come from the slew rate of MWMUX. Finally, we successfully developed a MWMUX with a low readout-current noise of $\sim 20 \text{ pA}/\sqrt{\text{Hz}}$, which is below the typical TES noise level. Here, we summarize the designed and measured SQUID properties in Tab. 5.1, comparing the previous SQUIDs (MWMUX01) and the SQUIDs of MWMUX02.

Table 5.1: Summary of SQUID's properties

Parameters	Units	MWMUX02		MWMUX01	
		Des.	Exp.	Des.	Exp.
L_S	pH	16.5	–	6.5	6.2
N	–	11	11	7	7
M_{in}	pH	363	372	91	63
l_{input}	mm	51.44175	–	7.89450	–
$f_{\lambda/2}$	GHz	1.3	–	8.5	–
$\sqrt{S_I}$	pA/ $\sqrt{\text{Hz}}$	–	17–21	–	120

Chapter 6

MWMUX03 and Low-Temperature Components for 80-Pixel TES Readout

6.1 Design

We briefly present a summary of the design of MWMUX03. The design concept is to read out large scale TES pixels using the 4 GHz-full-bandwidth of a HEMT amplifier. We apply a 500 kHz flux-ramp signal to modulate the resonator to take enough samples of a pulse of a TES X-ray microcalorimeter with a rise time of $\sim 10 \mu\text{s}$ so as not to degrade energy resolution. The BW of 2 MHz is compatible with 500 kHz flux-ramp modulation if we apply flux-ramp signal with $2\Phi_0$ amplitude, and 240 resonances can be embedded in 4 GHz if the resonance spacing is 16 MHz. For proper readout operation, to make full use of the SQUID gain, we designed the ratio of $\Delta f_r/BW \sim 1$, where Δf_r is the maximum resonance frequency shift due to the flux applied to the SQUID. The SQUID loop inductance and critical current are respectively designed as 9.88 pH and $10 \mu\text{A}$, and these yield $\lambda = 0.30$. The mutual inductance is designed as 237 pH, and then the slew rate of the MWMUX is 2.1 A/s. Six chips, each embedding 40 resonators and SQUIDs in $5 \times 20 \text{ mm}^2$, will be developed in the future. Those could cover the full band of 4 GHz. For demonstration, we first design two chips with frequency ranges of 4.6589 to 5.2828 GHz and 5.2989 to 5.9228 GHz, respectively. Due to the I/Q-mixer bandwidth of 4.5–9.0 GHz, we avoided the 4.0–4.5 GHz band. In Tab. 6.1, we summarize the design parameters of two MWMUX03 chips with respect to f_r , C_c , a , and D_c . In Figs. 6.1 and 6.2, we show the mask layouts and a micrograph of the SQUID and RF filters. On the chip, neighboring resonances were placed at every eighth space in order to reduce the effect of crosstalk. The

RF filter was aimed at preventing microwaves from flowing into the TES circuit. Also, the cut-off frequency was designed to be about 5 MHz.

Table 6.1: Design parameters of two MWMUX03 chips

Chip1: Ch41 to 80				Chip2: Ch81 to 120			
f_r	C_c	a	D_c	f_r	C_c	a	D_c
(GHz)	(fF)	–	(μm)	(GHz)	(fF)	–	(μm)
4.658917	16.3	0.58	67.85	5.298866	13.2	0.63	54.40
4.674951	16.2	0.58	67.45	5.314839	13.2	0.63	54.10
4.690956	16.1	0.58	67.05	5.330817	13.1	0.63	53.80
4.706916	16.0	0.58	66.70	5.346872	13.1	0.63	53.55
4.722930	16.0	0.58	66.30	5.362863	13.0	0.63	53.25
4.738911	15.9	0.58	65.90	5.378858	12.9	0.63	52.95
4.754913	15.8	0.59	65.55	5.394836	12.9	0.64	52.70
4.770896	15.7	0.59	65.15	5.410817	12.8	0.64	52.45
4.786898	15.6	0.59	64.80	5.426820	12.7	0.64	52.15
4.802950	15.5	0.59	64.40	5.442804	12.7	0.64	51.90
4.818948	15.4	0.59	64.05	5.458808	12.6	0.64	51.60
4.834905	15.4	0.59	63.70	5.474792	12.6	0.64	51.35
4.850894	15.3	0.59	63.35	5.490869	12.5	0.64	51.10
4.866913	15.2	0.60	63.00	5.506849	12.4	0.64	50.85
4.882888	15.1	0.60	62.65	5.522827	12.4	0.64	50.60
4.898893	15.0	0.60	62.30	5.538821	12.3	0.65	50.30
4.914925	15.0	0.60	61.95	5.554790	12.3	0.65	50.05
4.930909	14.9	0.60	61.60	5.570850	12.2	0.65	49.80
4.946921	14.8	0.60	61.25	5.586806	12.2	0.65	49.55
4.962881	14.7	0.60	60.90	5.602854	12.1	0.65	49.30
4.978866	14.7	0.60	60.55	5.618794	12.0	0.65	49.05
4.994858	14.6	0.61	60.25	5.634825	12.0	0.65	48.80
5.010891	14.5	0.61	59.90	5.650826	11.9	0.65	48.60
5.026867	14.4	0.61	59.55	5.666838	11.9	0.65	48.35
5.042928	14.4	0.61	59.25	5.682839	11.8	0.65	48.10
5.058849	14.3	0.61	58.95	5.698827	11.8	0.66	47.85
5.074889	14.2	0.61	58.60	5.714803	11.7	0.66	47.60
5.090849	14.1	0.61	58.30	5.730845	11.7	0.66	47.40
5.106845	14.1	0.61	57.95	5.746793	11.6	0.66	47.15
5.122923	14.0	0.62	57.65	5.762829	11.6	0.66	46.90
5.138853	13.9	0.62	57.35	5.778826	11.5	0.66	46.70

Continued on next page

Chip1: Ch41 to 80				Chip2: Ch81 to 120			
f_r (GHz)	C_c (fF)	a –	D_c (μm)	f_r (GHz)	C_c (fF)	a –	D_c (μm)
5.154883	13.9	0.62	57.05	5.794829	11.5	0.66	46.45
5.170843	13.8	0.62	56.75	5.810791	11.4	0.66	46.25
5.186902	13.7	0.62	56.45	5.826756	11.3	0.66	46.00
5.202890	13.6	0.62	56.15	5.842787	11.3	0.66	45.80
5.218892	13.6	0.62	55.85	5.858821	11.2	0.66	45.55
5.234905	13.5	0.62	55.55	5.874810	11.2	0.67	45.35
5.250842	13.4	0.63	55.25	5.890801	11.1	0.67	45.10
5.266876	13.4	0.63	54.95	5.906745	11.1	0.67	44.90
5.282832	13.3	0.63	54.65	5.922775	11.0	0.67	44.70

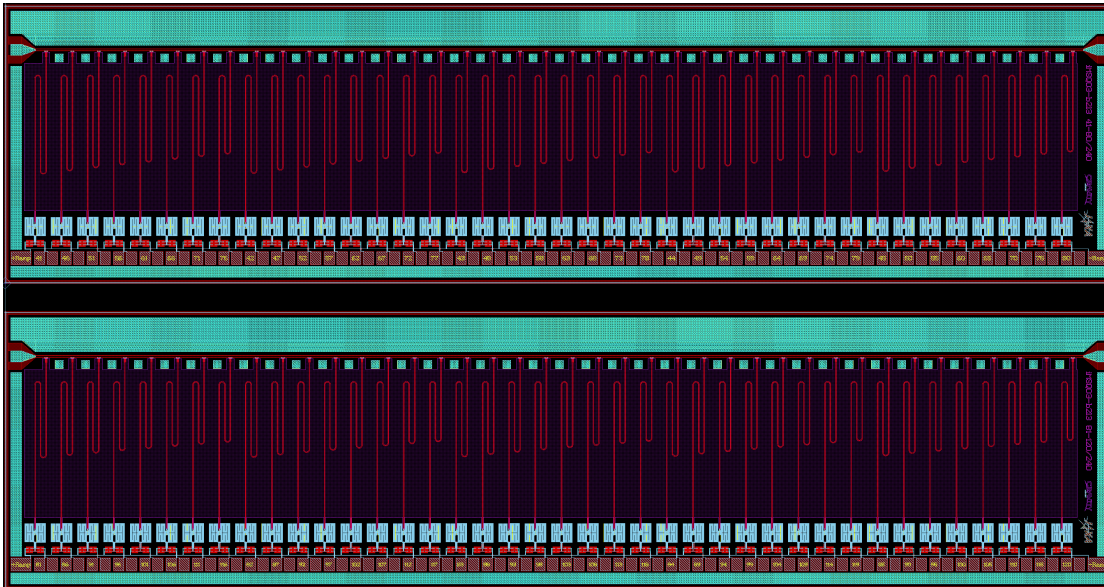


Figure 6.1: Mask designs of two 40-channel MWMUX chips. Neighboring resonators were placed at every eighth space, i.e., the resonators were arranged as follows: Ch41, 46, 51, 56, 61, 66, 71, 76, 82, and so on.

6.2 Fabrication

The MWMUX03 chips were fabricated in precisely the same fashion as the MWMUX02 chips (for detail, see Sec. 5.3).

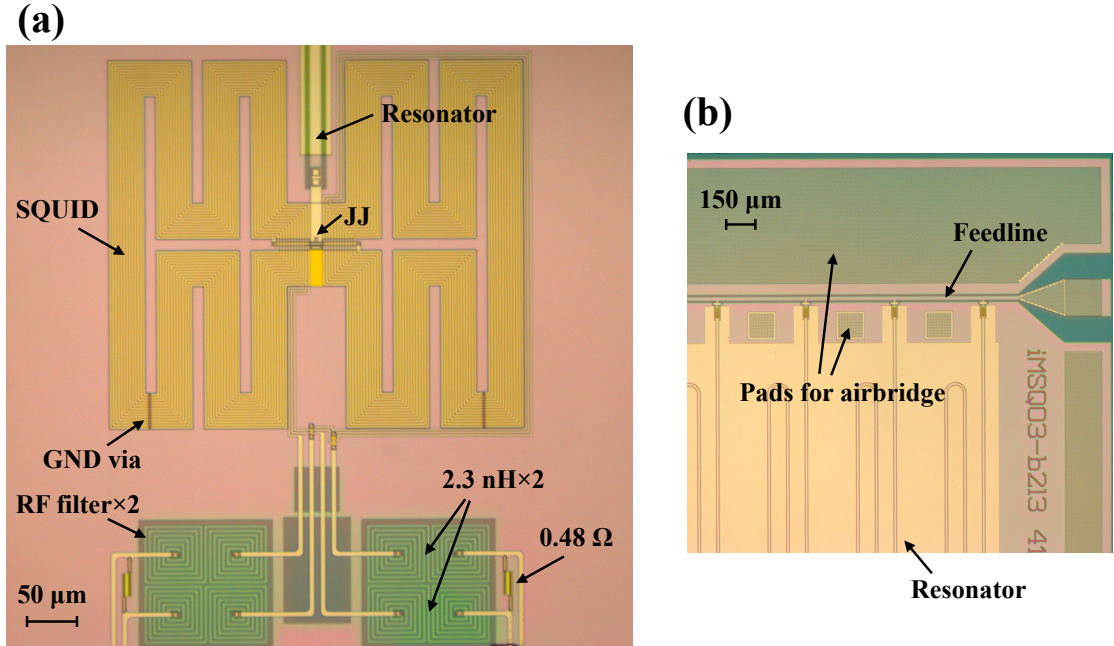


Figure 6.2: (a) Micrograph of a SQUID and an RF filter. (b) Micrograph of pads on the ground plane of the CPW for airbridges.

6.3 Performance Evaluation

6.3.1 Results

The obtained results at the base temperature of 100 mK are described here. In Fig. 6.3, we show the resonances and their spacing. We verified all 40 resonances were yielded. The spacing was ~ 12 MHz, and each chunk of 5 resonances was spaced by roughly 30 MHz. Figure 6.4 shows the maximum resonance frequency shifts Δf_r and bandwidth BW . The bandwidth of the resonators was distributed around the design value of 2 MHz. Although some of them were slightly narrower than the design, these were not expected to affect the 500 kHz FRM readout. The maximum resonance frequency shifts were also roughly twice as small as the design value of 2 MHz. That meant we could not make full use of the SQUID gain, but the operation is not significantly affected. We show the quality factors in Fig. 6.5. The internal quality factors Q_i vary between 22,000 and 110,000, and the coupling quality factors Q_c vary between 1,800 and 4,900. The flux and current noise spectra and the histogram of their white-noise level are respectively shown in Figs. 6.6 and 6.7. The quite large $1/f$ noise at low frequency probably mainly originated from two-level system noise (TLS) [71]. On the other hand, the

obtained flux and current white noise levels were quite good, and those values were $\sim 0.9 \mu\Phi_0/\sqrt{\text{Hz}}$ and $\sim 9 \text{ pA}/\sqrt{\text{Hz}}$, respectively.

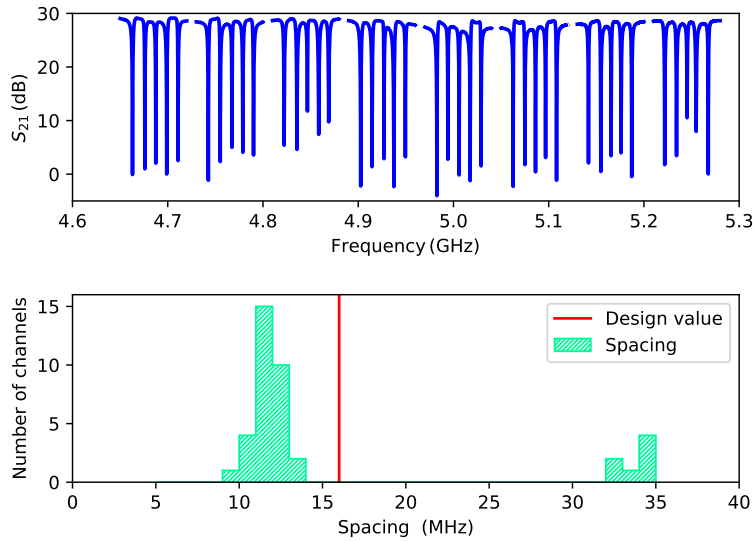


Figure 6.3: Resonances (*top*) and spacing of those (*bottom*).

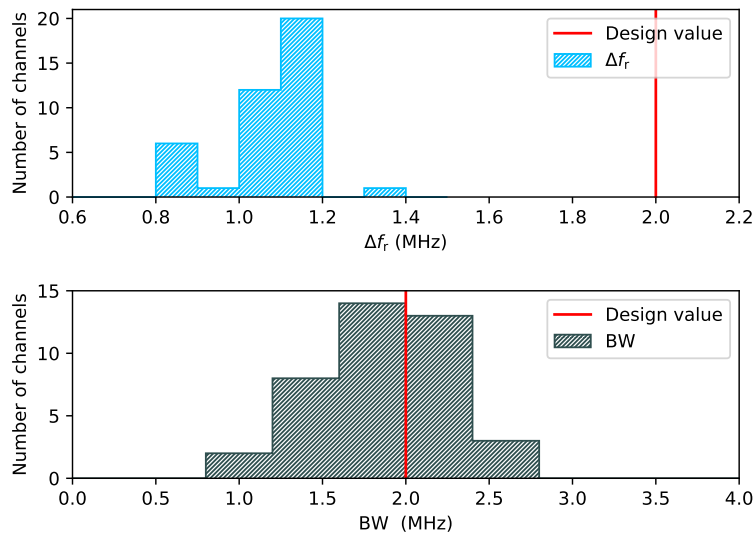


Figure 6.4: Maximum resonance frequency shifts (*top*) and bandwidth (*bottom*).

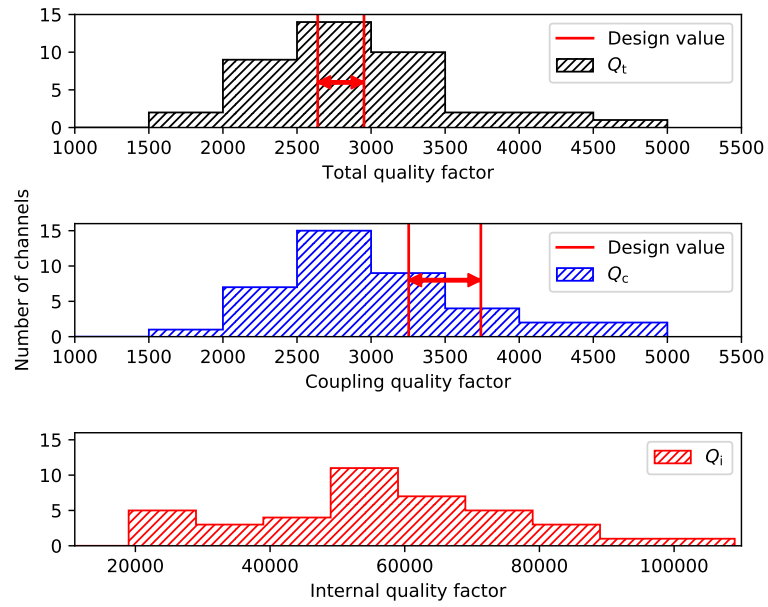


Figure 6.5: Quality factors.

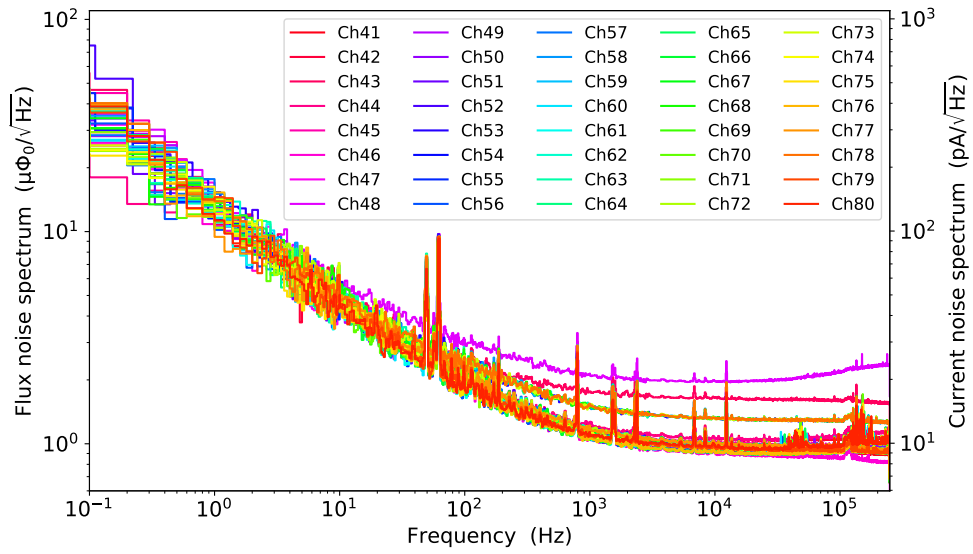


Figure 6.6: Noise spectra.

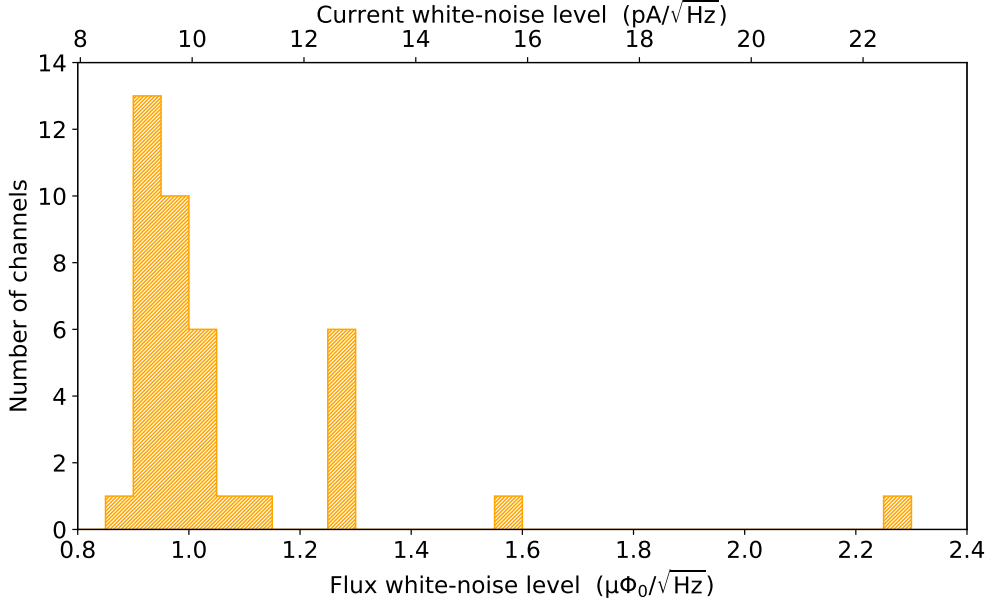


Figure 6.7: Histogram of the white-noise level extracted from Fig. 6.6.

6.3.2 Importance of Airbridge to Avoid Undesirable Resonances

We also studied the effect of airbridges bonded across the center conductor of a coplanar feedline that connects the ground electrodes on both sides. Undesirable resonances caused by an odd propagation mode, e.g., slot mode, can distort MWMUX resonances if the chip size is not negligible compared to the wavelength. Those resonances have never appeared on the previous $5 \times 5 \text{ mm}^2$ chips. However, since the size of $5 \times 20 \text{ mm}^2$ is as large as the wavelength, we need to investigate the effect. We studied the effect of the existence of airbridges with a GM refrigerator, which provides a temperature of 4 K. In Fig. 6.8 (*left*), without airbridge, there is a parasitic resonance in the middle of the MWMUX resonances. On the other hand, in Fig. 6.8 (*right*), the airbridge works well and makes S_{21} flat over the full 4–8 GHz band of the HEMT. This result shows the importance of the airbridge for avoiding a parasitic resonance in such a large chip with a size of $5 \times 20 \text{ mm}^2$.

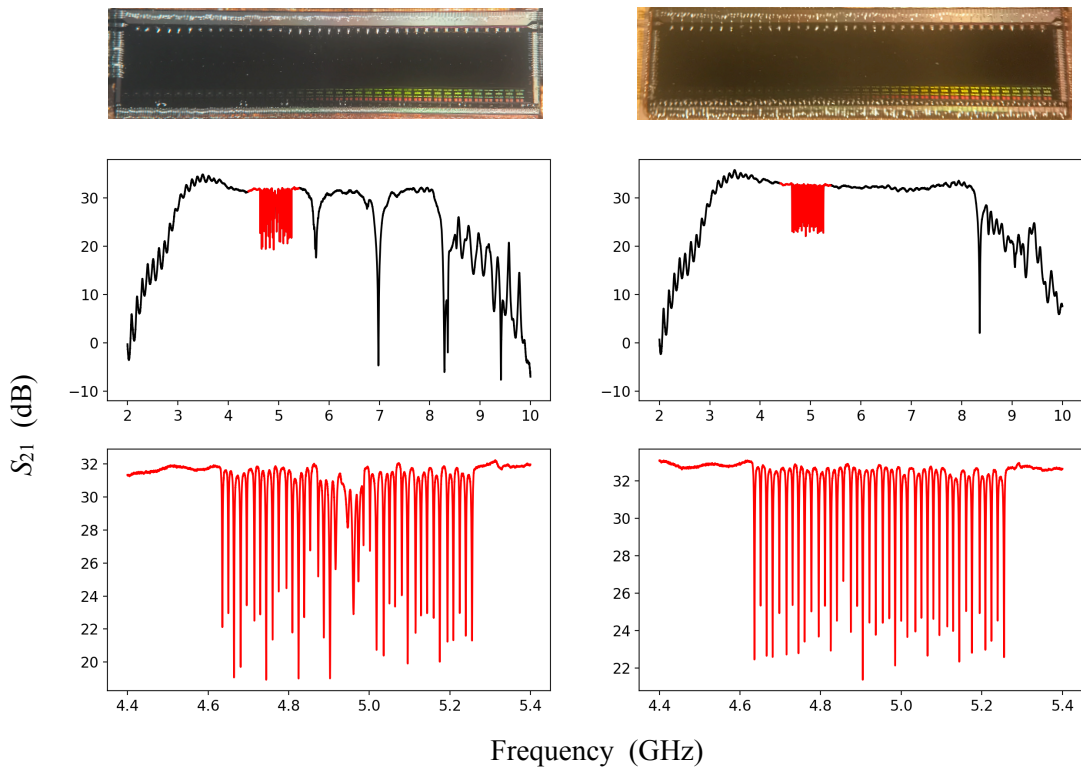


Figure 6.8: The micrographs (*top*) of a 40-channel MWMUX and its transmitted powers (*center*) and those enlarged views (*bottom*) with/without the bonding wire airbridge striding the feedline. Undesirable resonances caused by any odd propagation mode of the CPW, e.g., slot mode, can distort MWMUX resonances (*left*). The airbridges connecting ground planes work well and make S_{21} flat over the whole 4–8 GHz band corresponding to that of HEMT (*right*).

6.4 Development of a 40-Channel Bias Chip for Activating TES Microcalorimeters

A shunt resistance and damping inductor are needed to activate the TES. We also designed a bias chip that includes a value-selectable shunt and inductor. The shunt resistance can be selected from the values 2, 4, 10, 20 m Ω ; on the other hand, the inductance can be chosen from the values 0, 190, 230, 450, 850 nH, respectively. The design of the chip is shown in Fig. 6.10.



Figure 6.9: Mask design of the bias chip, which includes selectable shunt resistances (2, 4, 10, 20 m Ω) and inductors (0, 190, 230, 450, 850 nH) for each of the 40 channels, for activating the TES microcalorimeters. The chip size is 5 \times 20 mm².

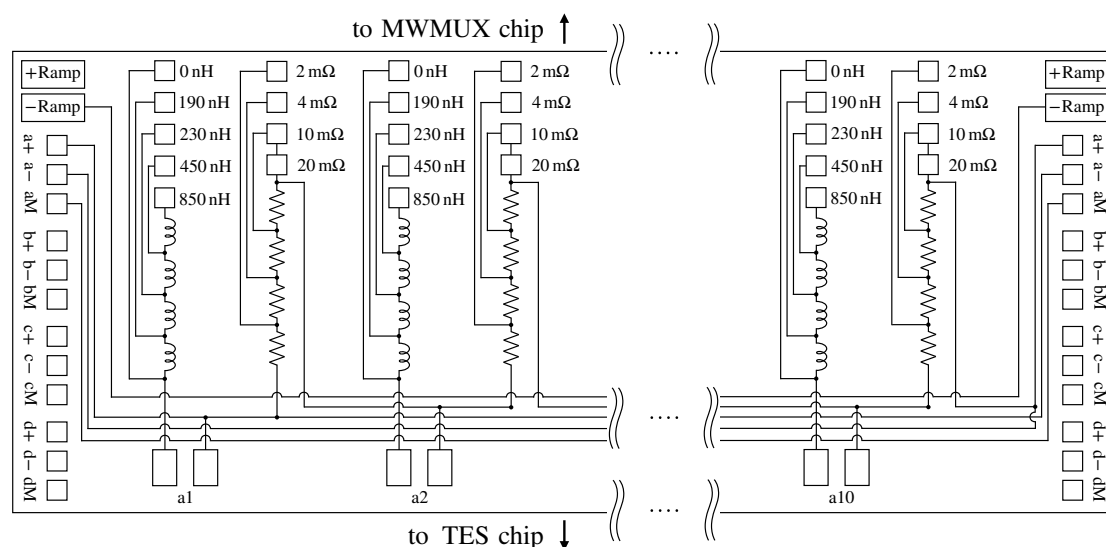


Figure 6.10: Circuit schematic of the bias chip shown in Fig. 6.9. There are 40 channels on the chip, and they are split up into four groups, namely group “a”, “b”, “c”, and “d”, each containing ten channels. Due to space limitations, only wires in group “a” are shown in the figure, but the other groups “b”, “c”, and “d” are also wired on the actual chip. All ten channels in each group are electrically connected in series; hence up to ten TES microcalorimeters can be simultaneously biased with a current source connected to a pair of bonding pads, e.g., a+ and a-.

6.5 Summary

We developed a MWMUX chip with 40 channels in 5 \times 20 mm². All 40 resonances were yielded, and the performance was compatible with reading out TES X-ray

microcalorimeters. The noise level was quite good and we obtained $\sim 9 \text{ pA}/\sqrt{\text{Hz}}$. Also, we investigated the effect of an airbridge bonded across the center conductor of a coplanar feedline that connects the ground electrodes on both its sides. As a result, the airbridge works well and makes the baseline of the resonances flat over the whole 4–8 GHz band. In Tab. 6.2, we summarize the designed and evaluated values. We have achieved the targets A, B, and C set in this theses.

Table 6.2: Design targets and measurement results of developed MWMUX

Parameters	BW (MHz)	Δf_r (MHz)	M_{in} (pH)	Noise ($\text{pA}/\sqrt{\text{Hz}}$)	Channels
Design	2	2	237	<30	40
Results	1.1–2.7	0.8–1.3	208–212	8.5–22.4	40

Chapter 7

Measurement Setup for Readout of TES X-ray Microcalorimeters with 38ch MUX

7.1 Measurement System

In Fig. 7.1, we show an overview of our measurement system. The whole system consists mainly of a refrigerator, to cool the MWMUX and TES down below 100 mK, and microwave readout systems.

For the refrigerator, we use an adiabatic demagnetization refrigerator (ADR) based on a pulse-tube refrigerator (PT) to reach a temperature below 100 mK. Figure 7.2 shows the AIST ADR system and its typical temperature-fluctuation spectrum at 60 mK, where we usually measure TESs. This system provides about 5–6 μK_{rms} temperature stability when we regulate the temperature at 60 mK. The refrigerator contains 4 K, 0.5 K, and cryogenic (50 mK) stages. The PT precools the cryogenic, 0.5 K and 4 K stages to around 2.6 K, and then the ADR with paramagnetic salts of GGG (gadolinium gallium garnet) and FAA (ferric ammonium alum) cools the cryogenic stage to a base temperature of 50 mK. At the 4 K stage, the isolator and 20 dB attenuators are placed. The HEMT provides about 39 dB gain and 2.3 K noise temperature and generates about 12 mW dissipation, and the isolator excludes 4 K thermal radiation, which is a potential noise source. We reduce the noise temperature with 20 dB attenuators in the microwave and flux-ramp signal lines. The microwave components, DC blocks, 10 dB attenuator, and isolator, are placed at the 0.5 K stage. The DC block separates each stage electrically and thermally and reduces the heat load from high-temperature to low-temperature stages. The 10 dB attenuator and isolator reduce the noise temperature. We place the sample holder with the MWMUX and

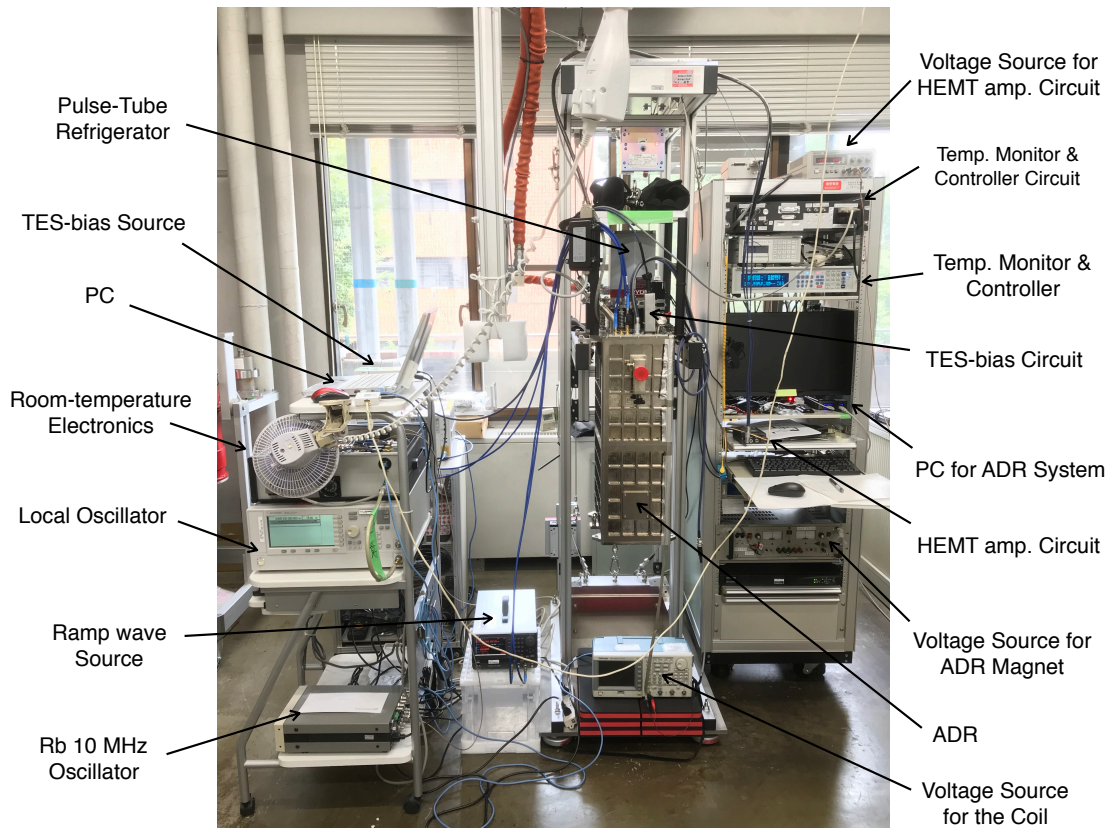


Figure 7.1: Overview of the measurement system.

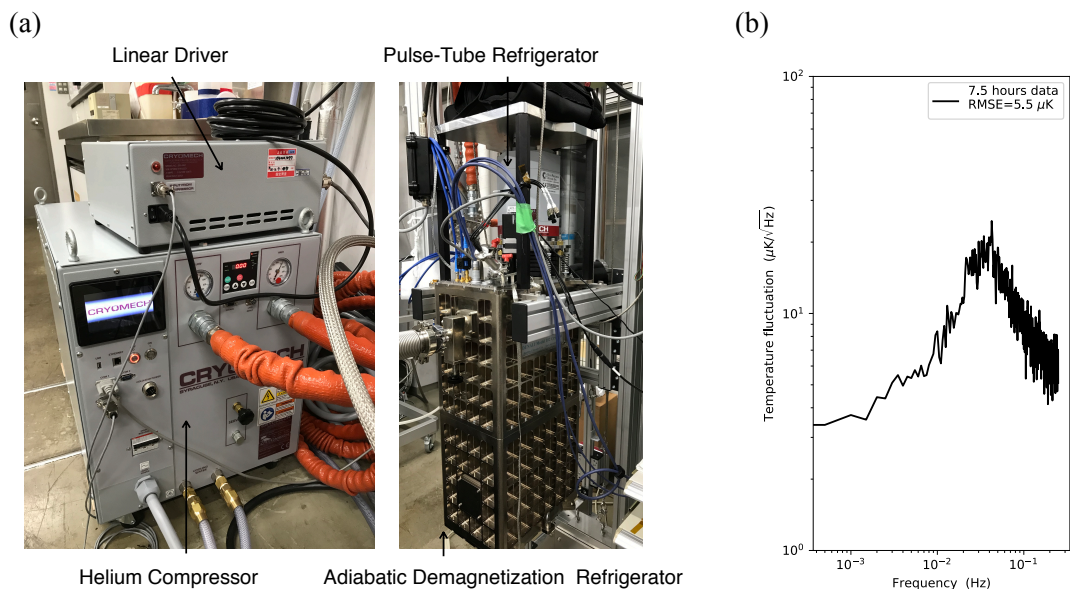


Figure 7.2: (a) AIST adiabatic demagnetization refrigerator (ADR) system. (b) Typical spectrum of temperature fluctuation at 60 mK regulation.

TES chips at the 50 mK stage. NbTi coaxial cables for microwave and 12-pair loom wires are used to connect the 0.5 K and/or 4 K stages to the 50 mK stage in order to reduce the heat load.

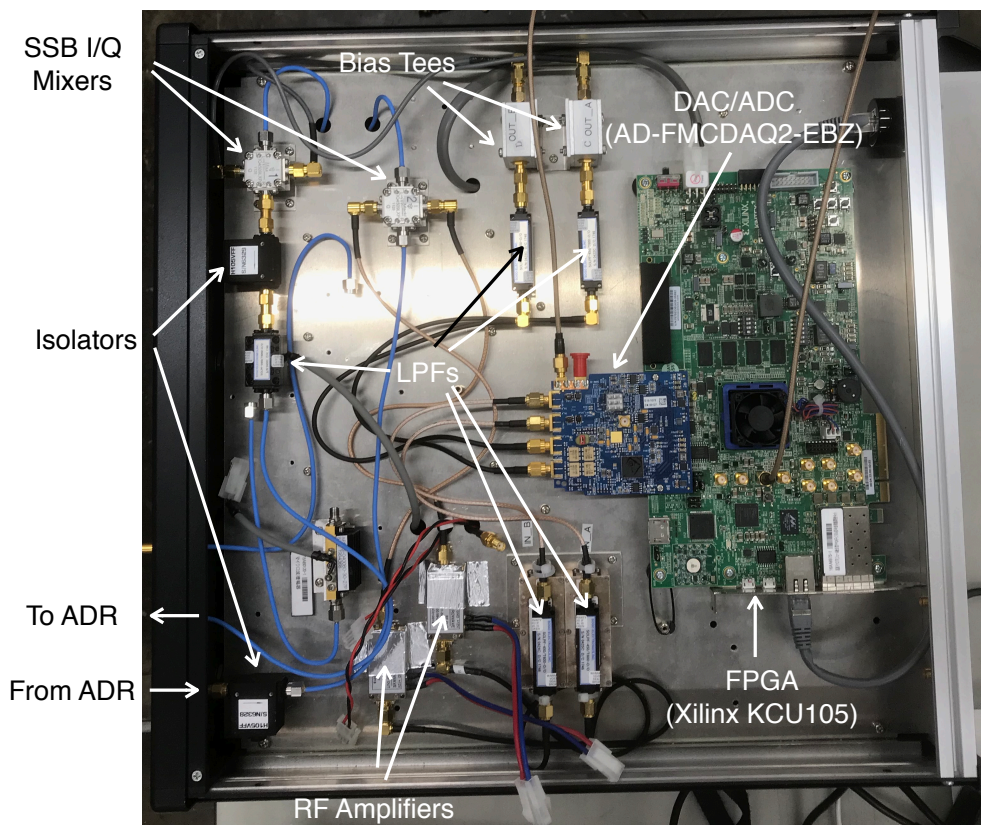


Figure 7.3: Photo of the room-temperature electronics.

A photograph of the room-temperature electronics and the circuit diagram of its system are shown in Figs. 7.3 and 7.4, respectively. The electronics-processing headquarters consisting of FPGA (Field Programmable Gate Array), and 14-bit ADC/DAC (Analog-Digital/Digital-Analog Converter) generates frequency combs in a ± 400 MHz range. The combs are mixed with a carrier wave from a local oscillator (LO) by an In-phase/Quadrature (I/Q) mixer, and up-converted to the frequency range of 4–8 GHz. In order to reduce the thermal noise, the up-converted frequency combs are attenuated by 20 and 10 dB attenuators and launched into the feedline of the MWMUX. The flux-ramp modulated output signals from the MWMUX are amplified by a 4–8 GHz bandwidth HEMT at the 4 K stage and come to the outside of the ADR. After being down-converted at the I/Q mixer and boosted by RF amplifiers with 30 dB gain at room-temperature, the flux-ramp

7.3. TES MICROCALORIMETER: SRON KILO-PIXEL UNIFORM ARRAY71

the voltage source at room temperature is 426Ω . We have not calibrated the coil, i.e., we do not know the absolute values of the magnetic field generated by the coil. Thus, we use the voltage values when we refer to the magnetic field applied by the coil below. When mounting the sample holder, we use a Cryophy magnetic shield to shield the entire cryogenic stage from the external magnetic field.

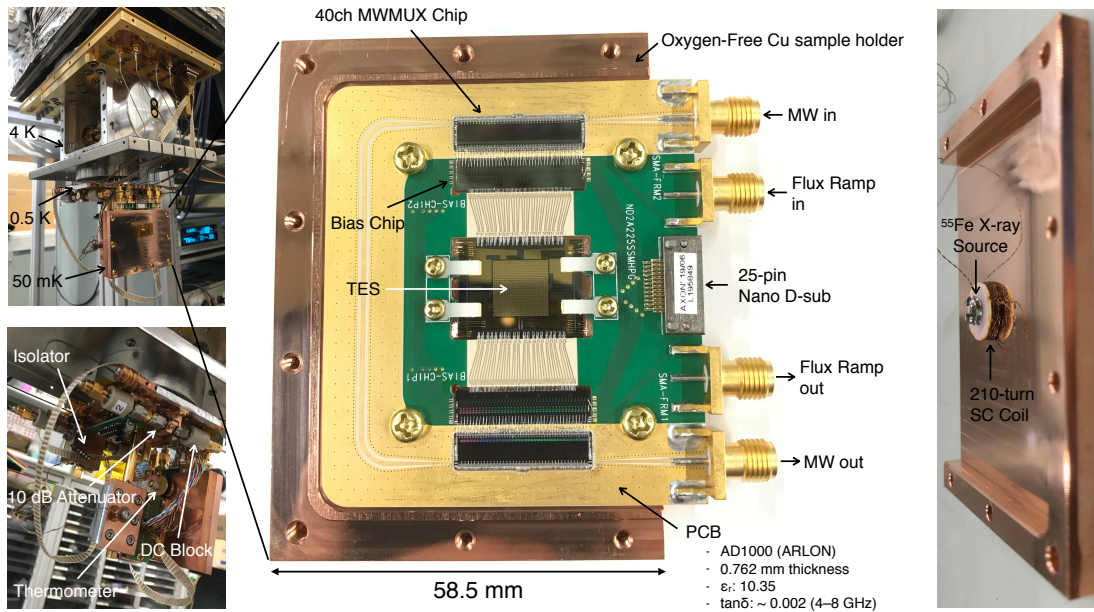


Figure 7.5: Low-temperature setup and microwave components at the cryogenic stage of the ADR.

7.3 TES Microcalorimeter: SRON Kilo-pixel Uniform Array

For the TES X-ray microcalorimeter to evaluate the performance of our developed MWMUX readout system, we use a 32×32 Ti/Au bilayer TES array detector chip developed for the X-IFU instrument on the *Athena* X-ray observatory at SRON [72, 73] (Fig. 7.6). Only 256 out of 1024 pixels are connected to wire-bonding pads. The chip size is $15 \times 19 \text{ mm}^2$. The TESs have a high aspect-ratio dimension of $120 \times 40 \mu\text{m}^2$, and the absorbers consist only of Au with $2.3 \mu\text{m}$ thickness and $240 \times 240 \mu\text{m}^2$ size. The nominal transition temperature and normal resistance are around 110 mK, and $100 \text{ m}\Omega$, respectively.

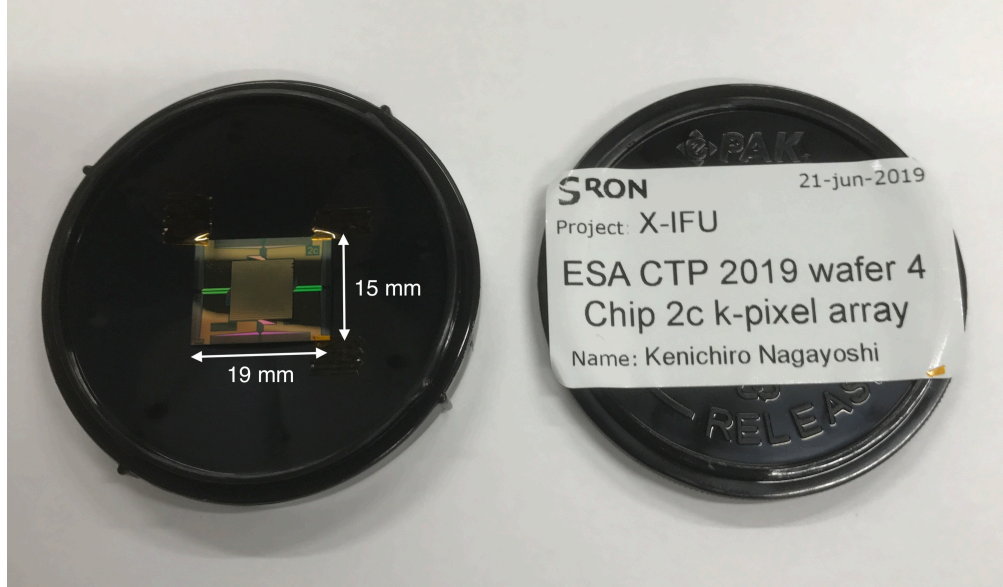


Figure 7.6: A 1024-pixel (32×32 pixels) Ti/Au TES X-ray microcalorimeter array developed by SRON as a backup option for the X-IFU instrument on the *Athena* X-ray observatory to be launched in the early 2030s. Note that only 256 out of 1024 pixels are wired to the bonding pads due to the physical space of the chip. The chip size is $15 \times 19 \text{ mm}^2$.

7.4 MWMUX Setup

We use two 40 ch MWMUX chips whose channel numbers are designated 41 to 80 ch and 81 to 120 ch, respectively. The TES array pixel maps are shown in Fig. 7.7; the left and right indicate the TES pixel and MWMUX channel numbers. In this experiment, we evaluate the TES pixels connected to the MWMUX with channel numbers from 41 to 80 ch.

For the preparation of the TES readout measurement, we generate 40 frequency combs with appropriate power and frequencies and prepare the references of flux-ramp demodulation signals by the following procedure. First of all, we measure the VNA sweep of the MWMUX (Fig. 7.8) and resonance frequency shifts (Δf_r), due to half a flux quantum applied to a SQUID, of all 40 resonances by applying DC flux to the SQUIDS via the FRM line. From the result, we choose the 40 comb frequencies as the center frequencies of the frequency shifts and generate combs injected into the ADR by the room-temperature electronics, as we described above. Next, we take I/Q data by again applying DC flux to the SQUIDS via the FRM line to seek the centers and amplitudes of the I/Q circles (Fig. 7.9). We extract

the phases θ from the I/Q data circles, and we regard these phases as the SQUID responses. Finally, we make the references of the flux-ramp demodulation signals (Fig. 7.10) by applying the flux-ramp signal to all SQUIDs without TES signal inputs. Utilizing the information of the references corresponding to the ramp amplitude of $\sim 1.7\Phi_0$ out of the total of $\sim 2\Phi_0$, we demodulate the modulated frequency combs by tracking the phase shifts from the references.

We optimize the injection power per comb by measuring the noise spectra of the MWMUX. The junction has an optimum bias power due to its critical current. Figure 7.11 shows the white noise levels with respect to comb power per comb injected into the ADR. This result indicates that the optimum power per comb is around -37 dBm, and we use microwave combs with -37 dBm throughout the measurement. The power injected into the ADR is attenuated by 34.5 dB before launching along the feedline of the MWMUX. The attenuation of 4.5 dB and 30 dB out of 34.5 dB come from the cryostat cable loss and 10 and 20 dB attenuators. Thus, the microwave with -71.5 dBm/comb is finally launched along the feedline of MWMUX.

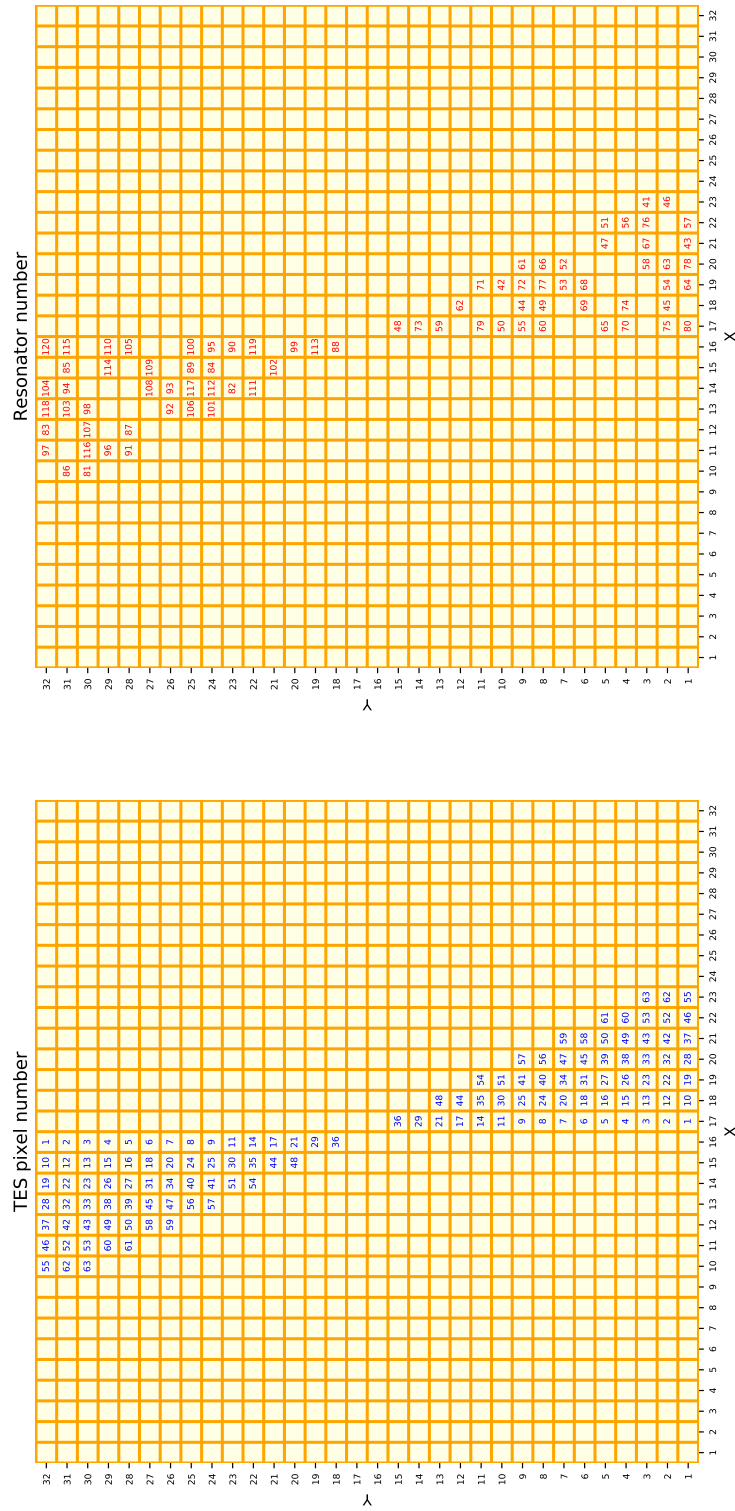


Figure 7.7: The pixel map of the TES X-ray microcalorimeter array mounted on the cryogenic stage. The number on each pixel is the identification number of the TES (*left*) and the MWMUX resonator channel (*right*).

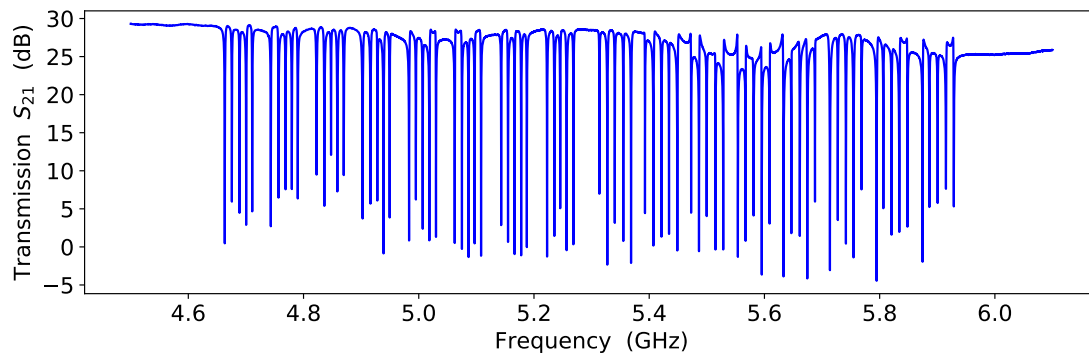


Figure 7.8: Transmission $|S_{21}|$ of all 80ch resonances as a function of frequency.

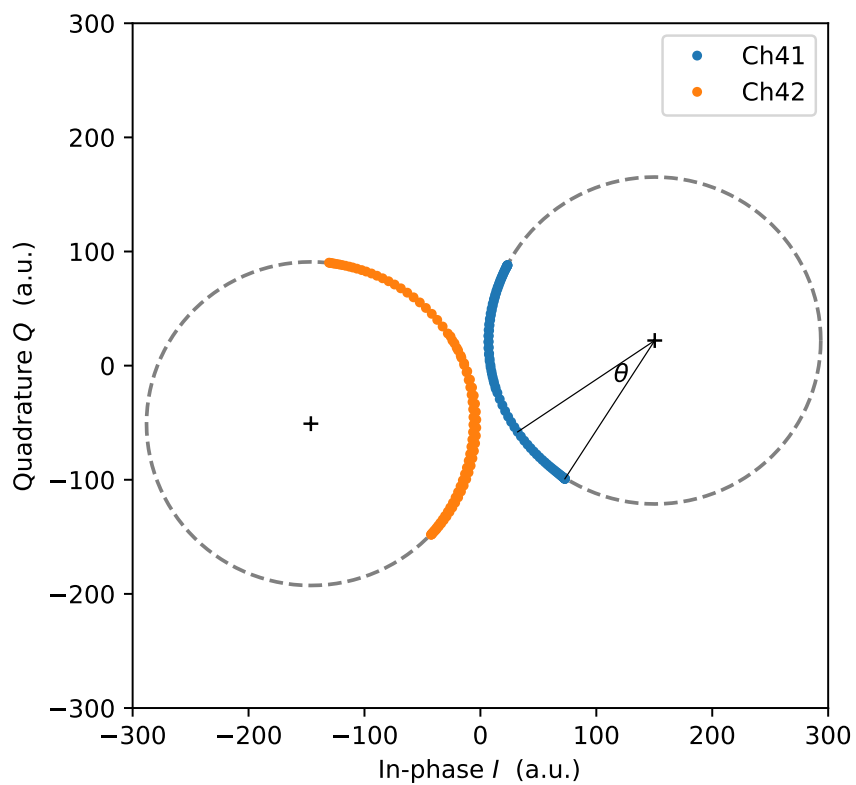


Figure 7.9: The SQUID response in the I/Q plane with respect to DC signals from the FRM line (only Ch41 and 42 are shown).

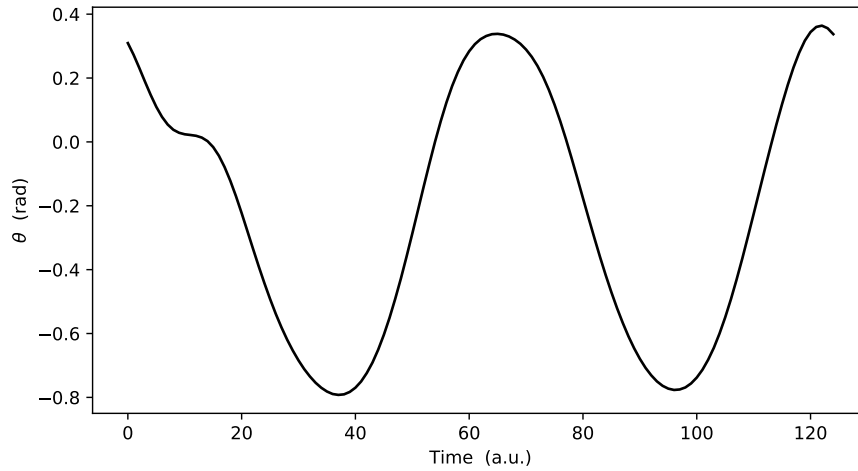


Figure 7.10: An averaged SQUID response θ for a 500 kHz flux-ramp wave (only Ch41). θ is the phase of the I/Q circle, and defined in Fig. 7.9. The horizontal axis is the number of data points with $2 \mu\text{s}$ interval. To demodulate the flux-ramp modulated signal, we use 105 out of 125 (84%) data points.

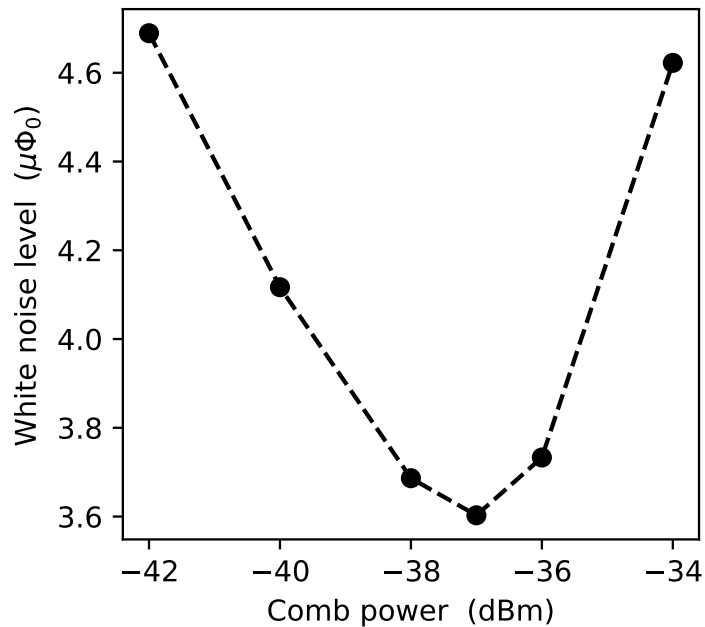


Figure 7.11: White noise levels with respect to comb power per comb injected into the ADR (only one channel is shown). Note that the power is attenuated by about 34.5 dBm from the value before launching along the feedline on the MWMUX.

Chapter 8

Readout of TES X-ray Microcalorimeters with 38ch MUX

We measured 38 TESs out of the SRON 1024-pixel array with the developed 40ch MWMUX. A TES is sensitive to a magnetic field, and the performance can be affected due to the critical current of TES being degraded by the field. In general, the magnetic field remnant at the detector stage is canceled out by applying an external magnetic field onto the TES surface actively. We used a superconducting coil to cancel out the residual magnetic field, which we expected to be generated by the ^{55}Fe X-ray source above the detector. The pulses were collected, and the energy resolutions were assessed by applying the optimal filtering processing and some corrections. Here, we describe the results of the TES readout experiment with our developed 40ch MWMUX.

8.1 Optimization of Magnetic Field

8.1.1 IV Characteristic on Magnetic Field

The TES performance is degraded by the residual magnetic field [74] due to the transition slope dR/dT being reduced or TES gain being suppressed. Therefore we actively applied a field generated by the coil to cancel it out. According to a preliminary experiment, the source of the residual magnetic field was considered to be the ^{55}Fe X-ray source above the detector. To evaluate the residual magnetic fields on each TES pixel, we first measured TES current-voltage (IV) characteristics by applying a magnetic field from the coil. In the data acquisition, we applied voltages from -5 to 0 V to the coil, and we measured the current through the

TESs while changing the bias current applied to the TESs. The results of the IV measurement are shown in Fig. 8.1, and Fig. 8.2 shows a closer view of the IV characteristics of Ch41. The behaviors of Ch46 and 51 were extraordinary, most likely due to problems with the detectors themselves. Thus, we discarded those channels, and we decided to measure only the other 38 pixels in the following measurements. From the IV characteristics, the normal resistance R_n of TESs and the parasitic resistance R_p were found to be roughly 83 m Ω and 1.2 m Ω , respectively. We calculated the dissipation of all 38-pixel TESs at the specific bias point, which was defined as the ratio of the resistance of working point to that of the normal state, R/R_n , where R is the resistance of the working point. As an example, the dissipation of all 38-pixel TESs at a bias point of $R/R_n \approx 20\%$ is shown in Fig. 8.3. The maximum dissipation indicates that we could take full advantage of the TES and that the magnetic field is the optimum value to cancel out the residual field.

8.1.2 Pulse Shape Dependence on a Magnetic Field

We also measured pulse heights and fall-time constants while changing the applied magnetic field. About 100 pulses from the Mn K α line in a typical channel (Ch48) were collected and averaged, and the amplitude A_{ave} and the fall-time constant τ_{fall} were extracted by fitting the following average pulse model to the averaged Mn K α pulse.

$$P_{\text{ave}}(t) = A_{\text{ave}} e^{-\frac{t-t_{\text{shift}}}{\tau_{\text{fall}}}} \left(1 - e^{-\frac{t-t_{\text{shift}}}{\tau_{\text{rise}}}} \right), \quad (8.1)$$

where t_{shift} and τ_{rise} are the shift from the trigger time and the rise-time constant, respectively. The obtained averaged pulses of Ch48 with respect to the different fields are shown in Fig. 8.4. Also, the pulse amplitudes and fall-time constants are shown in Fig. 8.5; the maximum and minimum values of those parameters were around 1.1 Φ_0 and 390 μs . Furthermore, we also obtained a rise-time constant of roughly 10–20 μs . We do not know about the amplitude, but the fall and rise time constants agree reasonably well with the values SRON expects.

8.2 Optimization of TES Bias Point

TES characteristics such as gain and/or noise depend on the detector's working point. Here, we investigated the optimum bias point, at which the TES attains its potential energy resolution, by calculating an integrated noise equivalent power resolution ΔE_{NEP} given by Eq. 8.2 at each R/R_n bias point.

$$\Delta E_{\text{NEP}} = 2\sqrt{2 \ln 2} E \left(\int_0^\infty \frac{4df}{\text{NEP}(f)^2} \right)^{-\frac{1}{2}} \quad (8.2)$$

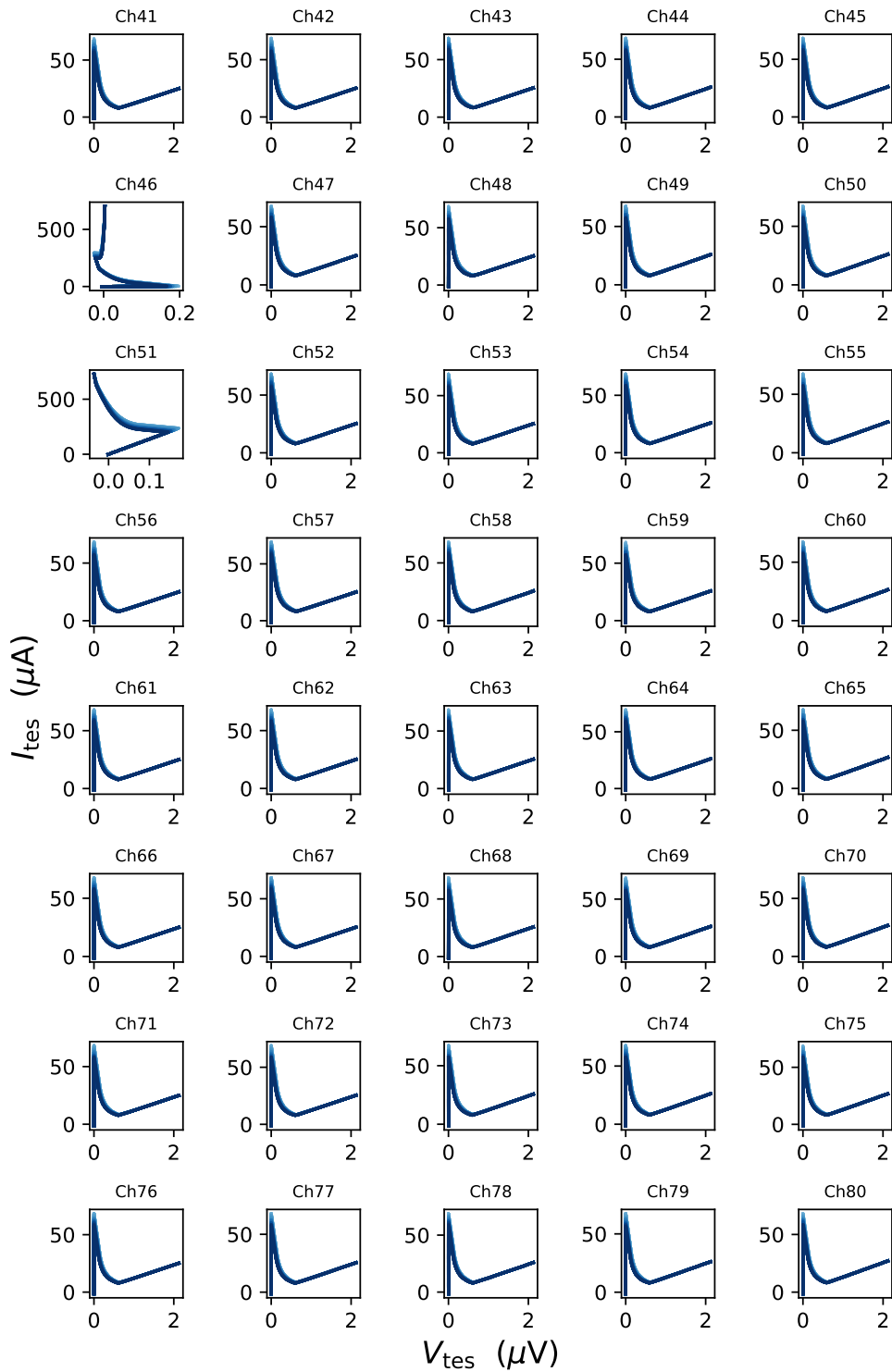


Figure 8.1: The IV characteristic of forty TESs. The behaviors of Ch46 and 51 are extraordinary and not suitable for readout TES signals.

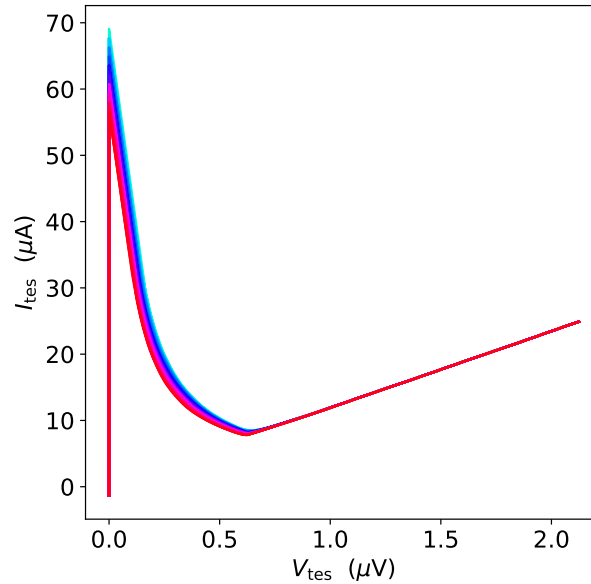


Figure 8.2: The IV characteristics of Ch41 with respect to different magnetic fields. The colors indicate the differences in the applied magnetic field.

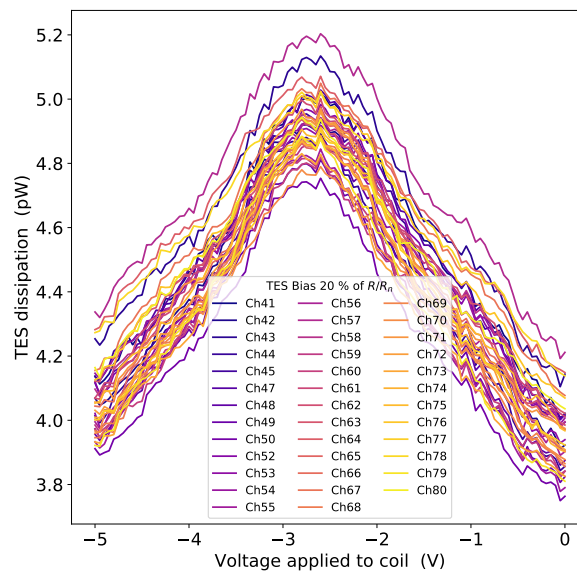


Figure 8.3: The dissipation of all 38-pixel TES at the bias point of 20% calculated from IV characteristics. The differences in maximum dissipation between channels could indicate the differences in the shunt resistance.

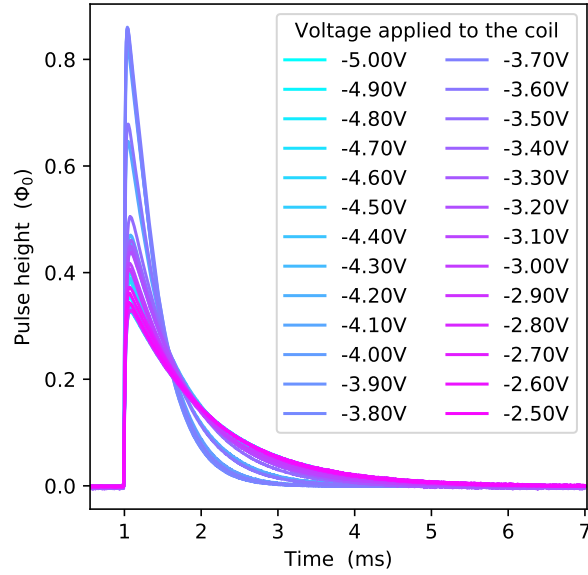


Figure 8.4: The averaged pulses of Ch48 under different fields.

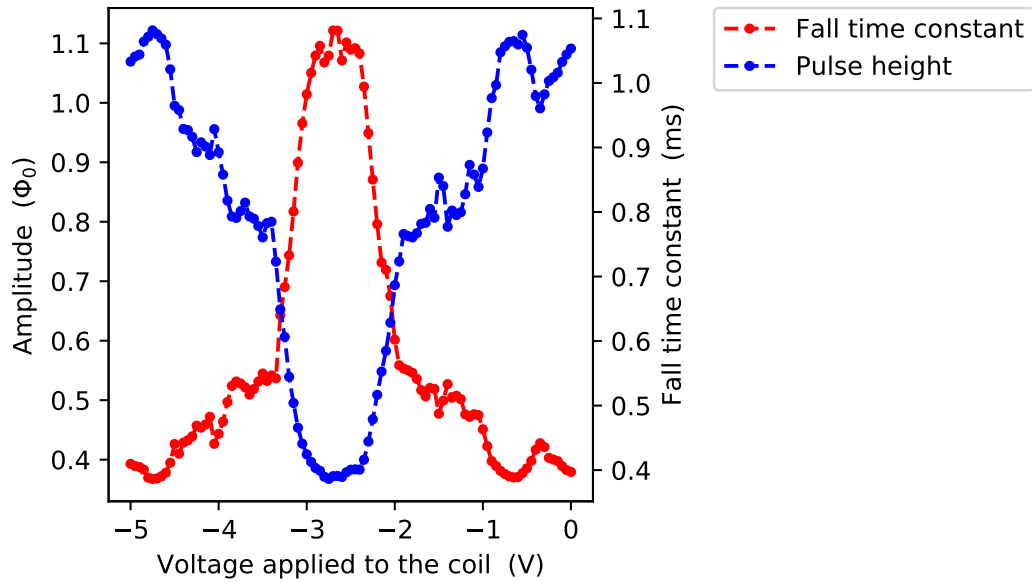


Figure 8.5: The amplitudes and fall time constants extracted from the averaged pulses under different fields of Ch48.

where $NEP(f)$ is defined as $NEP(f) \equiv \sqrt{2}NS(f)/PS(f)$, $NS(f)$ and $PS(f)$ are the noise spectrum and pulse spectrum, respectively. E is the expected energy, and now we consider the X-ray photon to be from Mn $K\alpha$. Therefore E is regarded as $E_{MnK\alpha}$, where $E_{MnK\alpha}$ is the energy of the Mn $K\alpha$ line. We collected about 100 pulses and noise records of the Mn $K\alpha$ line from the pixel in Ch72, as a representative TES, at bias points R/R_n from 10% to 30%, and estimated the integrated NEP resolution for these. The results shown in Fig. 8.6 indicate that we could exploit the TES's full ability at a bias point of around 20% of R/R_n . Thus, we set the bias point at around 20% of R/R_n in the following pulse collection measurement.

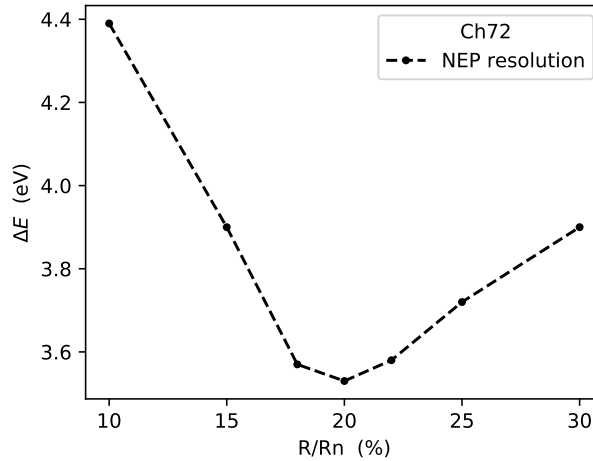


Figure 8.6: NEP resolution of Ch72 at different bias points.

8.3 Pulse Collection

Due to the gradients of the residual magnetic field and field applied by the coil, we could not optimize the field and TES bias point simultaneously for all pixels. However, we adopted the voltage applied to the coil of 2.67 V, and TES bias point of around 20%, and we stored pulses from ^{55}Fe in about 3 hours. We successfully detected X-ray photons on all 38 pixels, and we show the obtained averaged pulses of Mn $K\alpha$ in Fig. 8.7 and also the noise spectra in Fig. 8.8. The rise-time and fall-time constants of the averaged pulses were respectively 10–20 μs and 350–500 μs for all pixels. We have not understood what causes pulse shapes to be different from pixel to pixel, although the candidates are expected to be poor uniformity of

TES pixels, a gradient of the residual magnetic field and/or temperature on each pixel, and differences in bias point. The noise spectra differ between pixels, but all of them are below the noise of the MWMUX. The difference in the noise spectrum between pixels could come from the difference in pulse shape.

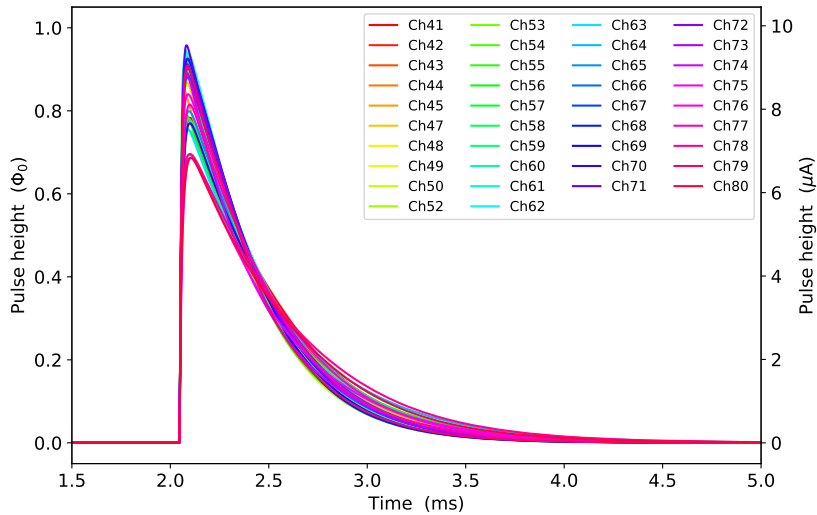


Figure 8.7: The averaged pulses of all 38 pixels.

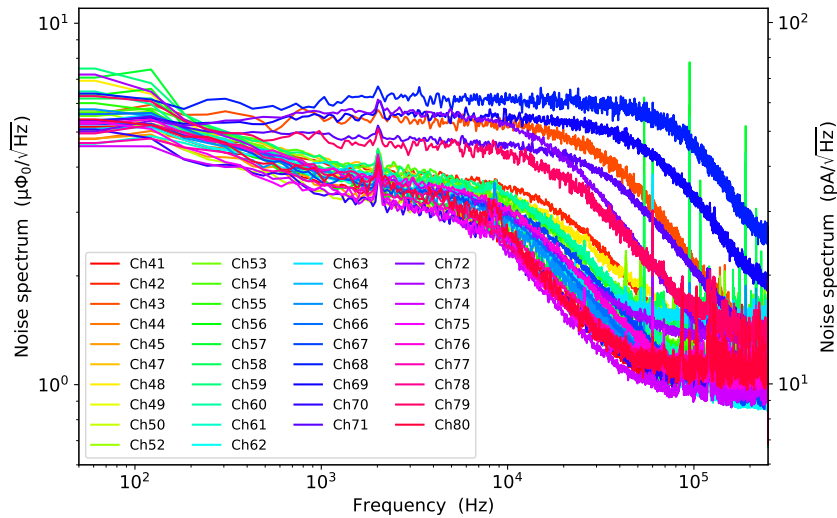


Figure 8.8: The noise spectra of all 38 pixels.

Using the data sets of Mn $K\alpha$ pulses, we constructed an energy spectrum and evaluated an energy resolution, or a precise determination of the pulse height, of the detector. In the following, we describe how the pulse heights were estimated and how we evaluated the energy resolution from the obtained energy spectrum.

8.3.1 Optimal Filtering

To reach the theoretical energy resolution of the TES, we generally apply so-called optimal filtering [75] to pulse data. In this processing, we use not only the pulse-peak value but also the complete information of the pulse. We assume that all the pulses have the same shape, and the noisy data $D(t)$ we acquire in an experiment can be given by

$$D(t) = H \times S(t) + N(t), \quad (8.3)$$

where H , $S(t)$, and $N(t)$ are the optimal pulse height estimate, the pulse shape model, and the noise in the time domain, respectively. We transfer the expression above into the frequency domain and define the test function χ^2 to be minimized as

$$\chi^2 \equiv \sum \frac{|D(f) - H \times S(f)|^2}{|N(f)|^2} \quad (8.4)$$

in the same fashion as the least-squares method. The deviation of χ^2 with respect to H to be zero yields that the optimal estimation of the pulse height H can be written as

$$H = \frac{\sum D(f) \frac{S^*(f)}{|N(f)|^2}}{\sum \left| \frac{S(f)}{N(f)} \right|^2}, \quad (8.5)$$

where $S^*(f)$ is the complex conjugate of $S(f)$. This equation can be transferred back into the time domain, and we finally find the optimal estimation of the pulse height H as

$$H = \sum D(t) \times T(t). \quad (8.6)$$

Here we discard the constant coefficient of $\sum |S(f)/N(f)|^2$ for simplicity. $T(t)$ is a template for the optimal filtering and defined as

$$T(t) \equiv \mathcal{F}^{-1} \left[\frac{S^*(f)}{|N(f)|^2} \right], \quad (8.7)$$

where \mathcal{F}^{-1} denotes the inverse-Fourier transformation. For $S(t)$ and $N(f)$, we usually use an averaged pulse and averaged noise spectrum density. In our community, we call the optimal filtered pulse height estimate the pulse height amplitude (*PHA*). Therefore, we use this expression in the following context. Figure 8.9 simply shows the flowchart of the signal processing with optimal filtering. In the

processing, we produce an energy spectrum from the obtained pulse data by the following procedure:

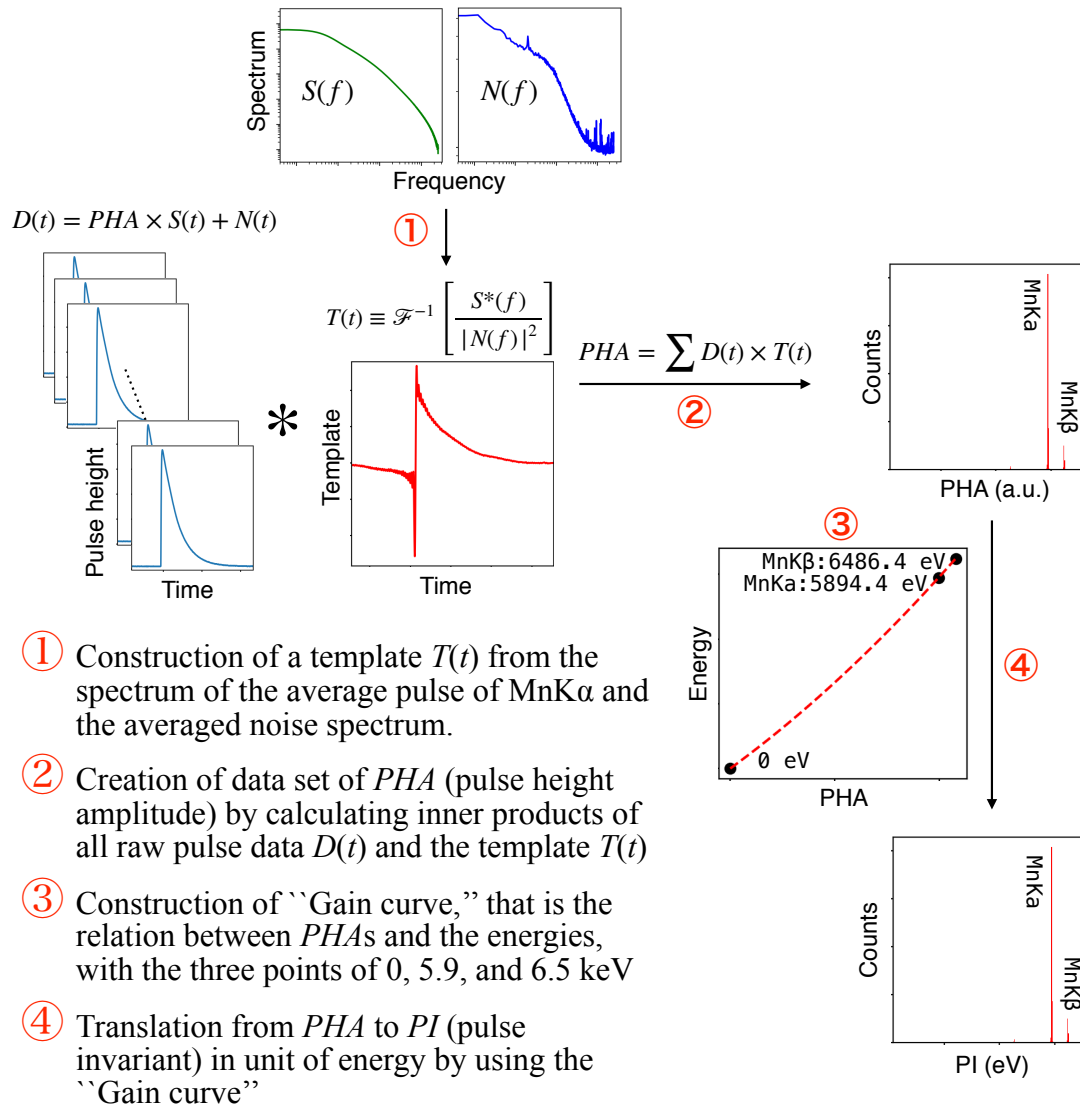


Figure 8.9: Flowchart of the signal processing with optimal filtering.

1. We first create a template $T(t)$ used as the optimal filter with the spectrum of the averaged Mn K α pulse $S(f)$, and the averaged noise spectrum $N(f)$. There is a lot of flexibility to create $T(t)$. We can apply some filters such as low- and/or band-pass filters to $S(f)$ in order to find an appropriate template.

2. We calculate the cross-correlations of all noisy pulses $D(t)$ and the template $T(t)$ created above to construct the PHA data set. To mitigate the arrival-time effect, we calculate the lag-correlations to estimate authentic PHA (see Subsec. 8.3.2).
3. After applying gain-drift correction (see Subsec. 8.3.3), if we need, we construct a “Gain curve” that is the translation function to convert PHA to PI (pulse invariant) in the unit of energy. The “Gain curve” is here constructed by fitting a quadratic function to the three points of 0, 5.9 (Mn $K\alpha$), and 6.5 keV (Mn $K\beta$).
4. We translate PHA to PI with the “Gain curve,” and we obtain the energy spectrum.

8.3.2 Construction of PHA Data Sets

We estimate a real pulse shape by reproducing it from a finite number of sampling points. Thus we cannot know the exact X-ray photon arrival time. A difference between an X-ray photon arrival time and the clock sample time appears to cause small differences in the pulse shapes, and this arrival-time effect can degrade the energy resolution due to misjudging the exact pulse shape. To correct this effect, we applied 3-dB filtering and a lag correlation when we constructed the template for optimal filtering and estimated the PHA by correlating raw pulses with this template.

The 3-dB filtering cuts off the high-frequency side of the pulse spectrum by a low-pass filter and damps the template, which reduces the contribution of the pulse-rise slope to the pulse estimation and mitigates the effect of not knowing the exact arrival time. In the lag correlation regime, we constructed 5-lag correlations between raw pulses and template by correlating raw pulses and template shifted by a sample, whose interval was $2\ \mu s$, with respect to the trigger point. Fitting a quadratic function of 5-lag correlations as shift points to the values, we could estimate the lag where the PHA is maximum.

In this experiment, low-frequency noise could affect energy resolution. Thus we also applied a zero-frequency DC-offset filtering, which reduced the contribution of the DC offset by making the DC offset in the frequency domain be zero when we created the templates. In Fig. 8.10, we show the templates of all 38 pixel TESs generated by using their averaged pulse (Fig. 8.7) and noise spectra (Fig. 8.8). We show an example of the effects of these three corrections: zero DC-offset filtering, 3-dB filtering, and 5-lag correlations, in Fig. 8.11.

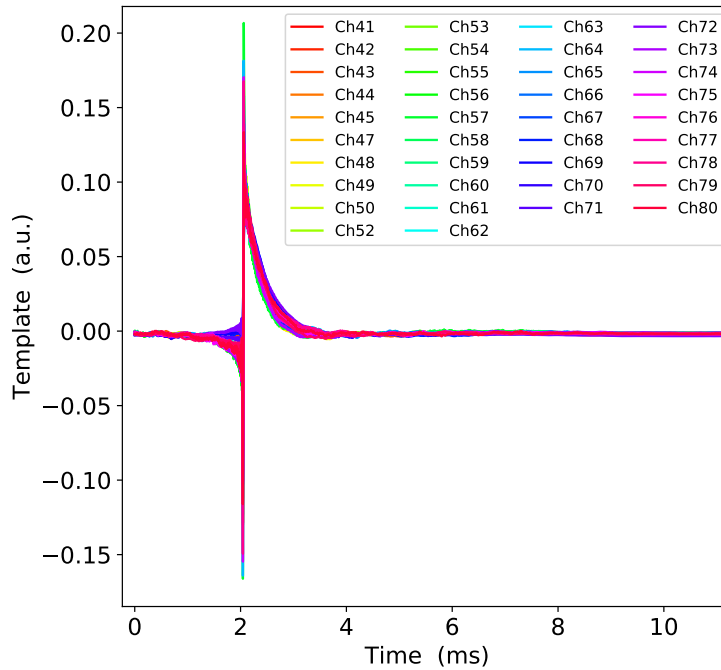


Figure 8.10: Templates of all 38 pixels used in this experiment.

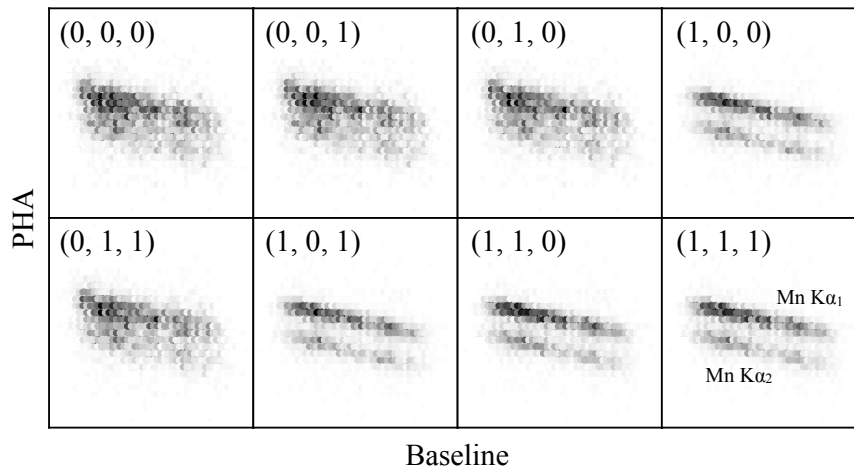


Figure 8.11: The correlations between baseline and *PHA* for only one channel. The baseline is defined as the mean value of the pre-triggered pulse absent data. These plots show the effects of these three corrections: zero DC-offset filtering, 3-dB filtering, and 5-lag correlations. The legends indicate whether those corrections are applied “1” or not “0” in the order from left to right: zero DC-offset filtering, 3-dB filtering, and 5-lag correlations.

8.3.3 Gain-drift Correction

The gain of a TES can vary over time due to factors such as a large-time scale temperature drift of the cryogenic stage and/or room-temperature electronics, and this effect can also affect the energy resolution if left uncorrected. We corrected this effect by following the method suggested by J. W. Fowler [76]. In Fig. 8.12 (*top right*), we show the correlation between baseline and PHA of Mn $K\alpha_1$ and Mn $K\alpha_2$ before treating the correction. The baseline is defined as the mean value of the pre-triggered pulse-absent data. The correlation is linear in the baseline, and Mn $K\alpha_1$ and Mn $K\alpha_2$ are clearly separated off. Those lines are however not perpendicular to the PHA axis, hence the PHA histogram, or the correlation projected to the PHA axis, looks like a lump as shown in Fig. 8.12 (*top left*) and causes the degradation of energy resolution. We correct the PHA to remove the correlation by using the following equation

$$PHA'_j = PHA_j[1 + \alpha_{DC}(B_j - B_0)], \quad (8.8)$$

where PHA_j and PHA'_j are the plain and corrected PHA for pulse j ; B_0 and B_j are the median baseline and the baseline for that pulse; α_{DC} is the gain slope and is the only free parameter in the equation. The α_{DC} is determined in such a way that the PHA histogram is the sharpest possible spectrum. The sharpness can be quantified by the Shannon entropy of the histogram, and we define an estimated spectral entropy H_{DC} as

$$H_{DC} = - \sum_i^{N_b} f_i \ln f_i, \quad (8.9)$$

where N_b and f_i are bins of a normalized PHA histogram, and the fraction of all pulses contained in bin i , respectively. We select α_{DC} that minimizes the spectral entropy H_{DC} . In Fig. 8.12 (*bottom right*) and (*bottom left*), we finally show the correlation between baseline and corrected PHA , and the histogram of the corrected PHA , respectively.

8.3.4 Hölzer Fit to Mn $K\alpha$ Line Complex

After constructing corrected PHA data, we convert them to pulse invariant (PI) data in units of eV by using a quadratic response function passing through the zero, Mn $K\alpha$ and Mn $K\beta$ lines. We assessed the energy resolution via fitting the PI data to the two-peaked shape of the Mn $K\alpha$ line complex with the natural line shape given by Tab. 8.1 [58] by using the maximum likelihood method. Our fit model M is described as:

$$M = \sum_i A_m \times \Delta_{bin} \times I_{int,i} \times Voigt\left(E - E_i - E_{shift}, \frac{W_i}{2}, \frac{\Delta E}{2\sqrt{2 \ln 2}}\right), \quad (8.10)$$

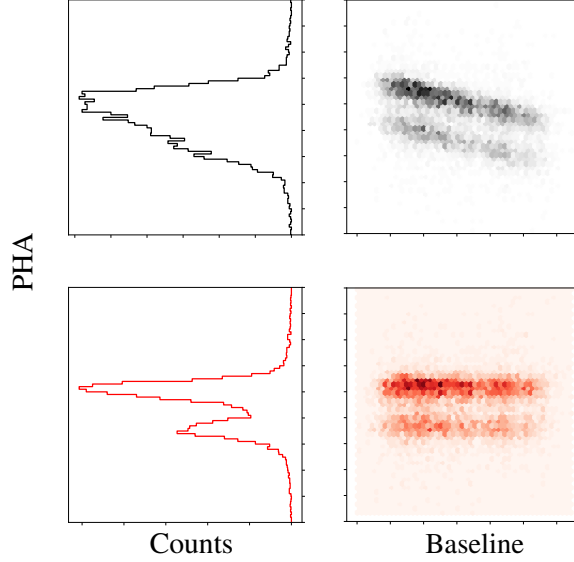


Figure 8.12: The gain drift and correlation between baseline and *PHA* (only one channel is shown as an example). The top and bottom rows are before and after correction, respectively. In the correlation between baseline and *PHA*, Mn $K\alpha_1$ and Mn $K\alpha_2$, which are fine structures of the Mn $K\alpha$ line, are clearly separated.

where the free parameters A_m , E_{shift} , and ΔE are scale factor, energy shift, and energy resolution, which is the full-width-at-half-maximum (FWHM) of a Gaussian, respectively; Δ_{bin} and E are the binsize and energy; E_i , W_i , and $I_{\text{int},i}$ are the center energy, or position, width, and integrated intensities of fine structure i come from Tab. 8.1; *Voigt* denotes the Voigt profile which is a probability distribution given by a convolution of a Cauchy-Lorentz distribution and a Gaussian distribution, and is written as

$$\text{Voigt}(E, \gamma, \sigma) = \frac{\Re[w(z)]}{\sigma\sqrt{2\pi}}, \quad (8.11)$$

where \Re denotes the real part, and

$$z = \frac{E + i\gamma}{\sigma\sqrt{2}} \quad \text{and} \quad w(z) = e^{-z^2} \left(1 + \frac{2i}{\sqrt{\pi}} \int_0^z e^{t^2} dt \right). \quad (8.12)$$

Table 8.1: Mn $K\alpha$ line complex. E_i , W_i , I_i , and I_{int} are positions, widths, amplitudes, and integrated intensities of the line.

Peak	$K\alpha_1$				Peak	$K\alpha_2$			
	E_i (eV)	W_i (eV)	I_i	I_{int}		E_i (eV)	W_i (eV)	I_i	I_{int}
α_{11}	5898.853	1.715	0.790	0.3527	α_{21}	5887.743	2.361	0.372	0.2286
α_{12}	5897.867	2.043	0.264	0.1404	α_{22}	5886.495	4.216	0.100	0.1098
α_{13}	5894.829	4.499	0.068	0.0796					
α_{14}	5896.532	2.663	0.096	0.0666					
α_{15}	5899.417	0.969	0.0714	0.018					
α_{16}	5902.712	1.5528	0.0106	0.0043					

8.3.5 Result

Finally, we obtained energy spectra of the 5.9 keV Mn $K\alpha$ line for all 38 TES pixels as shown in Fig. 8.13. The best energy resolution and median value of all pixels are 2.79 ± 0.09 eV (Figs. 8.14a and 8.14b) and 3.3 eV, respectively. We also constructed the summed spectrum of all 38 pixels, and we evaluated the energy resolution as 3.40 ± 0.02 eV. This 38-pixel spectrum is shown in Fig. 8.15, and its histogram is also shown in Fig. 8.16. More details of energy spectra and correlations of baselines and *PHAs* of all 38 pixels are shown in Appx. C. The energy resolutions are shown on the pixel map in Fig. 8.17, and we cannot clearly find any correlation between the energy resolution and the position on the map.

8.4 Summary

We simultaneously read out the 38 TESs with our developed 40ch MWMUX by using only six wires from the room-temperature electronics to the low-temperature cryogenic stage. The bias point and magnetic field applied to the TESs were optimized as much as possible. We successfully detected X-ray photons from 38 pixels. The best energy resolution and the median value of all pixels were obtained as 2.79 ± 0.09 eV and 3.3 eV, respectively. The energy resolution of the 38-pixel summed spectrum was achieved as 3.40 ± 0.02 eV.

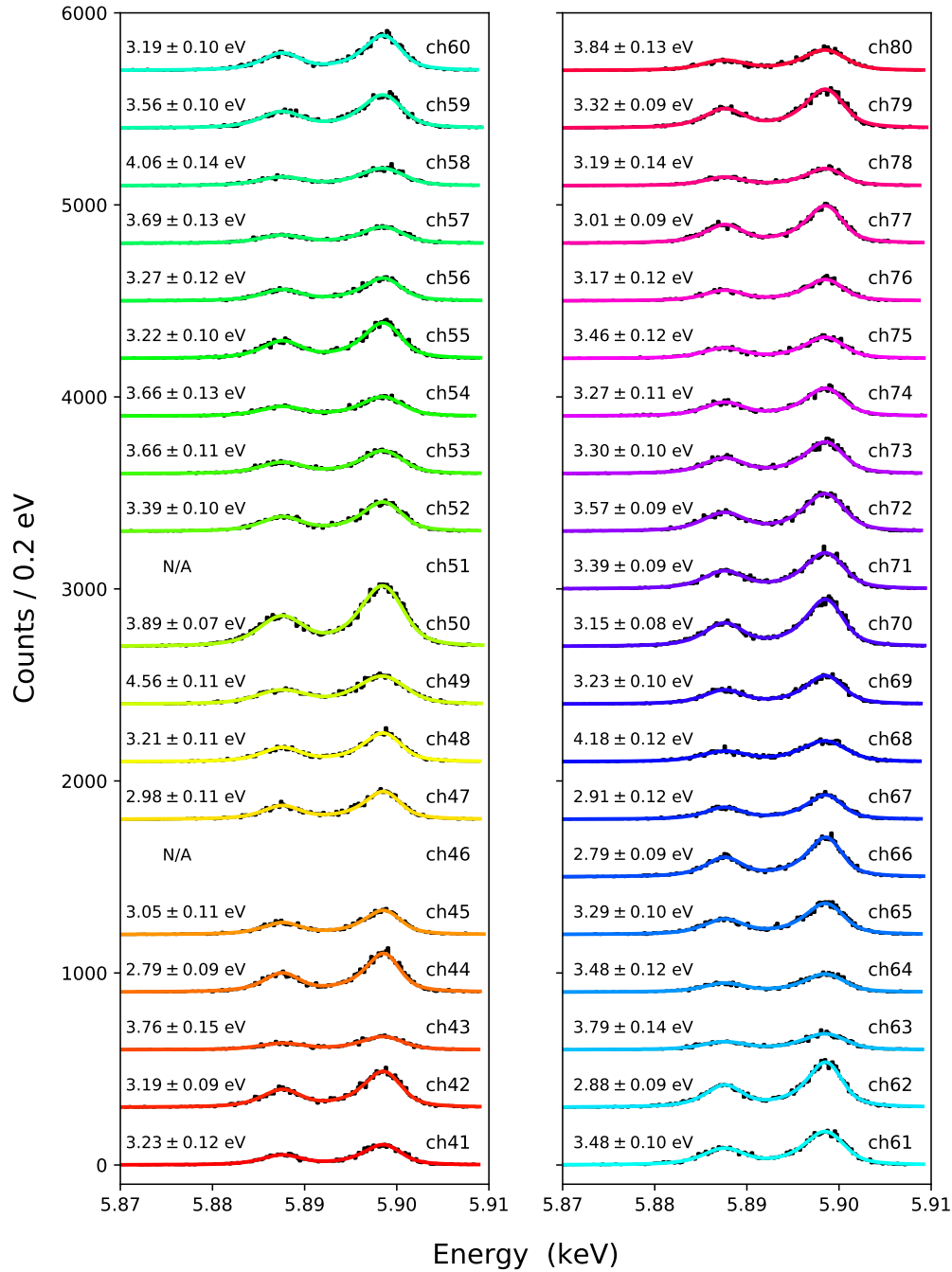
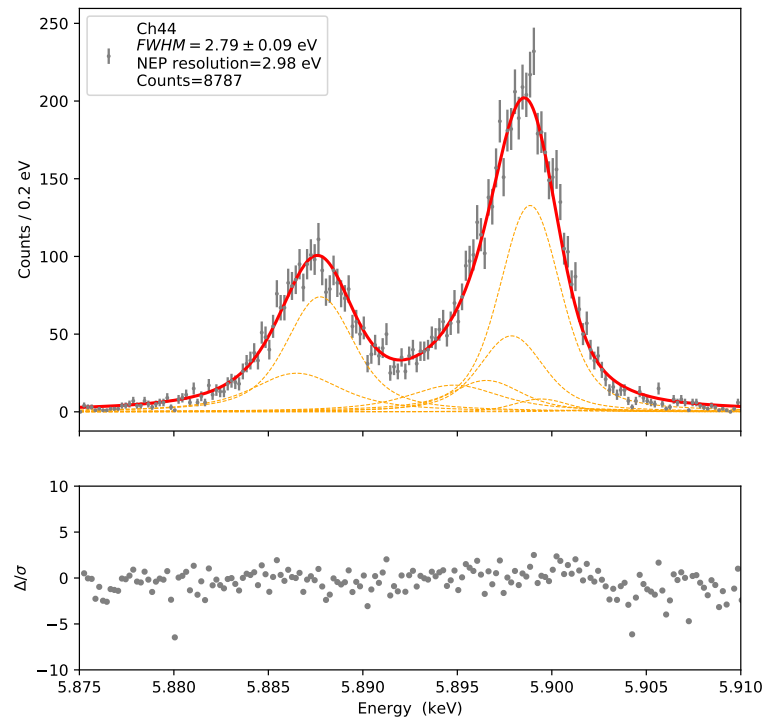
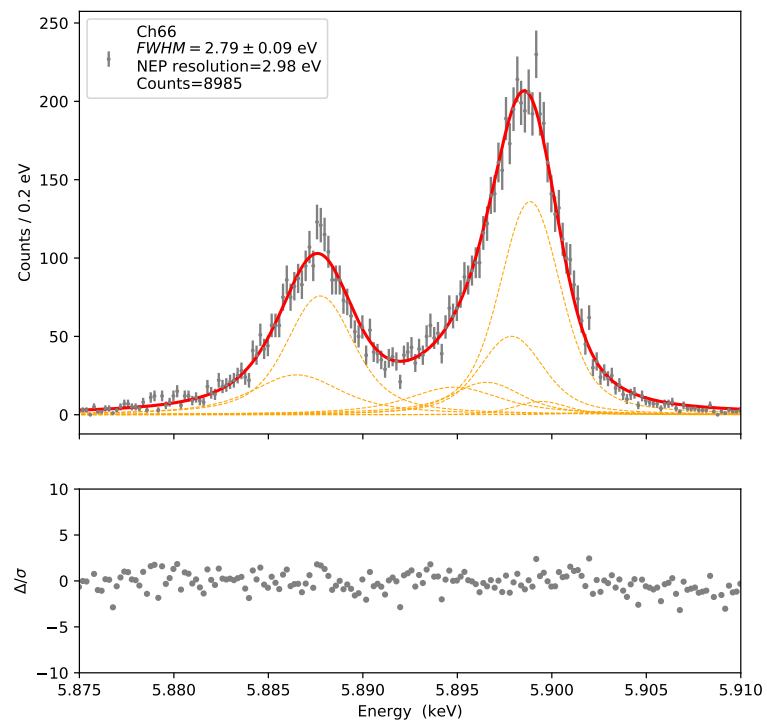


Figure 8.13: The obtained energy spectra from all 38 TES X-ray microcalorimeters.



(a) The energy spectrum of Ch44.



(b) The energy spectrum of Ch66.

Figure 8.14: The energy spectra with the best-recorded energy resolution of 2.79 ± 0.09 eV.

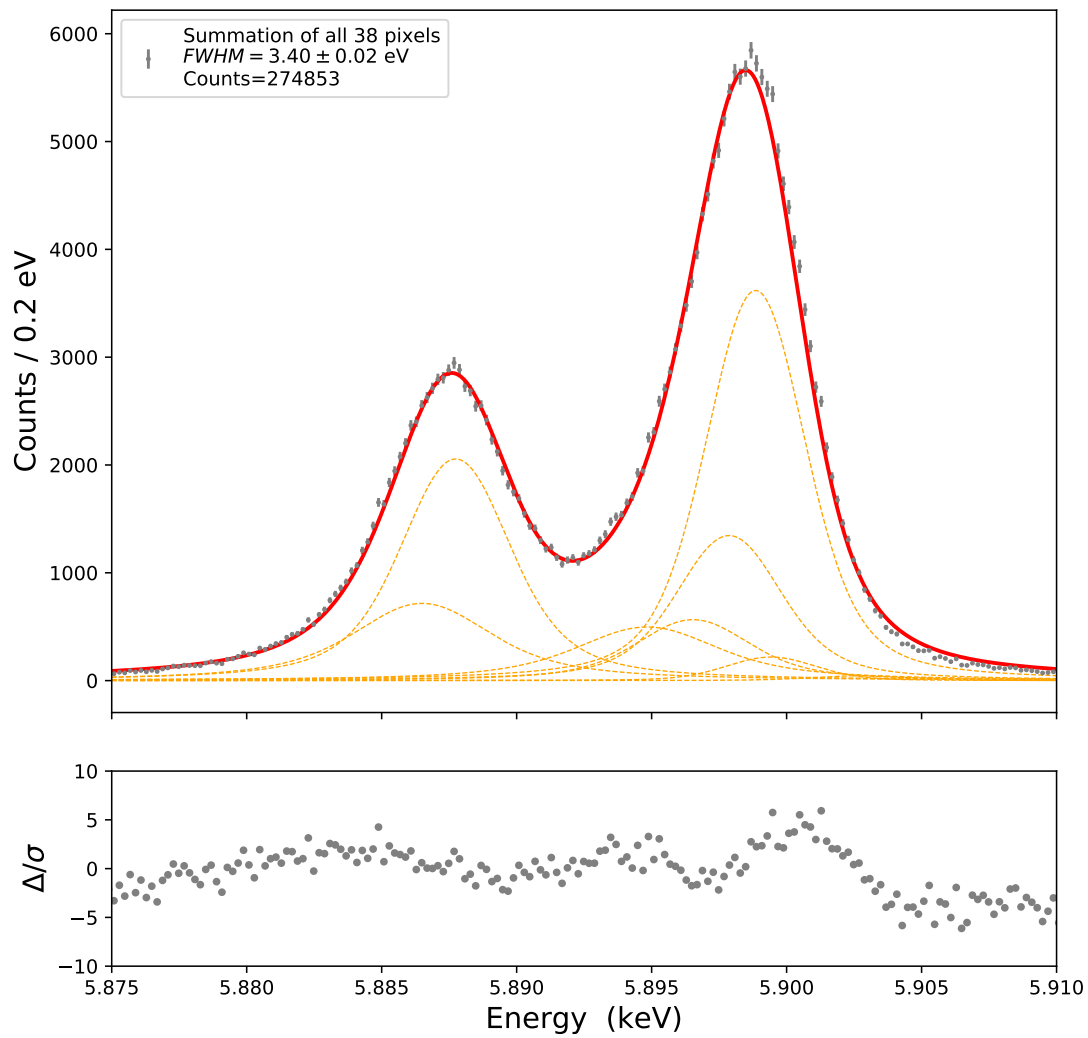


Figure 8.15: The combined energy spectrum from 38 pixels measured simultaneously with MWMUX readout.

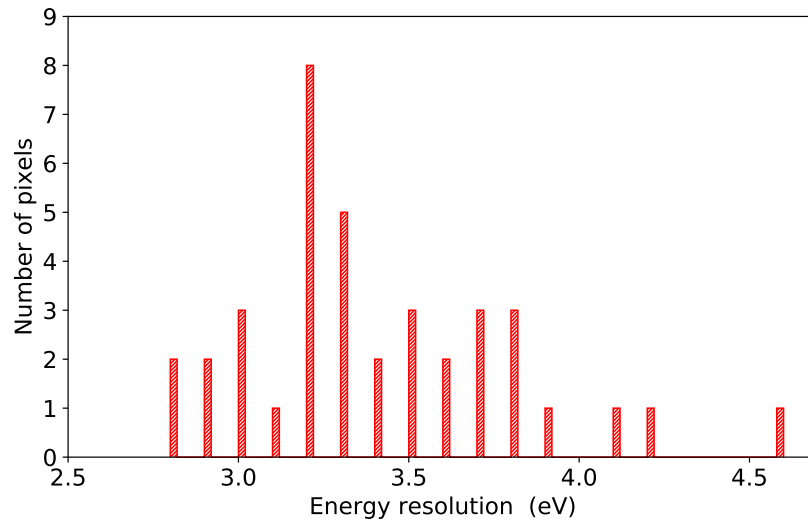


Figure 8.16: The histogram of the energy resolutions among all 38 pixels.

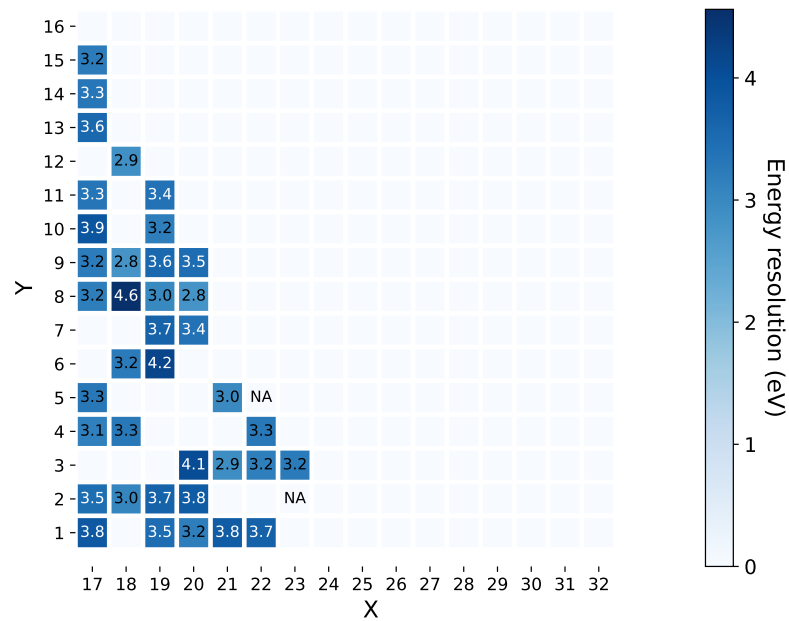


Figure 8.17: The energy resolutions on the TES pixel map. The left top is the center of the TES array, and the number on each pixel corresponds to the energy resolution.

Chapter 9

Discussion

We successfully read out 38 TES pixels with our developed 40ch MWMUX by using two pairs of coaxial cable for microwave and flux-ramp lines and a twisted-pair cable. The best energy resolution and the median value of all pixels at the 5.9 keV Mn $K\alpha$ line were 2.79 ± 0.09 eV and 3.3 eV, respectively. This result surpasses the performance of the SXS instrument, which was on board the *Hitomi* satellite and operated in orbit in 2016, in both the energy resolution and the number of pixels. Furthermore, the obtained result is comparable to the requirement of 2.5 eV with a 40-pixel FDM multiplexing readout for the *Athena* satellite to be launched in 2031.

In what follows, we discuss room for consideration and prospects in terms of energy resolution and the number of multiplexed pixels toward MWMUX on board future satellites.

9.1 Energy Resolution

The obtained energy resolutions in Chap. 8 vary from 2.8 to 4.6 eV, and the variation is about 2 eV. Three probable factors causing the energy resolution nonuniformity among pixels are considered as follows: First, poor uniformity of the detector itself. Second, the existence of a temperature gradient among the pixels. Third, imperfect cancellation of the residual magnetic field. These effects should be assessed for a more uniform readout.

We estimated contributions of the readout noise to energy resolution by calculating the integrated NEP resolutions of the noise spectra taken at a bath temperature of 125 mK, which is above the TES transition temperature. These noise spectra shown in Fig. 9.1 include not only the readout noise, but also the thermal Johnson noise of the TES normal resistance of roughly $0.9 \mu\Phi_0/\sqrt{\text{Hz}}$, assuming $R_n = 83 \text{ m}\Omega$. We found the contributions of the readout noise to the energy reso-

lutions is 1.0 to 1.8 eV as shown in Fig. 9.2. The readout noise in the MWMUX does not affect the energy resolution, though the intrinsic energy resolution of the detectors has not been evaluated because we have not assessed the detector in a mature conventional DC measurement. Even in the worst case, the readout noise contribution only accounts for 13%, which comes from the energy resolution of 3.2 eV and the readout noise contribution of 1.6 eV. We compare the readout noise contribution obtained in our experiment with the state-of-the-art design of the TES detector system on the *Athena* mission as an example of a future space mission. In the *Athena* mission, the breakdown of energy resolution to achieve the requirement of 2.5 eV is 1.9 eV for the TES detector array and 1.6 eV for the other components [77]. The readout noise contribution of 1.3 eV, which is the median value of our result, meets the requirement of 1.6 eV, and the worst case of 1.8 eV is even not bad, but there is a little room for improvement. We suggested a scheme to suppress the contribution of the white noise component by increasing the mutual inductance M_{in} between the SQUID and the TES circuit. In Chap. 5, we successfully enlarged M_{in} and demonstrated M_{in} was not restricted by parasitic resonances. Recall from Eq. 3.56 that M_{in} is constrained by the slew rate which can be expressed as $dI_{\text{tes}}/dt < \Phi_0 f_{\text{ramp}}/2M_{\text{in}}$. In Fig. 9.3, we show the TES slew rate dI_{tes}/dt and that of MWMUX used in the experiment. This figure implies M_{in} can be roughly twice as large as the current value of ~ 210 pH. As a result, we can improve the white readout noise below ~ 5 pA/ $\sqrt{\text{Hz}}$.

Finally, we enumerate probable contributions to energy resolution, but we have not evaluated them.

- The existence of a temperature gradient among the pixels
- A residual magnetic field not canceled out sufficiently
- Thermal crosstalk between TES pixels
- Electrical crosstalk between resonators
- Power saturation of HEMT at 4 K and RF components at room temperature

For future prospects, we should clear the budgets of the probable contributions to energy resolution and optimize the readout system, including an adjustment of the experimental environment, such as controlling the magnetic field and the temperature.

9.2 Number of Multiplexed Pixels

We successfully read out 38 channels multiplexed using only less than 20% of the 4 GHz-bandwidth of HEMT amplifier. We can simultaneously read out 240

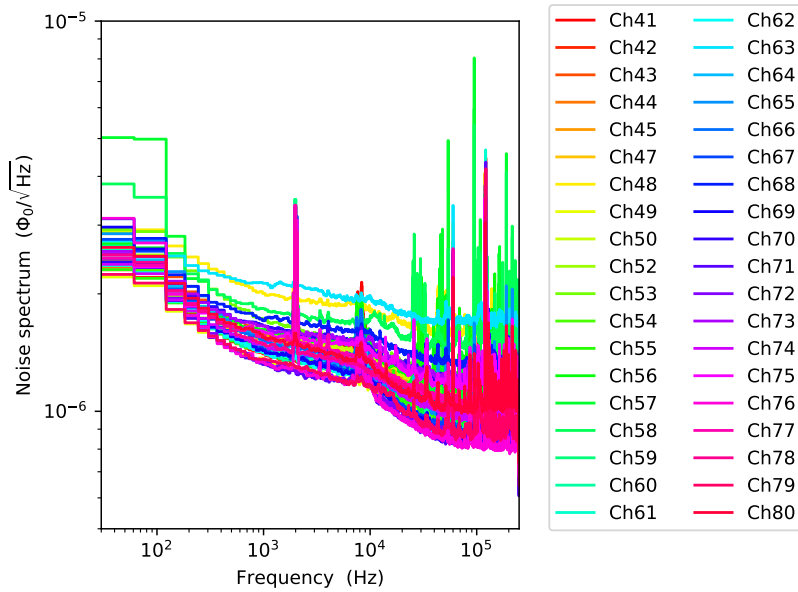


Figure 9.1: The noise spectra taken at a bath temperature of 125 mK, which is above TES transition temperature. These spectra include the contribution of the thermal Johnson noise of TES normal resistance. Assuming $R_n = 83 \text{ m}\Omega$, the contribution is $\sim 0.9 \mu\Phi_0/\sqrt{\text{Hz}}$.

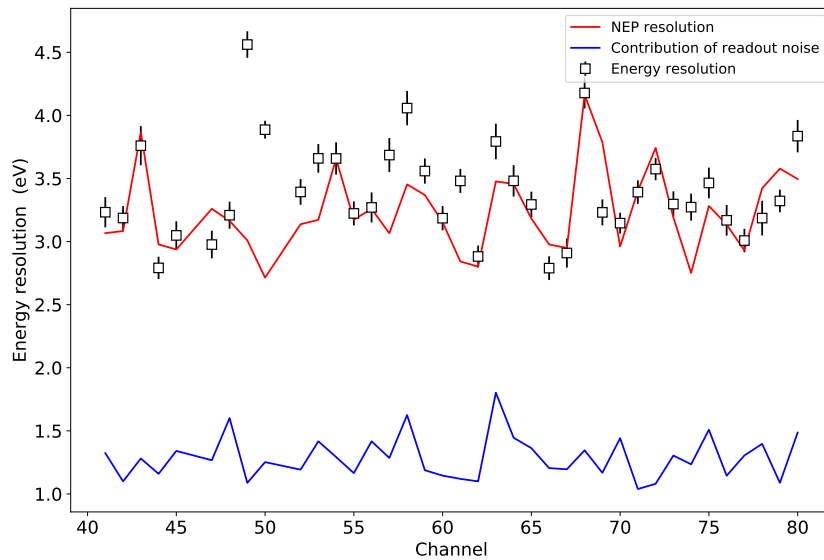


Figure 9.2: The comparison of the energy resolutions, integrated NEP resolutions, and the expected readout noise contributions, which are calculated from the results in Fig. 9.1, on each channel.

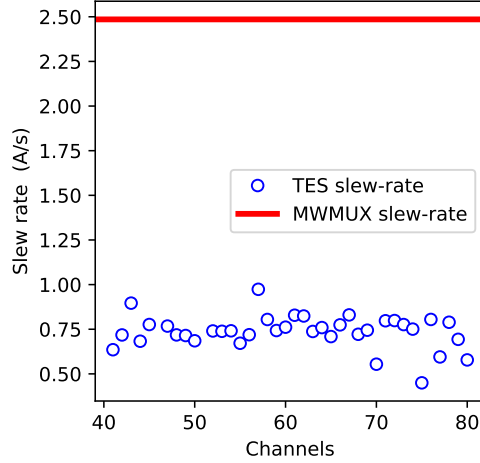


Figure 9.3: The slew rate of Mn $K\alpha$ pulses of all 38 TES pixels. These are calculated from the maximum time derivative of averaged pulse $(dI_{\text{tes}}/dt)_{\text{max}}$.

pixels with a pair of coaxial cables if the full band of a HEMT could be used. Furthermore, a wide-band HEMT with 8 GHz-bandwidth and parallelization of HEMTs would make it possible to increase the number of pixels by 10–100 times. Besides, a multi-absorber TES known as a *hydra*, which is being actively developed for *Lynx* [20], could increase the number of multiplexed pixels by 10–100 times. In the *hydra* configuration, a TES has multiple absorbers with different thermal conductances to the TES, and we can read out multiple pixels with one TES at the same time. Utilizing those techniques, the number of multiplexed pixels read out with a pair of coaxial cables becomes 1000–10000.

9.3 Summary

In this chapter, we discussed room for consideration and future prospects in terms of energy resolution and the number of multiplexed pixels toward MWMUX on board future satellites. The estimated contributions of the MWMUX readout noise to the energy resolution were 1.0–1.8 eV and almost meet the requirement of future astrophysical observation, and we can further suppress the contributions by increasing the coupling between SQUID and TES and reducing the readout current noise. Use of a wide-band HEMT, parallelization of HEMTs, and multi-absorber TESs could increase the technological feasibility to read out 1000–10000 pixels by MWMUX with a pair of coaxial cables for microwave lines.

Chapter 10

Conclusion

In this dissertation, we developed a microwave SQUID multiplexer (MWMUX) to read out a transition-edge sensor (TES) X-ray microcalorimeter array for future astrophysical observations. Through the research of this thesis, we obtained the following achievements:

- We have developed MWMUX with large resonance bandwidth of 2 MHz.
- Using MWMUX with $BW > 2$ MHz, we successfully detected X-ray photons from TESs.
- We have developed MWMUX with low noise below $10 \text{ pA}/\sqrt{\text{Hz}}$.
- We have developed MWMUX with 40 channel in a ~ 640 MHz band.
- We successfully read out the 38 TES pixels with our developed 40ch MWMUX by using only two pairs of coaxial cable for microwave and flux-ramp lines and a twisted-pair cable for TES bias.
- The best energy resolution and the median value of all pixels at 5.9 keV Mn $K\alpha$ line were $2.79 \pm 0.09 \text{ eV}$ and 3.3 eV , respectively.
- This result surpasses the performance of the SXS instrument, which was on board the *Hitomi* satellite and operated in orbit in 2016, in both the energy resolution and the number of pixels.
- The obtained result is comparable to the requirement of 2.5 eV with a 40-pixel FDM multiplexing readout for the *Athena* satellite to be launched in 2031.
- The estimated contributions of the MWMUX readout noise to the energy resolution were 1.0–1.8 eV and almost meet the requirement of future astrophysical observations.

For the first time in the world, we have developed MWMUX with low readout noise, we successfully read out the 38-pixel TESs with the developed 40ch MWMUX, and we obtained the best energy resolution and the median resolution for all pixels, at the 5.9 keV Mn $K\alpha$ line, of 2.79 ± 0.09 eV and 3.3 eV, respectively. The results in this thesis will impact X-ray astronomy by making it feasible to realize an X-ray camera with a high precision spectrometer on each pixel for future X-ray astronomical observatories.

Appendix A

List of Instruments and Components

The instruments and components used in this work were as follows:

- LNF-LNC4.8C s/n 631Z (Low Noise Factory)
- LNF-PS_3 (Low Noise Factory)
- E3630A (KEYSIGHT)
- QCY-060400C000 (QuinStar)
- DC Block 8039 (API/Inmet)
- SA18H-xx (Fairview Microwave)
- AD1000 (Arlon) processed by SHINKOU PHOTO SERVICE Co
- SMA 2985-6037 (Amphenol)
- ND2A225SSMHPG1 (Axon')
- ND2A225PWX3W010PX (Axon')
- SC-086/50-NbTi-NbTi (COAX CO)
- SC-219/50-CN-CN (COAX CO)
- Cryophy magnetic shield (OHTAMA CO)
- H105VFF (MTC)
- EK-U1-KCU105-G (Xilinx)

- AD-FMCDQAQ2-EBZ (Analog Devices)
- SCLPF-8400/T9000-O/O (Sogo Electronics)
- SCLPF-450/T600-O/O (Sogo Electronics)
- ZFBT-4R2GW+ (Mini-Circuits)
- PS2-14-450/8S (Pulsar)
- IQ-4509LXP (Marki)
- PSG CW Signal Generator E8247C (Agilent)
- ABL0100-01-3010 (Wenteq)
- AD-8723D (A&D)
- FS725 Benchtop rubidium frequency standard (SRS)
- WF1968 (NF)
- EXA Signal Analyzer N9010A (KEYSIGHT)
- PNA Network Analyzer E8362C (Agilent)
- AFSX3-04000800-15-10P (Miteq)
- USB-6211 (NI)
- AFG3252 (Tektronix)
- Bi-polar DC Power Supply BOP 20-20M (Kepco)
- Model 372 AC Resistance Bridge (Lake Shore Cryotronics)
- Model 218 Temperature Monitor (Lake Shore Cryotronics)
- UPS BN150XR (OMRON)
- ADQ23Q04H (Panasonic)
- ADR Cryostat Model 102 Denali (HPD)
- PT407-RM (CRYOMECH)
- CPA286i (CRYOMECH)
- EPS-002 (CRYOMECH)
- MNR-D-9-1010 (UNION ELECTRIC Co)

Appendix B

Superconducting Microstrip Line Inductance

The SQUID inductor is formed by a superconducting microstrip line having strip width w , strip thickness t_s , ground plane thickness t_g , and dielectric substrate thickness h as shown in Fig.B.1. W. H. Chang presented an accurate analytical inductance formula for a superconducting microstrip line by taking into account the fringe field [53]. This formula is valid if the aspect ratio u , defined as the ratio of the strip width to the thickness of the substrate $u = w/h$, of the stripline is large or exceeds about unity. We assume that both the strip and the ground plane are made of the same material, that is to say, the London magnetic penetration depths λ_L [54] of the electrodes are the same value. Then the superconducting microstrip-line inductance per unit length L_{MS} (H/m) given by Chang can be written as:

$$L_{MS} = \frac{\mu_0}{wK(u, t_h)} \left[h + \lambda_L \left\{ \coth \left(\frac{t_s}{\lambda_L} \right) + \frac{2\sqrt{p}}{r_b} \operatorname{csch} \left(\frac{t_s}{\lambda_L} \right) + \coth \left(\frac{t_g}{\lambda_L} \right) \right\} \right], \quad (\text{B.1})$$

where μ_0 and $K(u, t_h)$ are the permeability of vacuum and the fringe field factor, respectively. $K(u, t_h)$ is a function of the aspect ratio u and the strip thickness normalized by the dielectric substrate thickness $t_h = t_s/h$, and is given by:

$$K(u, t_h) = \frac{2}{\pi u} \ln \left(\frac{2r_b}{r_a} \right), \quad (\text{B.2})$$

where r_a and r_b are defined as follows:

$$\ln r_a = -1 - \frac{\pi u}{2} + \ln 4p - \frac{(\sqrt{p} + 1)^2}{2\sqrt{p}} \ln(\sqrt{p} + 1) + \frac{(\sqrt{p} + 1)^2}{2\sqrt{p}} \ln(\sqrt{p} - 1) \quad (\text{B.3a})$$

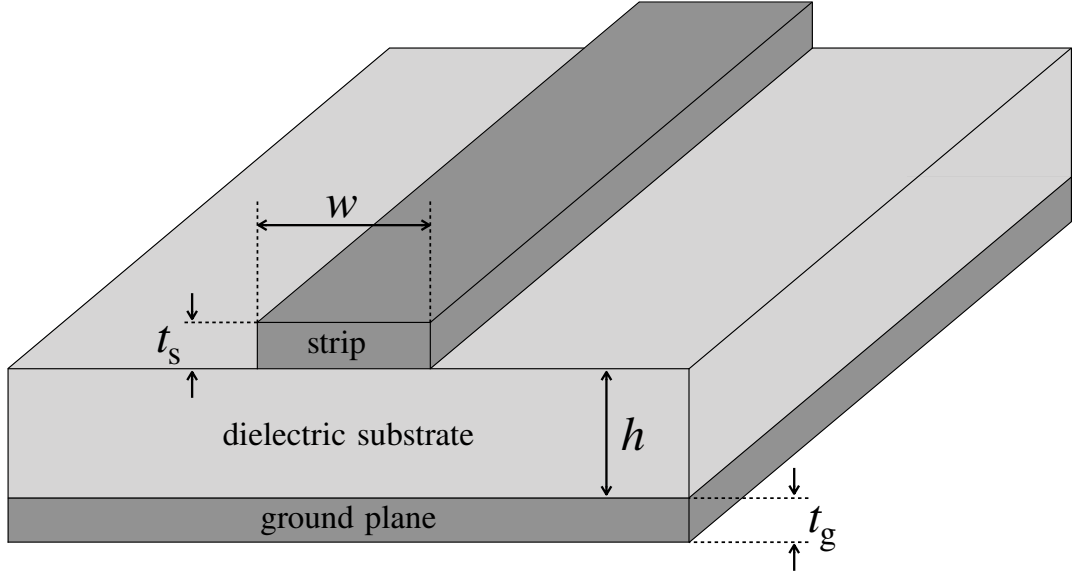


Figure B.1: Superconducting microstrip line structure having strip width w , strip thickness t_s , ground plane thickness t_g , and dielectric substrate thickness h .

$$r_b = q + \frac{p+1}{2} \ln D \quad (\text{for } u \geq 5) \quad (\text{B.3b})$$

$$D = \max(p, q) \quad (\text{B.3c})$$

$$p = 2(1 + t_h)^2 - 1 + \sqrt{\{2(1 + t_h)^2 - 1\}^2 - 1} \quad (\text{B.3d})$$

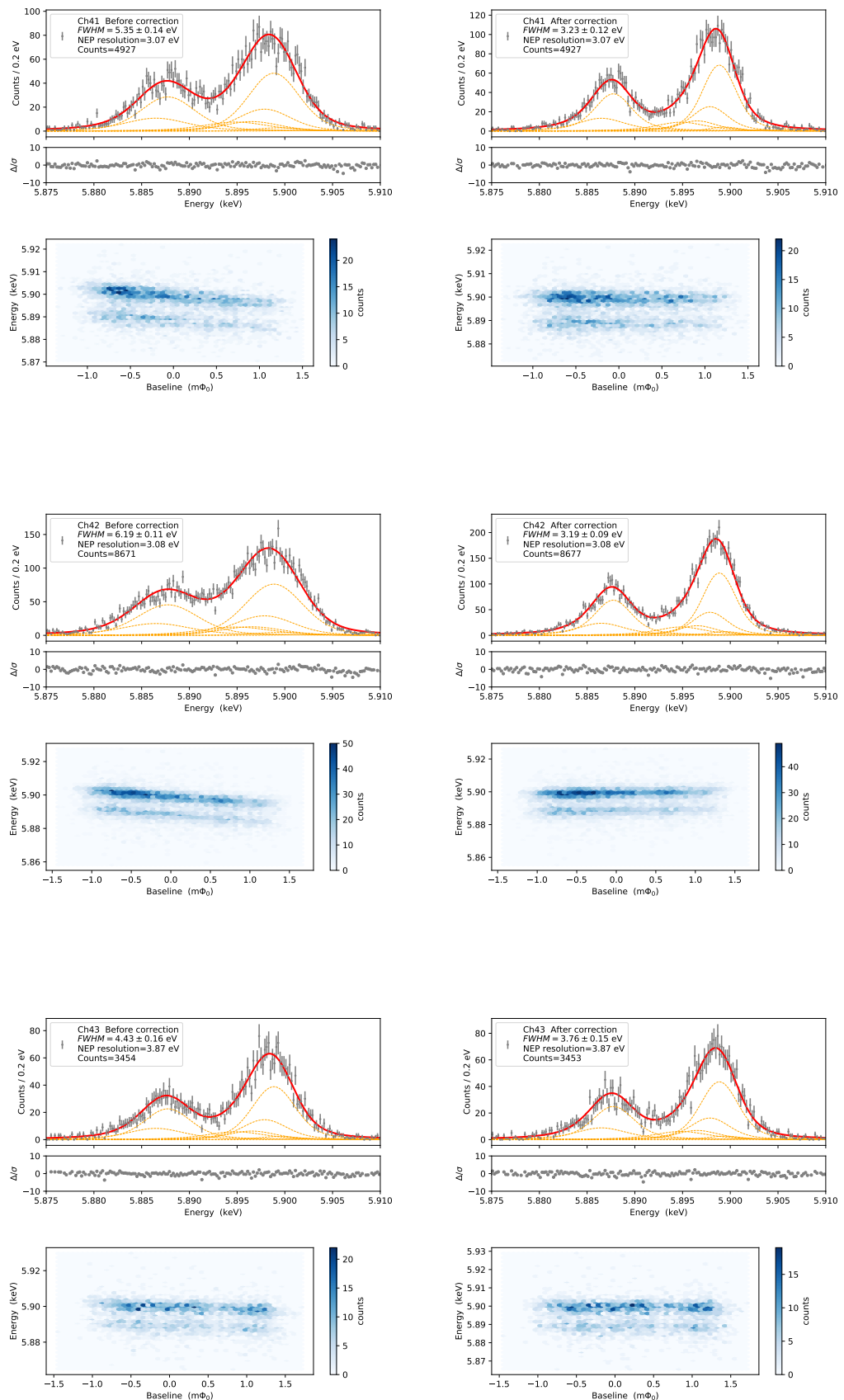
$$q = \frac{\pi u \sqrt{p}}{2} + \frac{p+1}{2} \left(1 + \ln \frac{4}{\sqrt{p}+1} \right) - \sqrt{p} \ln(\sqrt{p}+1) - \frac{(\sqrt{p}-1)^2}{2} \ln(\sqrt{p}-1). \quad (\text{B.3e})$$

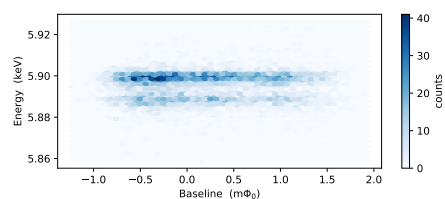
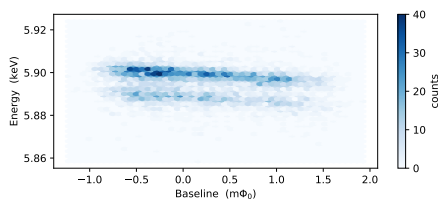
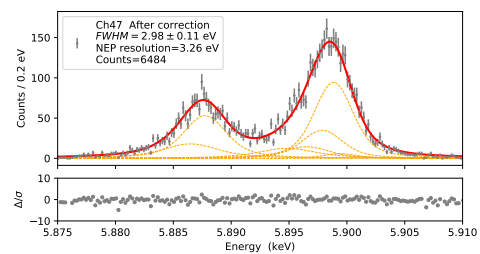
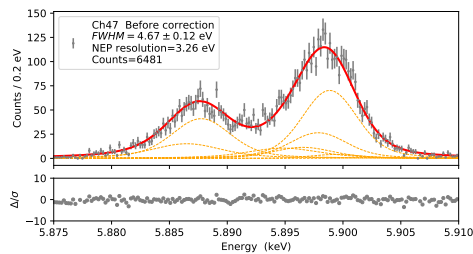
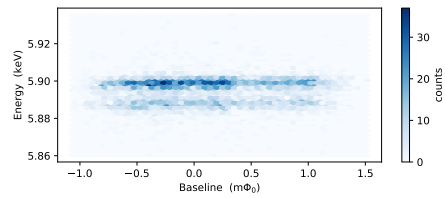
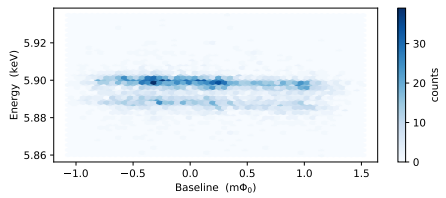
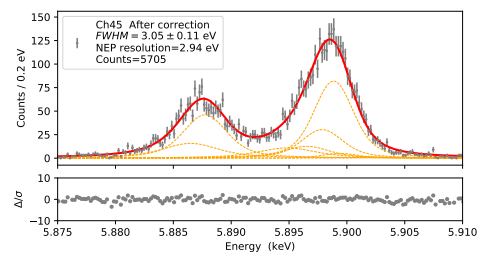
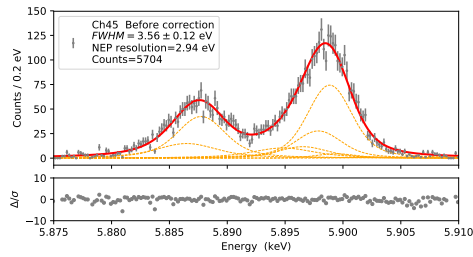
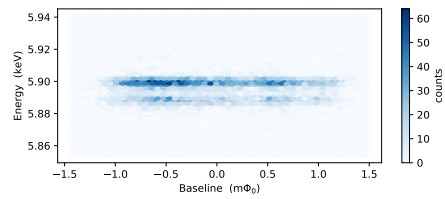
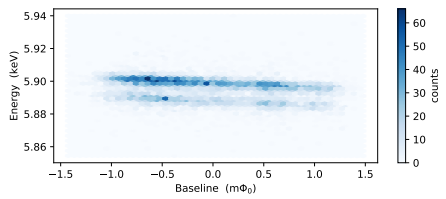
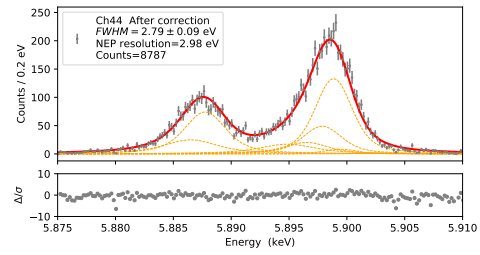
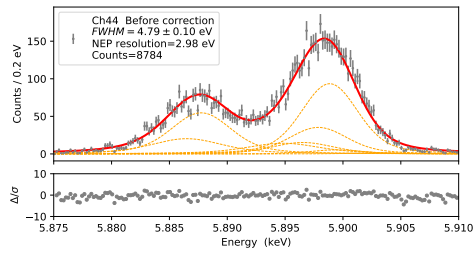
When $K \approx 1$, i.e. u is large, and $t_s, t_g \gg \lambda_L$, L_{MS} can be reduced to $L_{MS} \approx (h + 2\lambda_L) \mu_0/w$.

Appendix C

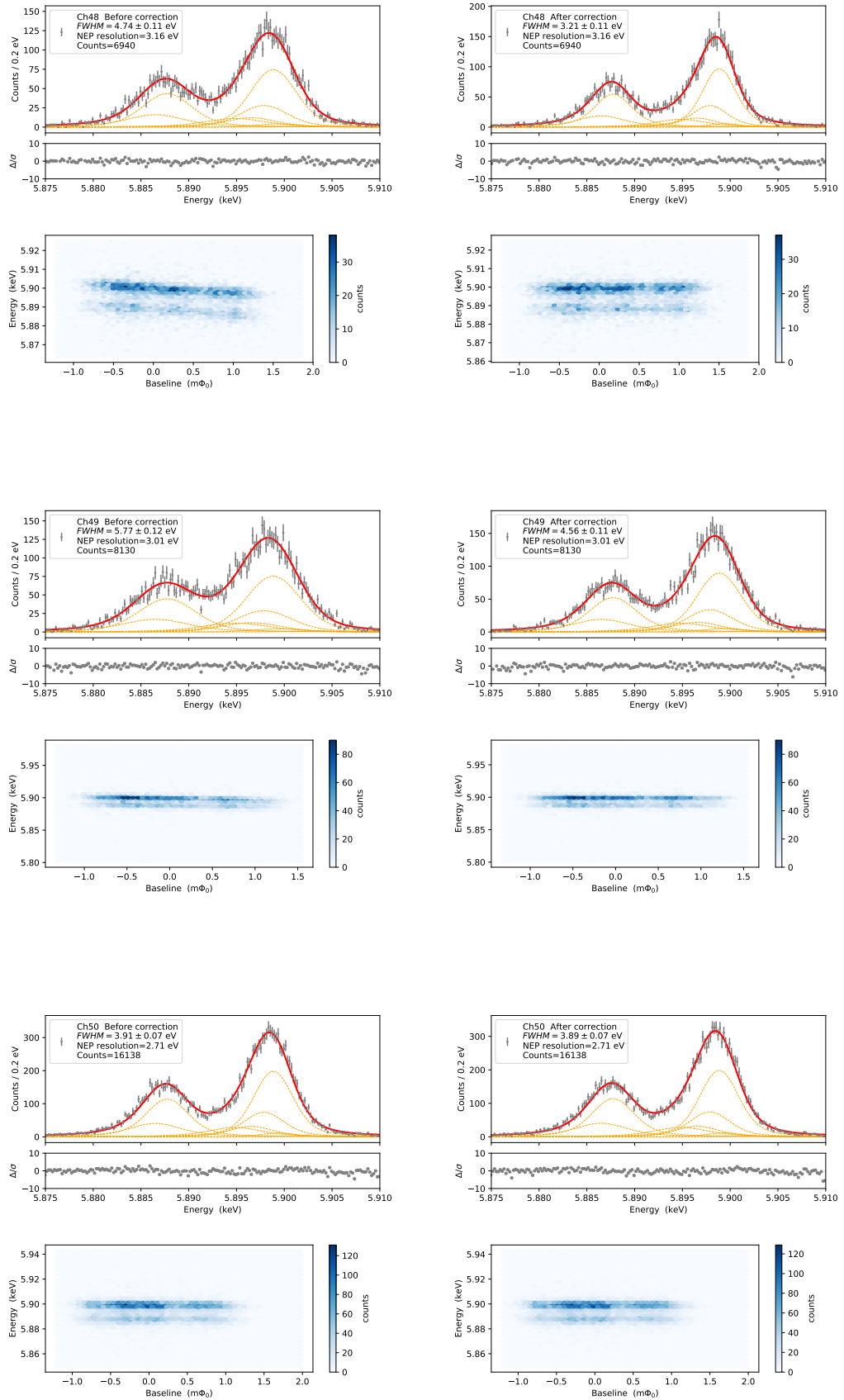
Energy Spectra and Gain-Drift Correlations of All 38 Pixels

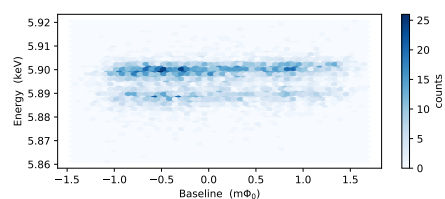
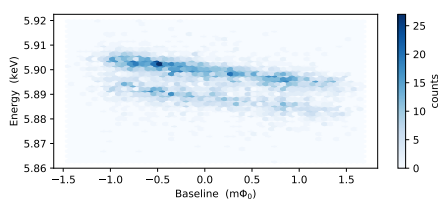
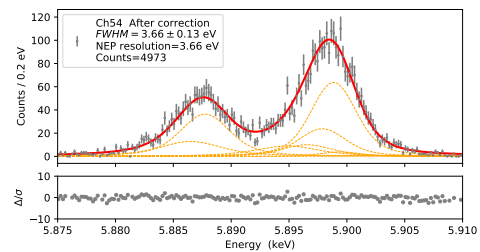
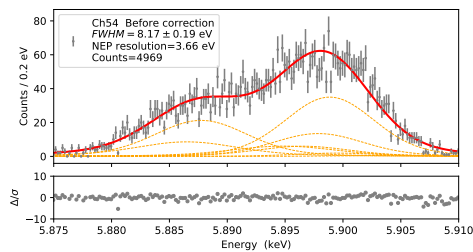
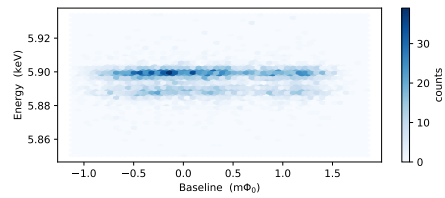
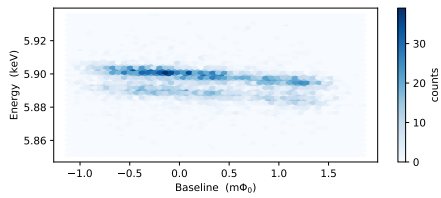
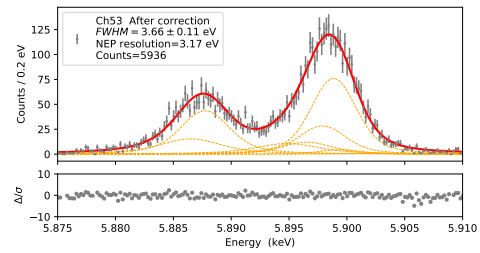
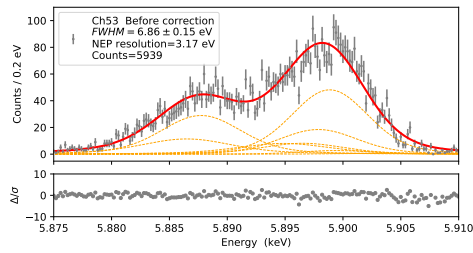
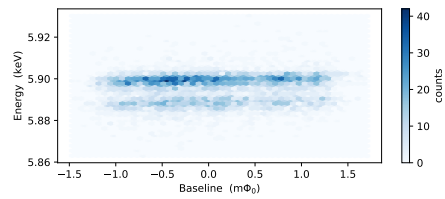
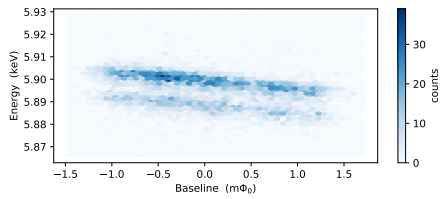
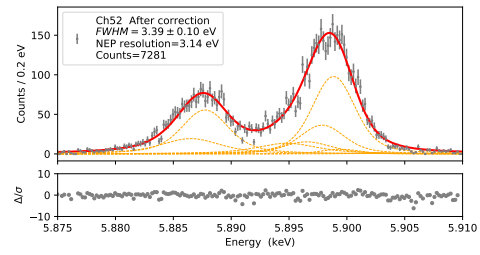
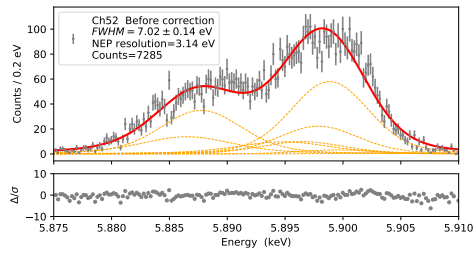
APPENDIX C. ENERGY SPECTRA AND GAIN-DRIFT CORRELATIONS OF ALL 38 PIXELS





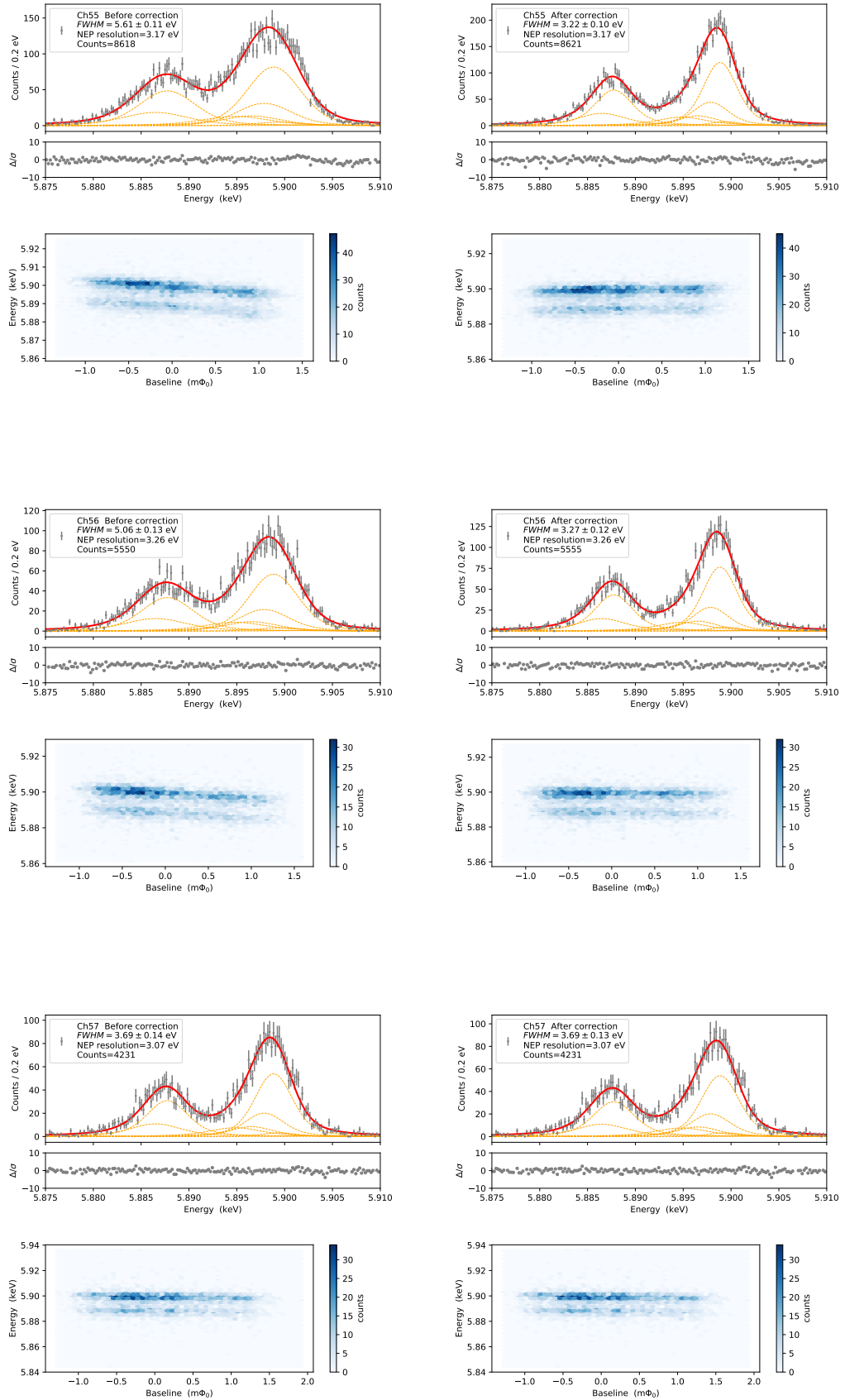
APPENDIX C. ENERGY SPECTRA AND GAIN-DRIFT CORRELATIONS OF ALL 38 PIXELS

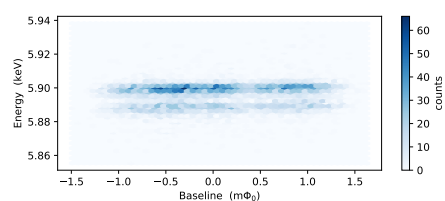
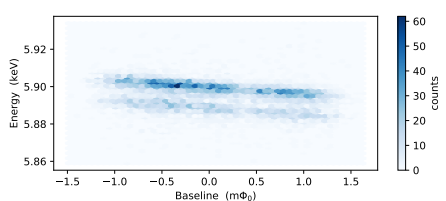
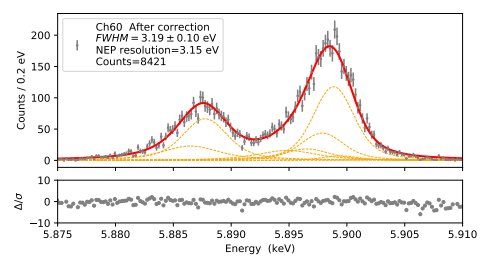
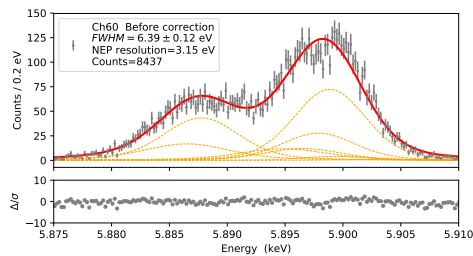
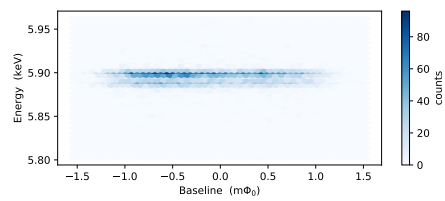
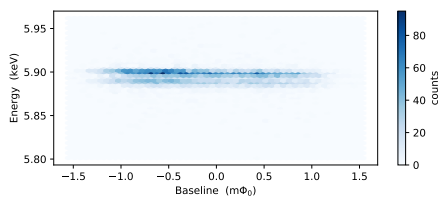
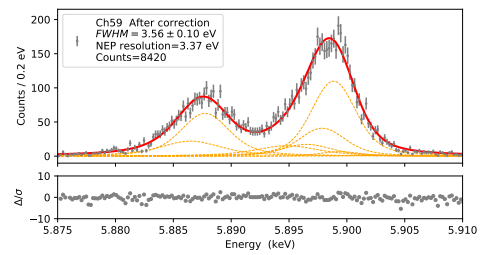
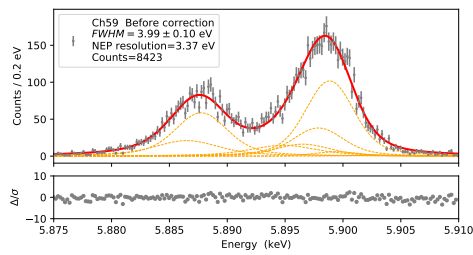
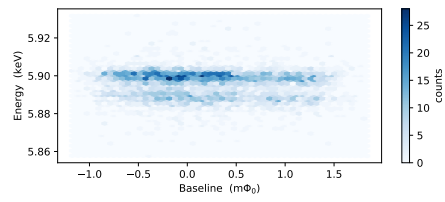
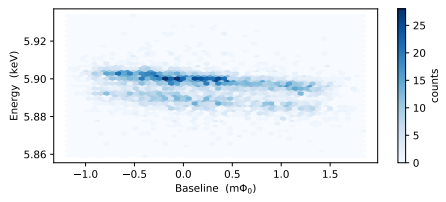
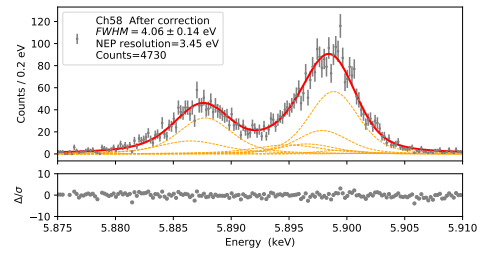
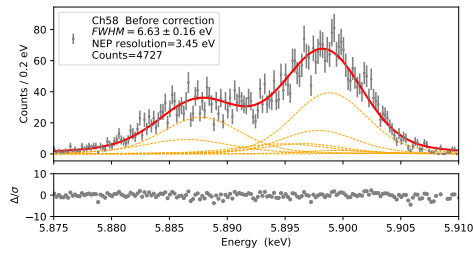




APPENDIX C. ENERGY SPECTRA AND GAIN-DRIFT CORRELATIONS
OF ALL 38 PIXELS

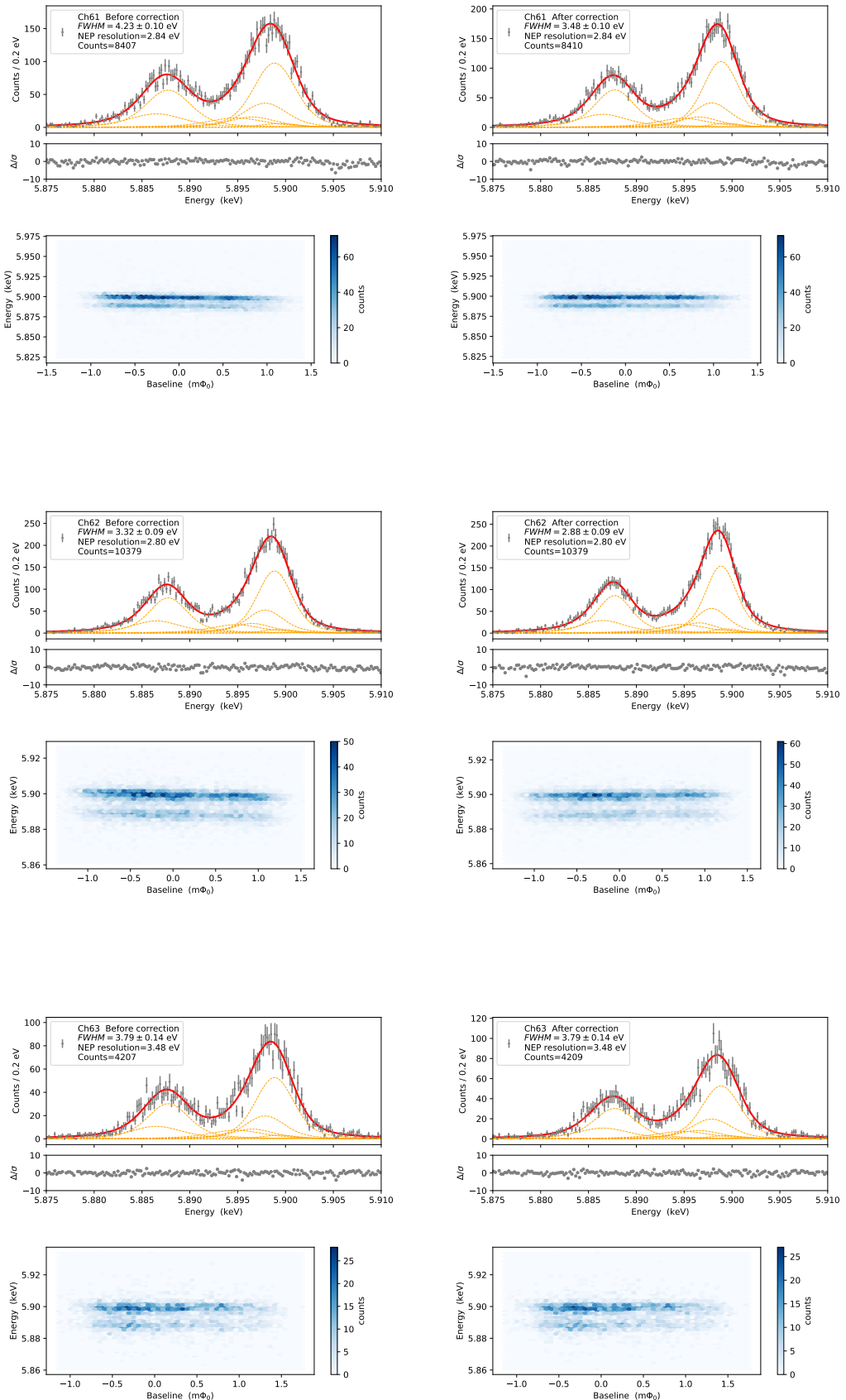
110

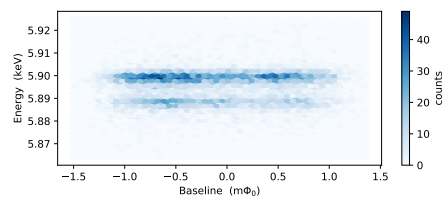
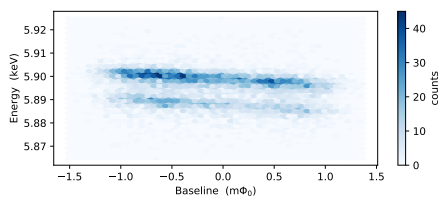
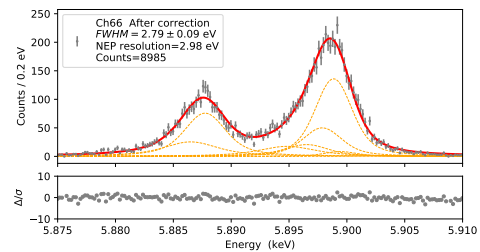
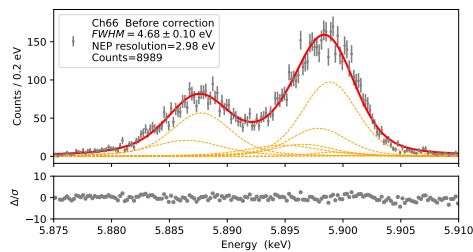
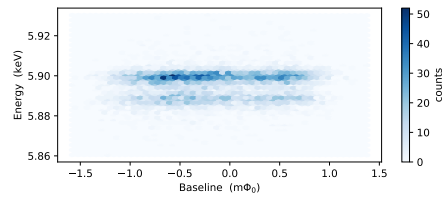
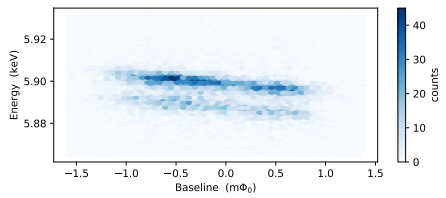
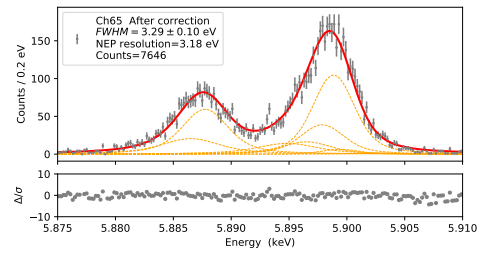
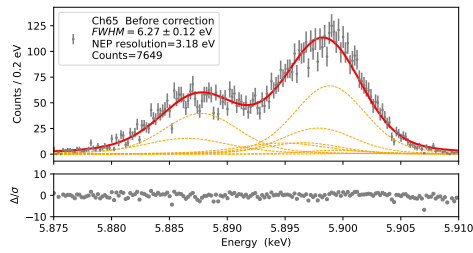
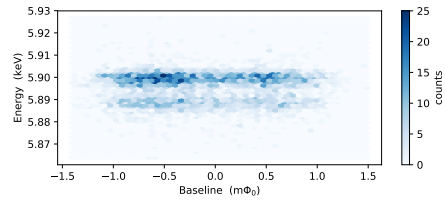
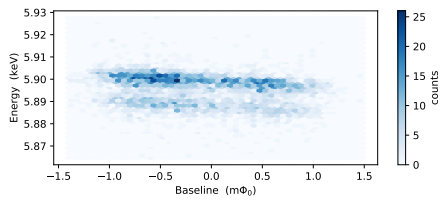
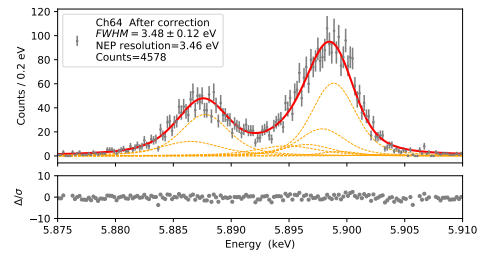
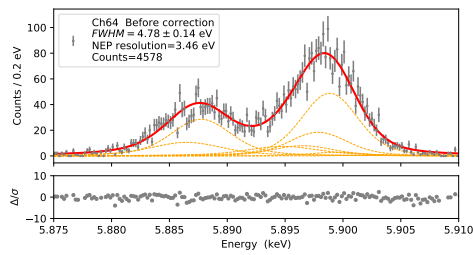




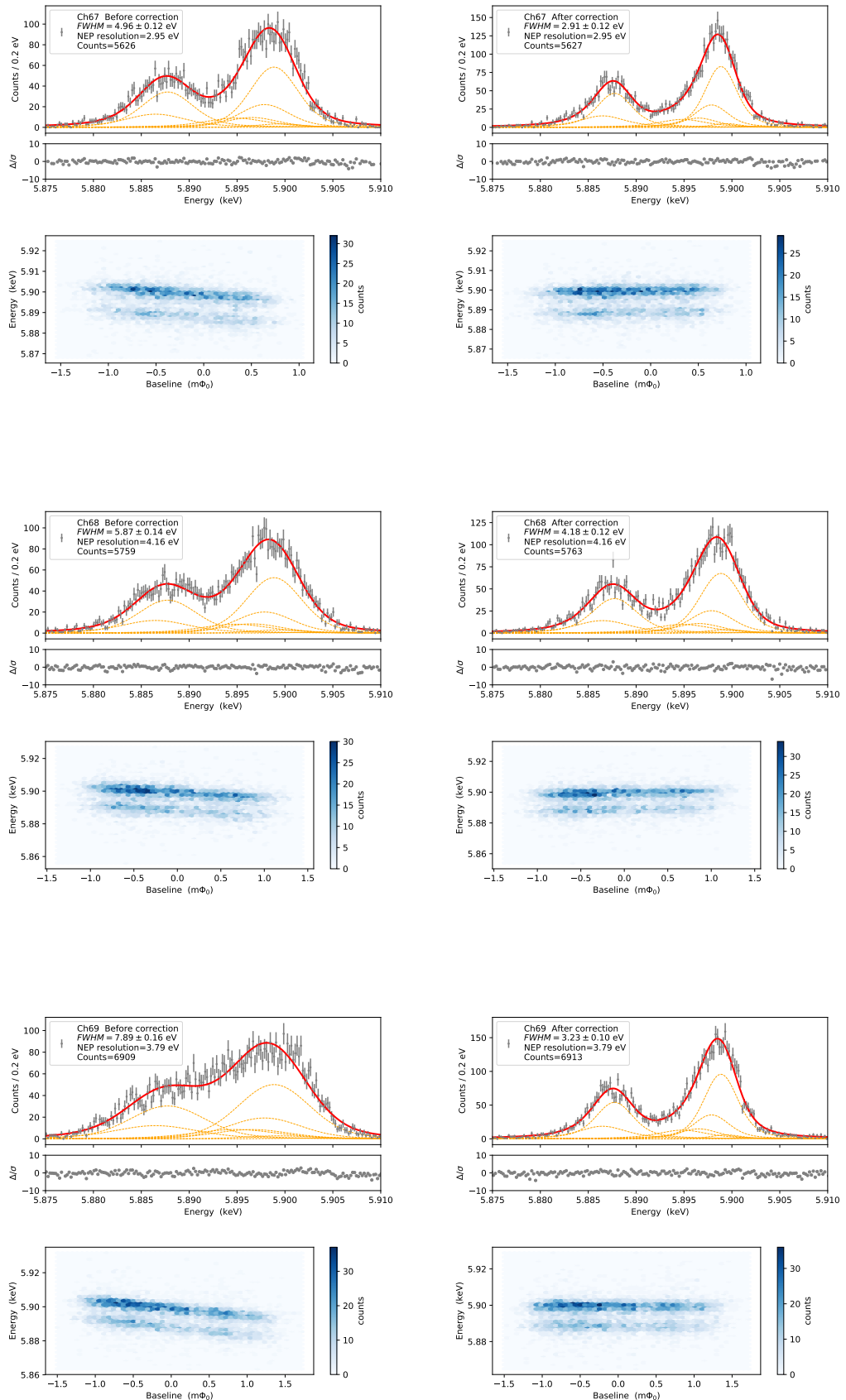
APPENDIX C. ENERGY SPECTRA AND GAIN-DRIFT CORRELATIONS OF ALL 38 PIXELS

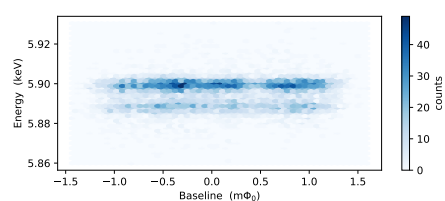
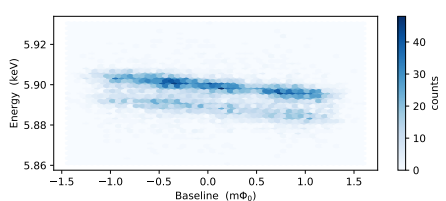
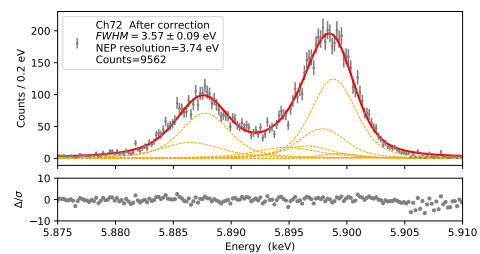
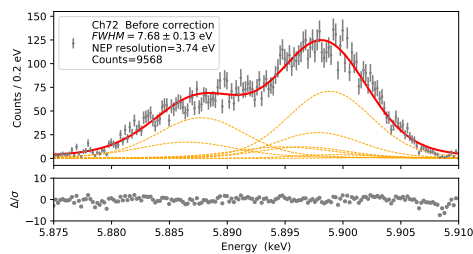
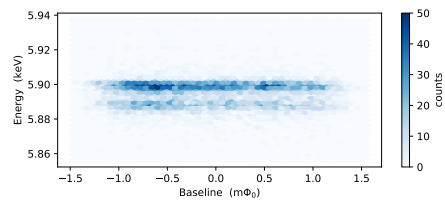
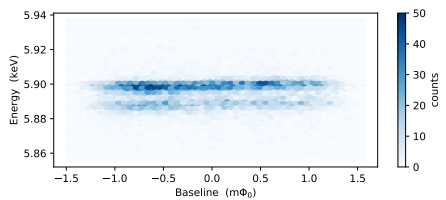
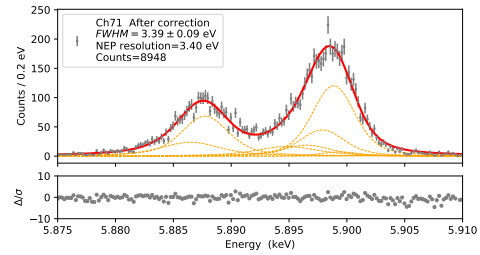
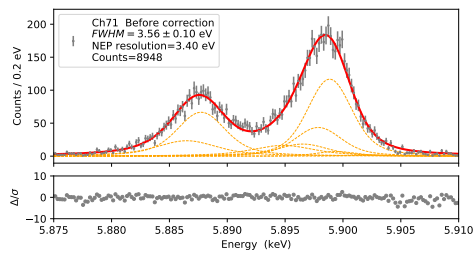
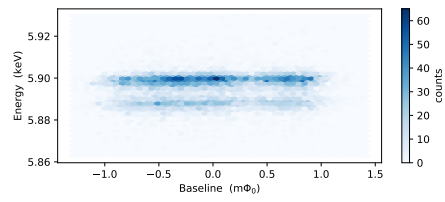
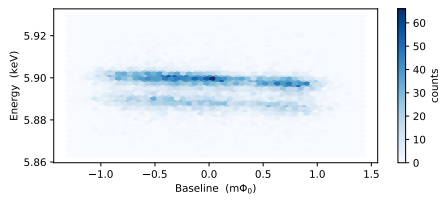
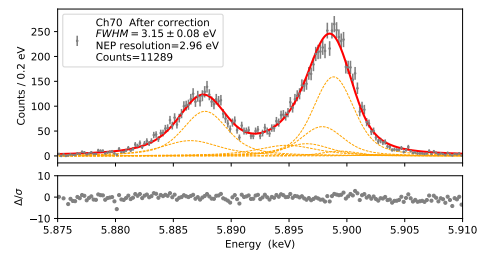
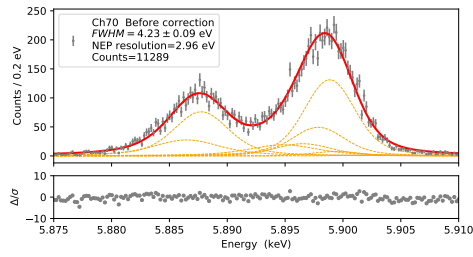
112





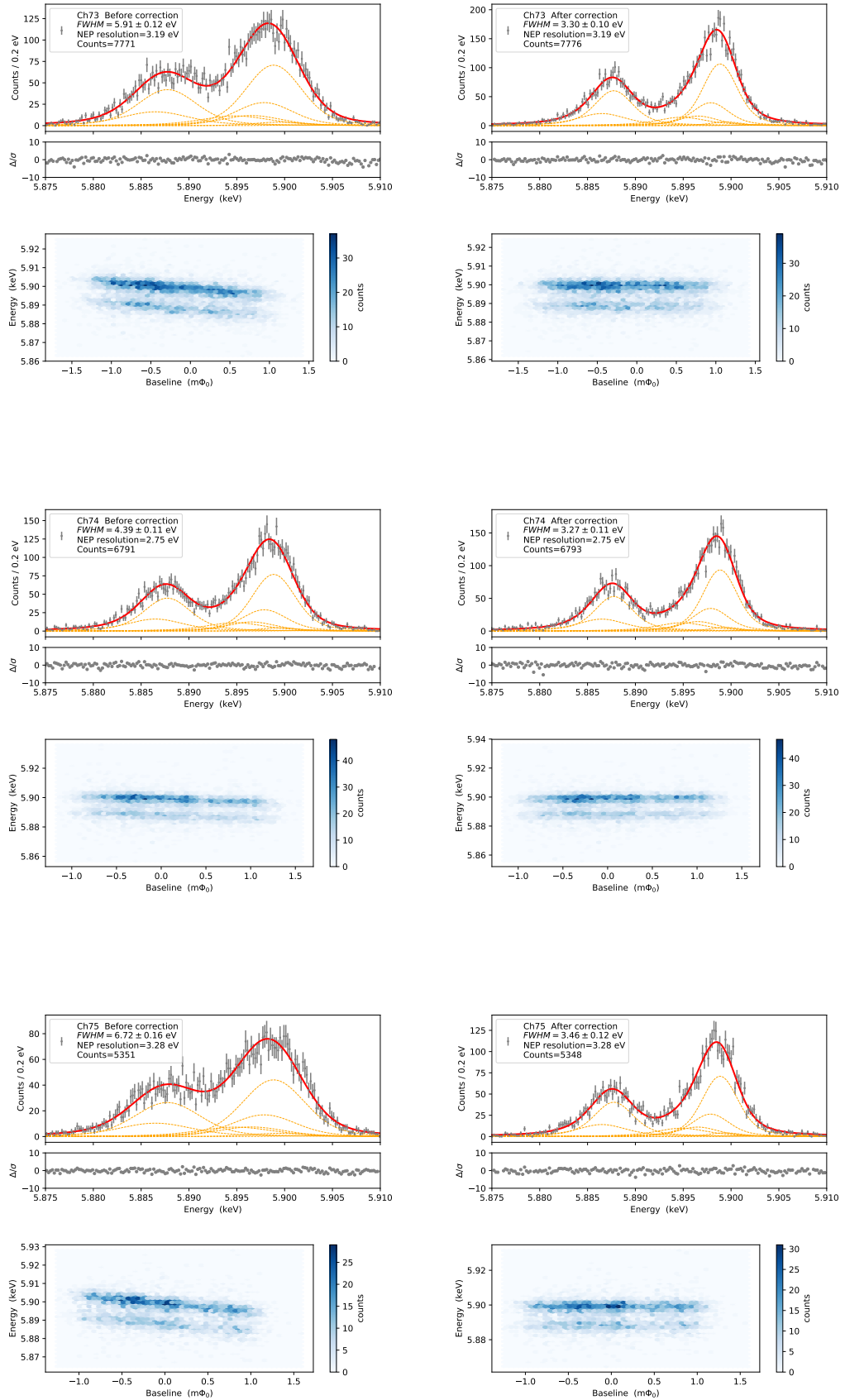
APPENDIX C. ENERGY SPECTRA AND GAIN-DRIFT CORRELATIONS OF ALL 38 PIXELS

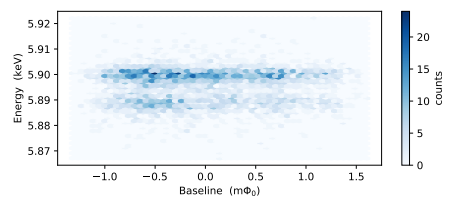
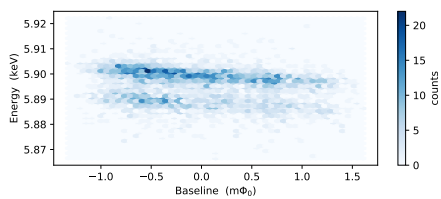
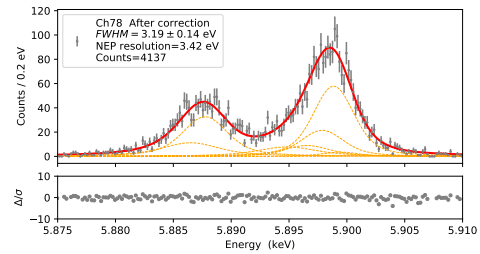
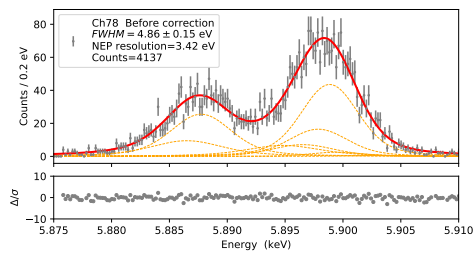
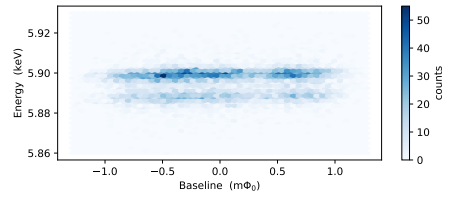
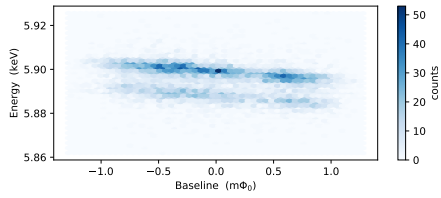
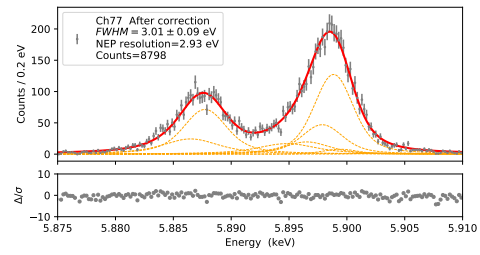
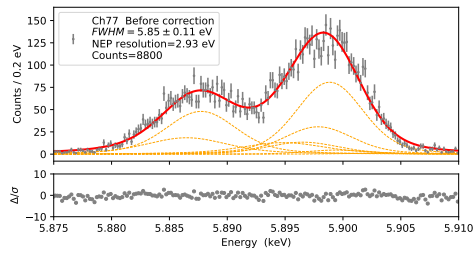
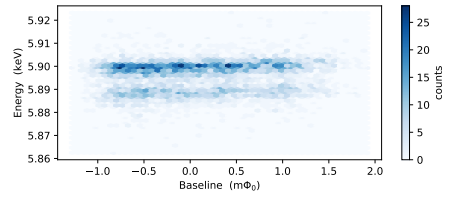
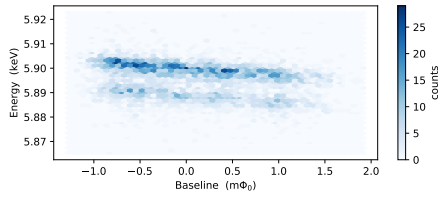
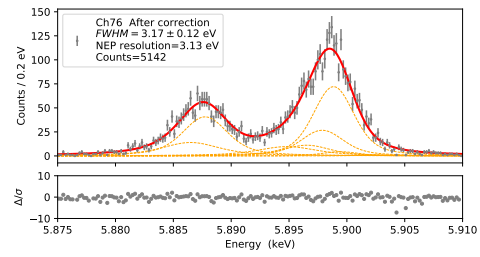
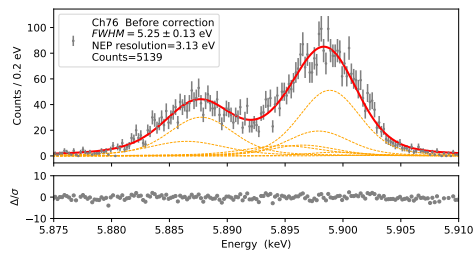




APPENDIX C. ENERGY SPECTRA AND GAIN-DRIFT CORRELATIONS OF ALL 38 PIXELS

116





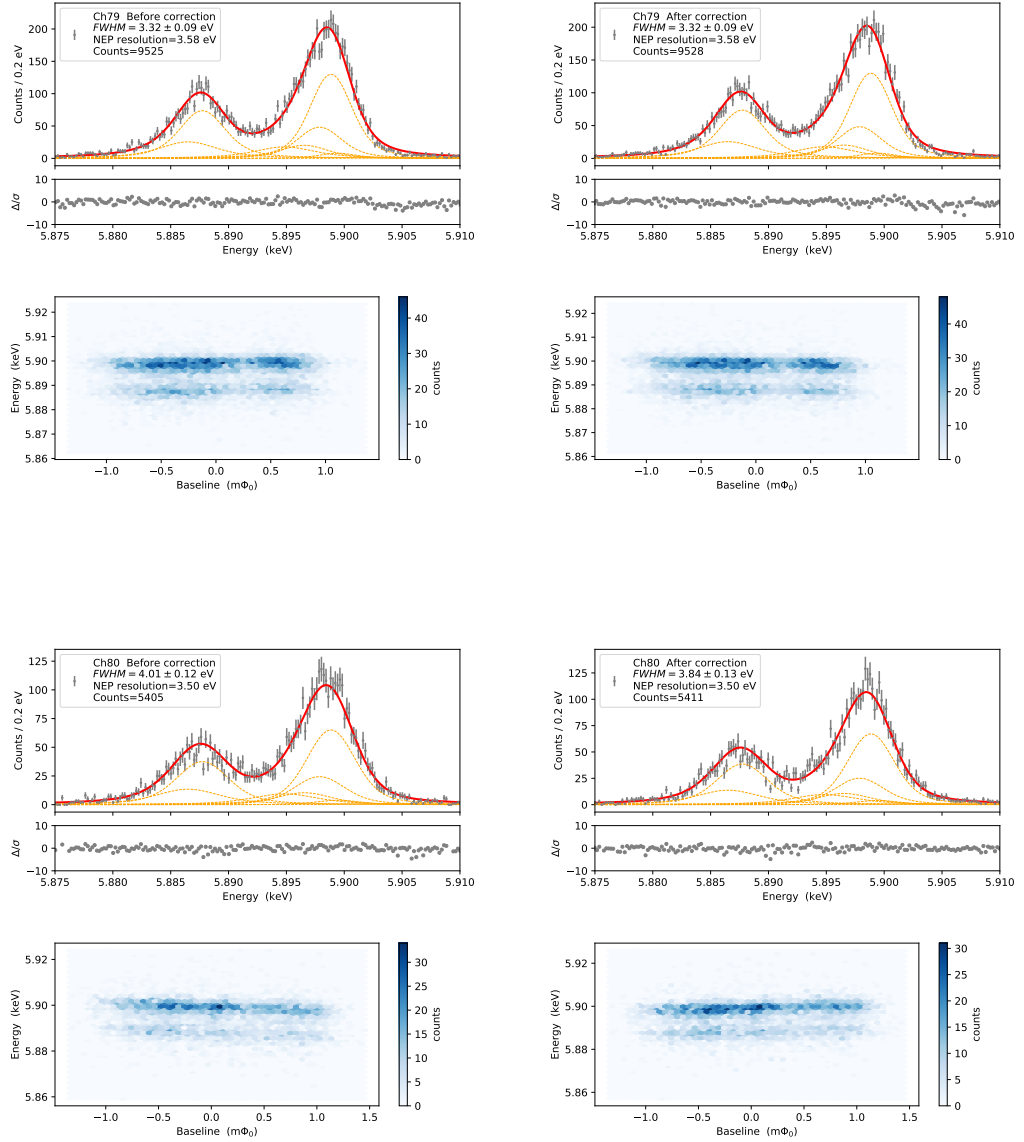


Figure C.1: Energy spectra (*upper panels*) and anti-correlations between energy and baseline (*lower panels*) of all 38 pixels. Those before/after application of the gain-drift correction are shown in the left/right columns.

Bibliography

- [1] Y. Tanaka and J. Bleeker. The diffuse soft X-ray sky - Astrophysics related to cosmic soft X-rays in the energy range 0.1-2.0 keV. *Space Science Reviews*, 20:815–888, 08 1977. <https://doi.org/10.1007/BF02431836>.
- [2] D. McCammon, R. Almy, E. Apodaca, W. Bergmann Tiest, W. Cui, S. Deiker, M. Galeazzi, M. Juda, A. Lesser, T. Mihara, J. P. Morgenthaler, W. T. Sanders, J. Zhang, E. Figueroa-Feliciano, R. L. Kelley, S. H. Moseley, R. F. Mushotzky, F. S. Porter, C. K. Stahle, and A. E. Szymkowiak. A High Spectral Resolution Observation of the Soft X-Ray Diffuse Background with Thermal Detectors. *The Astrophysical Journal*, 576(1):188–203, sep 2002. <https://doi.org/10.1086%2F341727>.
- [3] Ryuichi Fujimoto, Kazuhisa Mitsuda, Dan McCammon, Yoh Takei, Michael Bauer, Yoshitaka Ishisaki, F. Scott Porter, Hiroya Yamaguchi, Kiyoshi Hayashida, and Noriko Y. Yamasaki. Evidence for Solar-Wind Charge-Exchange X-Ray Emission from the Earth ’ s Magnetosheath. *Publications of the Astronomical Society of Japan*, 59(sp1):S133–S140, 01 2007. <https://doi.org/10.1093/pasj/59.sp1.S133>.
- [4] Masaki Numazawa, Yuichiro Ezoe, Kumi Ishikawa, Takaya Ohashi, Yoshizumi Miyoshi, Tomoki Kimura, Yasunobu Uchiyama, Daikou Shiota, and Graziella Branduardi-Raymont. Suzaku observation of Jupiter ’ s X-rays around solar maximum. *Publications of the Astronomical Society of Japan*, 71(5), 07 2019. <https://doi.org/10.1093/pasj/psz077>.
- [5] Anastasia Fialkov, Aviad Cohen, Rennan Barkana, and Joseph Silk. Constraining the redshifted 21-cm signal with the unresolved soft X-ray background. *Monthly Notices of the Royal Astronomical Society*, 464(3):3498–3508, 10 2016. <https://doi.org/10.1093/mnras/stw2540>.
- [6] Renyue Cen and Jeremiah P. Ostriker. Where Are the Baryons? *The Astrophysical Journal*, 514(1):1–6, mar 1999. <https://doi.org/10.1086%2F306949>.

- [7] Kohji Yoshikawa, Klaus Dolag, Yasushi Suto, Shin Sasaki, Noriko Y. Yamasaki, Takaya Ohashi, Kazuhisa Mitsuda, Yuzuru Tawara, Ryuichi Fujimoto, Tae Furusho, Akihiro Furuzawa, Manabu Ishida, Yoshitaka Ishisaki, and Yoh Takei. Locating the Warm–Hot Intergalactic Medium in the Simulated Local Universe. *Publications of the Astronomical Society of Japan*, 56(6):939–957, 12 2004. <https://doi.org/10.1093/pasj/56.6.939>.
- [8] Y. Takei, E. Ursino, E. Branchini, T. Ohashi, H. Kawahara, K. Mitsuda, L. Piro, A. Corsi, L. Amati, J. W. den Herder, M. Galeazzi, J. Kaastra, L. Moscardini, F. Nicastro, F. Paerels, M. Roncarelli, and M. Viel. STUDYING THE WARM-HOT INTERGALACTIC MEDIUM IN EMISSION. *The Astrophysical Journal*, 734(2):91, may 2011. <https://doi.org/10.1088>.
- [9] M. Fukugita, C. J. Hogan, and P. J. E. Peebles. The Cosmic Baryon Budget. *The Astrophysical Journal*, 503(2):518–530, aug 1998. <https://doi.org/10.1086%2F306025>.
- [10] Kazuhisa Mitsuda. Observational Signatures of the Warm-Hot Intergalactic Medium and X-ray Absorption Lines by the Halo of our Galaxy. *Chinese Journal of Astronomy and Astrophysics*, 3(S1):169–180, dec 2003. <https://doi.org/10.1088%2F1009-9271%2F3%2Fs1%2F169>.
- [11] K.D. Irwin and G.C. Hilton. *Transition-Edge Sensors*, pages 63–150. Springer Berlin Heidelberg, Berlin, Heidelberg, 2005. https://doi.org/10.1007/10933596_3.
- [12] Robert D. Horansky, Joel N. Ullom, James A. Beall, Gene C. Hilton, Kent D. Irwin, Donald E. Dry, Elizabeth P. Hastings, Stephen P. Lamont, Clifford R. Rudy, and Michael W. Rabin. Superconducting calorimetric alpha particle sensors for nuclear nonproliferation applications. *Applied Physics Letters*, 93(12):123504, 2008. <https://doi.org/10.1063/1.2978204>.
- [13] Kazuhisa Mitsuda. TES X-ray microcalorimeters for X-ray astronomy and material analysis. *Physica C: Superconductivity and its Applications*, 530:93–97, 2016. <https://doi.org/10.1016/j.physc.2016.03.018>.
- [14] HEATES Collaboration et al. First application of superconducting transition-edge sensor microcalorimeters to hadronic atom X-ray spectroscopy. *Progress of Theoretical and Experimental Physics*, 2016(9), 09 2016. <https://doi.org/10.1093/ptep/ptw130>.
- [15] Kazuki Niwa, Takayuki Numata, Kaori Hattori, and Daiji Fukuda. Few-photon color imaging using energy-dispersive superconducting transition-edge

- sensor spectrometry. *Scientific Reports*, 7(1):45660, 2017. <https://doi.org/10.1038/srep45660>.
- [16] A. Suzuki et al. The LiteBIRD Satellite Mission: Sub-Kelvin Instrument. *Journal of Low Temperature Physics*, 193(5):1048–1056, 2018. <https://doi.org/10.1007/s10909-018-1947-7>.
- [17] P. Khosropanah, B. Dirks, M. Parra-Borderías, M. Ridder, R. Hijmering, J. van der Kuur, L. Gottardi, M. Bruijn, M. Popescu, J. R. Gao, and H. Hoovers. Low-noise transition edge sensor (TES) for SAFARI instrument on SPICA. In Wayne S. Holland and Jonas Zmuidzinas, editors, *Millimeter, Submillimeter, and Far-Infrared Detectors and Instrumentation for Astronomy V*, volume 7741, pages 163 – 171. International Society for Optics and Photonics, SPIE, 2010. <https://doi.org/10.1117/12.857725>.
- [18] Didier Barret et al. *The Athena X-ray Integral Field Unit (X-IFU)*, volume 9905 of *Society of Photo-Optical Instrumentation Engineers (SPIE) Conference Series*, page 99052F. 2016. <https://ui.adsabs.harvard.edu/abs/2016SPIE.9905E..2FB>.
- [19] S. Yamada, T. Ohashi, Y. Ishisaki, Y. Ezoe, Y. Ichinohe, S. Kitazawa, K. Kosaka, R. Hayakawa, K. Nunomura, K. Mitsuda, N. Y. Yamasaki, T. Kikuchi, T. Hayashi, H. Muramatsu, Y. Nakashima, Y. Tawara, I. Mitsuishi, Y. Babazaki, D. Seki, K. Otsuka, M. Ishihara, K. Osato, N. Ota, M. Tomariguchi, D. Nagai, E. Lau, K. Sato, and the DIOS team. Super DIOS: Future X-ray Spectroscopic Mission to Search for Dark Baryons. *Journal of Low Temperature Physics*, 193(5):1016–1023, 2018. <https://doi.org/10.1007/s10909-018-1918-z>.
- [20] Simon R. Bandler, James A. Chervenak, Aaron M. Datesman, Archana M. Devasia, Michael J. DiPirro, Kazuhiro Sakai, Stephen J. Smith, Thomas R. Stevenson, Wonsik Yoon, Douglas A. Bennett, Benjamin Mates, Daniel S. Swetz, Joel N. Ullom, Kent D. Irwin, Megan E. Eckart, Enectali Figueroa-Feliciano, Dan McCammon, Kevin K. Ryu, Jeffrey R. Olson, and Ben Zeiger. Lynx x-ray microcalorimeter. *Journal of Astronomical Telescopes, Instruments, and Systems*, 5(2):1 – 29, 2019. <https://doi.org/10.1117/1.JATIS.5.2.021017>.
- [21] A. Simionescu et al. Voyage through the Hidden Physics of the Cosmic Web. https://www.cosmos.esa.int/documents/1866264/3219248/SimionescuA_Voyage2050_cosmicweb.pdf/5588490d-d8d5-dbdd-b594-e73d493c4205?t=1565184667443.

- [22] S. J. Smith, J. S. Adams, C. N. Bailey, S. R. Bandler, J. A. Chervenak, M. E. Eckart, F. M. Finkbeiner, R. L. Kelley, C. A. Kilbourne, F. S. Porter, and J. E. Sadleir. Small Pitch Transition-Edge Sensors with Broadband High Spectral Resolution for Solar Physics. *Journal of Low Temperature Physics*, 167(3):168–175, 2012. <https://doi.org/10.1007/s10909-012-0574-y>.
- [23] S. J. Lee, J. S. Adams, S. R. Bandler, J. A. Chervenak, M. E. Eckart, F. M. Finkbeiner, R. L. Kelley, C. A. Kilbourne, F. S. Porter, J. E. Sadleir, S. J. Smith, and E. J. Wassell. Fine pitch transition-edge sensor X-ray microcalorimeters with sub-eV energy resolution at 1.5 keV. *Applied Physics Letters*, 107(22):223503, 2015. <https://doi.org/10.1063/1.4936793>.
- [24] K. D. Irwin. An application of electrothermal feedback for high resolution cryogenic particle detection. *Applied Physics Letters*, 66(15):1998–2000, 1995. <https://doi.org/10.1063/1.113674>.
- [25] J. A. Chervenak, K. D. Irwin, E. N. Grossman, John M. Martinis, C. D. Reintsema, and M. E. Huber. Superconducting multiplexer for arrays of transition edge sensors. *Applied Physics Letters*, 74(26):4043–4045, 1999. <https://doi.org/10.1063/1.123255>.
- [26] K D Irwin, M D Niemack, J Beyer, H M Cho, W B Doriese, G C Hilton, C D Reintsema, D R Schmidt, J N Ullom, and L R Vale. Code-division multiplexing of superconducting transition-edge sensor arrays. *Superconductor Science and Technology*, 23(3):034004, feb 2010. <https://doi.org/10.1088/0953-2048/23/3/034004>.
- [27] Jongsoo Yoon, John Clarke, J. M. Gildemeister, Adrian T. Lee, M. J. Myers, P. L. Richards, and J. T. Skidmore. Single superconducting quantum interference device multiplexer for arrays of low-temperature sensors. *Applied Physics Letters*, 78(3):371–373, 2001. <https://doi.org/10.1063/1.1338963>.
- [28] Joel N Ullom and Douglas A Bennett. Review of superconducting transition-edge sensors for x-ray and gamma-ray spectroscopy. *Superconductor Science and Technology*, 28(8):084003, jul 2015. <https://doi.org/10.1088/0953-2048/28/8/084003>.
- [29] J.N. Ullom, W.B. Doriese, D.A. Fischer, J.W. Fowler, G.C. Hilton, C. Jaye, C.D. Reintsema, D.S. Swetz, and D.R. Schmidt. Transition-Edge Sensor Microcalorimeters for X-ray Beamline Science. *Synchrotron Radiation News*, 27(4):24–27, 2014. <https://doi.org/10.1080/08940886.2014.930806>.
- [30] K. M. Morgan, B. K. Alpert, D. A. Bennett, E. V. Denison, W. B. Doriese, J. W. Fowler, J. D. Gard, G. C. Hilton, K. D. Irwin, Y. I. Joe, G. C. O’Neil,

- C. D. Reintsema, D. R. Schmidt, J. N. Ullom, and D. S. Swetz. Code-division-multiplexed readout of large arrays of TES microcalorimeters. *Applied Physics Letters*, 109(11):112604, 2016. <https://doi.org/10.1063/1.4962636>.
- [31] Roland den Hartog, D. Boersma, M. Bruijn, B. Dirks, L. Gottardi, H. Hoeyers, R. Hou, M. Kiviranta, P. de Korte, J. van der Kuur, B. J. van Leeuwen, A. Nieuwenhuizen, and M. Popescu. Baseband Feedback for Frequency-Domain-Multiplexed Readout of TES X-ray Detectors. *AIP Conference Proceedings*, 1185(1):261–264, 2009. <https://aip.scitation.org/doi/abs/10.1063/1.3292328>.
- [32] K. D. Irwin and K. W. Lehnert. Microwave SQUID multiplexer. *Applied Physics Letters*, 85(11):2107–2109, 2004. <https://doi.org/10.1063/1.1791733>.
- [33] J. A. B. Mates, G. C. Hilton, K. D. Irwin, L. R. Vale, and K. W. Lehnert. Demonstration of a multiplexer of dissipationless superconducting quantum interference devices. *Applied Physics Letters*, 92(2):023514, 2008. <https://doi.org/10.1063/1.2803852>.
- [34] John Arthur Benson Mates. *The microwave SQUID multiplexer*. PhD thesis, University of Colorado, 2011.
- [35] J. A. B. Mates, K. D. Irwin, L. R. Vale, G. C. Hilton, J. Gao, and K. W. Lehnert. Flux-Ramp Modulation for SQUID Multiplexing. *Journal of Low Temperature Physics*, 167(5):707–712, Jun 2012. <https://doi.org/10.1007/s10909-012-0518-6>.
- [36] Peter K. Day, Henry G. LeDuc, Benjamin A. Mazin, Anastasios Vayonakis, and Jonas Zmuidzinas. A broadband superconducting detector suitable for use in large arrays. *Nature*, 425(6960):817–821, 2003. <https://doi.org/10.1038/nature02037>.
- [37] Bradley Dober and the others. Readout demonstration of 512 TES bolometers using a single microwave SQUID multiplexer (Conference Presentation). In Jonas Zmuidzinas and Jian-Rong Gao, editors, *Millimeter, Submillimeter, and Far-Infrared Detectors and Instrumentation for Astronomy IX*, volume 10708. International Society for Optics and Photonics, SPIE, 2018. <https://doi.org/10.1117/12.2314231>.
- [38] J. A. B. Mates, D. T. Becker, D. A. Bennett, B. J. Dober, J. D. Gard, J. P. Hays-Wehle, J. W. Fowler, G. C. Hilton, C. D. Reintsema, D. R. Schmidt, D. S. Swetz, L. R. Vale, and J. N. Ullom. Simultaneous readout of 128 X-ray

- and gamma-ray transition-edge microcalorimeters using microwave SQUID multiplexing. *Applied Physics Letters*, 111(6):062601, 2017. <https://doi.org/10.1063/1.4986222>.
- [39] F. Hirayama, S. Kohjiro, D. Fukuda, H. Yamamori, S. Nagasawa, and M. Hidaka. Microwave SQUID Multiplexer for TES Readout. *IEEE Transactions on Applied Superconductivity*, 23(3):2500405–2500405, June 2013. <https://doi.org/10.1109/TASC.2012.2237474>.
- [40] Irimatsugawa Tomoya. *Study on Gamma-ray Transition Edge Sensor Array Based on Microwave SQUID Multiplexer*. PhD thesis, University of Tokyo, 2018.
- [41] W. Yoon, J. S. Adams, S. R. Bandler, D. Becker, D. A. Bennett, J. A. Chervenak, A. M. Datesman, M. E. Eckart, F. M. Finkbeiner, J. W. Fowler, J. D. Gard, G. C. Hilton, R. L. Kelley, C. A. Kilbourne, J. A. B. Mates, A. R. Miniussi, S. H. Moseley, O. Noroozian, F. S. Porter, C. D. Reintsema, J. E. Sadleir, K. Sakai, S. J. Smith, T. R. Stevenson, D. S. Swetz, J. N. Ullom, L. R. Vale, N. A. Wakeham, E. J. Wassell, and E. J. Wollack. Toward Large Field-of-View High-Resolution X-ray Imaging Spectrometers: Microwave Multiplexed Readout of 28 TES Microcalorimeters. *Journal of Low Temperature Physics*, 193(3):258–266, 2018. <https://doi.org/10.1007/s10909-018-1917-0>.
- [42] C.G. Montgomery, R.H. Dicke, E.M. Purcell, and Massachusetts Institute of Technology. Radiation Laboratory. *Principles of Microwave Circuits*. Massachusetts Institute of Technology. Radiation Laboratory. Radiation Laboratory series. McGraw-Hill Book Company, 1948.
- [43] D.M. Pozar. *Microwave Engineering, 4th Edition*. Wiley, 2011.
- [44] T. Ohira and K. Araki. Active Q -Factor and Equilibrium Stability Formulation for Sinusoidal Oscillators. *IEEE Transactions on Circuits and Systems II: Express Briefs*, 54(9):810–814, Sep. 2007. <https://doi.org/10.1109/TCSII.2007.899952>.
- [45] Jiansong Gao. *The Physics of Superconducting Microwave Resonators*. PhD thesis, California Institute of Technology, 2008. <https://resolver.caltech.edu/CaltechETD:etd-06092008-235549>.
- [46] K. Kurokawa. Power Waves and the Scattering Matrix. *IEEE Transactions on Microwave Theory and Techniques*, 13(2):194–202, March 1965. <https://doi.org/10.1109/TMTT.1965.1125964>.

- [47] MS Khalil, MJA Stoutimore, FC Wellstood, and KD Osborn. An analysis method for asymmetric resonator transmission applied to superconducting devices. *Journal of Applied Physics*, 111(5):054510, 2012. <https://doi.org/10.1063/1.3692073>.
- [48] Chunqing Deng, Martin Otto, and Adrian Lupascu. An analysis method for transmission measurements of superconducting resonators with applications to quantum-regime dielectric-loss measurements. *Journal of Applied Physics*, 114:054504, 04 2013. <https://doi.org/10.1063/1.4817512>.
- [49] B.D. Josephson. Possible new effects in superconductive tunnelling. *Physics Letters*, 1(7):251–253, 1962. <http://www.sciencedirect.com/science/article/pii/0031916362913690>.
- [50] B.D. Josephson. Supercurrents through barriers. *Advances in Physics*, 14(56):419–451, 1965. <https://doi.org/10.1080/00018736500101091>.
- [51] John Clarke and Alex I Braginski. *The SQUID handbook*, volume 1. John Wiley & Sons, Ltd, 2005.
- [52] Yuki Nakashima, Fuminori Hirayama, Satoshi Kohjiro, Hirotake Yamamori, Shuichi Nagasawa, Noriko Y. Yamasaki, and Kazuhisa Mitsuda. Adjustable SQUID-resonator direct coupling in microwave SQUID multiplexer for TES microcalorimeter array. *IEICE Electronics Express*, 14(11):20170271–20170271, 2017. <https://doi.org/10.1587/elex.14.20170271>.
- [53] W. H. Chang. The inductance of a superconducting strip transmission line. *Journal of Applied Physics*, 50(12):8129–8134, 1979. <https://doi.org/10.1063/1.325953>.
- [54] Charles Kittel. *Introduction to Solid State Physics*. Wiley, 8 edition, 2004.
- [55] Y. Nakashima, F. Hirayama, S. Kohjiro, H. Yamamori, S. Nagasawa, A. Sato, T. Irimatsugawa, H. Muramatsu, T. Hayashi, N. Y. Yamasaki, and K. Mitsuda. Readout of X-ray Pulses from a Single-pixel TES Microcalorimeter with Microwave Multiplexer Based on SQUIDs Directly Coupled to Resonators. *Journal of Low Temperature Physics*, 193(3):618–625, Nov 2018. <https://doi.org/10.1007/s10909-018-2030-0>.
- [56] Muramatsu Haruka. *A spectroscopic study of 229-Th isomer using TES microcalorimeters*. PhD thesis, University of Tokyo, 2019.
- [57] A. Yamaguchi, H. Muramatsu, T. Hayashi, N. Yuasa, K. Nakamura, M. Takimoto, H. Haba, K. Konashi, M. Watanabe, H. Kikunaga, K. Maehata, N. Y.

- Yamasaki, and K. Mitsuda. Energy of the ^{229}Th Nuclear Clock Isomer Determined by Absolute γ -ray Energy Difference. *Phys. Rev. Lett.*, 123:222501, Nov 2019. <https://link.aps.org/doi/10.1103/PhysRevLett.123.222501>.
- [58] G. Hölzer, M. Fritsch, M. Deutsch, J. Härtwig, and E. Förster. $K\alpha_{1,2}$ and $K\beta_{1,3}$ x-ray emission lines of the $3d$ transition metals. *Phys. Rev. A*, 56:4554–4568, Dec 1997. <https://link.aps.org/doi/10.1103/PhysRevA.56.4554>.
- [59] H. Yoshitake, Y. Ezoe, T. Yoshino, K. Mukai, K. Ishikawa, K. Mitsuda, N. Y. Yamasaki, Y. Ishisaki, H. Akamatsu, R. Maeda, and T. Takano. Optimization of Structure of Large Format TES Arrays. *IEEE Transactions on Applied Superconductivity*, 19(3):456–459, June 2009. <https://doi.org/10.1109/TASC.2009.2019227>.
- [60] K. Enpuku and K. Yoshida. Modeling the dc superconducting quantum interference device coupled to the multiturn input coil. *Journal of Applied Physics*, 69(10):7295–7300, 1991. <https://doi.org/10.1063/1.347576>.
- [61] K. Enpuku, R. Cantor, and H. Koch. Modeling the direct current superconducting quantum interference device coupled to the multiturn input coil. II. *Journal of Applied Physics*, 71(5):2338–2346, 12 1992. <https://doi.org/10.1063/1.351353>.
- [62] K. Enpuku, R. Cantor, and H. Koch. Modeling the dc superconducting quantum interference device coupled to the multiturn input coil. III. *Journal of Applied Physics*, 72(3):1000–1006, 1992. <https://doi.org/10.1063/1.351824>.
- [63] S. Kohjiro, N. Simizu, S. Kiryu, N. Chiba, and M. Koyanagi. Study of current peaks in DC SQUID with integrated coupling coil. *IEEE Transactions on Applied Superconductivity*, 3(1):1853–1857, March 1993. <https://doi.org/10.1109/77.233320>.
- [64] J. Jaycox and M. Ketchen. Planar coupling scheme for ultra low noise DC SQUIDS. *IEEE Transactions on Magnetics*, 17(1):400–403, January 1981. <https://doi.org/10.1109/TMAG.1981.1060902>.
- [65] Y. Nakashima, F. Hirayama, S. Kohjiro, H. Yamamori, S. Nagasawa, A. Sato, N. Y. Yamasaki, and K. Mitsuda. Investigation of Large Coupling Between TES X-Ray Microcalorimeter and Microwave Multiplexer Based on Microstrip SQUID. *IEEE Transactions on Applied Superconductivity*, 29(5):1–5, Aug 2019. <https://doi.org/10.1109/TASC.2019.2905688>.

- [66] Kenji Hinode, Shuichi Nagasawa, Masao Sugita, Tetsuro Satoh, Hiroyuki Akaike, Yoshihiro Kitagawa, and Mutsuo Hidaka. Pattern-size-free planarization for multilayered large-scale SFQ circuits. *IEICE transactions on electronics*, 86(12):2511–2513, 2003.
- [67] Shuichi Nagasawa, Kenji Hinode, Masao Sugita, Tetsuro Satoh, Hiroyuki Akaike, Yoshihiro Kitagawa, and Mutsuo Hidaka. Planarized multi-layer fabrication technology for LTS large-scale SFQ circuits. *Superconductor Science and Technology*, 16(12):1483–1486, nov 2003. <https://doi.org/10.1088/2F0953-2048/16/12/2F036>.
- [68] T. Irimatsugawa, H. Yamamori, F. Hirayama, S. Nagasawa, G. Fujii, S. Kohjiro, A. Sato, D. Fukuda, M. Hidaka, Y. Sato, M. Ohno, and H. Takahashi. Degradation of Quality Factor of Superconducting Resonators by Remaining Metallic Film and Improved Fabrication Process Using Caldera Planarization. *IEEE Transactions on Applied Superconductivity*, 29(5):1–6, Aug 2019. <https://doi.org/10.1109/TASC.2019.2905144>.
- [69] Jukka Knuutila, Seppo Ahlfors, Antti Ahonen, Jari Hällström, Matti Kajola, Olli V. Lounasmaa, Visa Vilkmán, and Claudia Tesche. Large- area low-noise seven- channel dc SQUID magnetometer for brain research. *Review of Scientific Instruments*, 58(11):2145–2156, 1987. <https://doi.org/10.1063/1.1139478>.
- [70] Satoshi Kohjiro, Fuminori Hirayama, Hirotake Yamamori, Shuichi Nagasawa, Daiji Fukuda, and Mutsuo Hidaka. White noise of Nb-based microwave superconducting quantum interference device multiplexers with NbN coplanar resonators for readout of transition edge sensors. *Journal of Applied Physics*, 115(22):223902, 2014. <https://doi.org/10.1063/1.4882118>.
- [71] Jiansong Gao, Jonas Zmuidzinas, Benjamin A. Mazin, Henry G. LeDuc, and Peter K. Day. Noise properties of superconducting coplanar waveguide microwave resonators. *Applied Physics Letters*, 90(10):102507, 2007. <https://doi.org/10.1063/1.2711770>.
- [72] K. Nagayoshi, M. L. Ridder, M. P. Bruijn, L. Gottardi, E. Taralli, P. Khosropanah, H. Akamatsu, S. Visser, and J.-R. Gao. Development of a Ti/Au TES Microcalorimeter Array as a Backup Sensor for the Athena/X-IFU Instrument. *Journal of Low Temperature Physics*, Dec 2019. <https://doi.org/10.1007/s10909-019-02282-8>.
- [73] E. Taralli, L. Gottardi, K. Nagayoshi, M. Ridder, S. Visser, P. Khosropanah, H. Akamatsu, J. van der Kuur, M. Bruijn, and J. R. Gao. Characterization of

- High Aspect-Ratio TiAu TES X-ray Microcalorimeter Array Under AC Bias. *Journal of Low Temperature Physics*, Nov 2019. <https://doi.org/10.1007/s10909-019-02254-y>.
- [74] Y. Ishisaki, H. Kurabayashi, A. Hoshino, T. Ohashi, T. Yoshino, T. Hagihara, K. Mitsuda, and K. Tanaka. Effect of On-Chip Magnetic Shielding for TES Microcalorimeters. *Journal of Low Temperature Physics*, 151(1):131–137, Apr 2008. <https://doi.org/10.1007/s10909-007-9628-y>.
- [75] A. E. Szymkowiak, R. L. Kelley, S. H. Moseley, and C. K. Stahle. Signal processing for microcalorimeters. *Journal of Low Temperature Physics*, 93(3):281–285, Nov 1993. <https://doi.org/10.1007/BF00693433>.
- [76] J. W. Fowler, B. K. Alpert, W. B. Doriese, Y. I. Joe, G. C. O'Neil, J. N. Ullom, and D. S. Swetz. The Practice of Pulse Processing. *Journal of Low Temperature Physics*, 184(1):374–381, Jul 2016. <https://doi.org/10.1007/s10909-015-1380-0>.
- [77] Thien Lam Trong. X-IFU technical challenge. In Jan-Willem A. den Herder, Tadayuki Takahashi, and Marshall Bautz, editors, *Space Telescopes and Instrumentation 2016: Ultraviolet to Gamma Ray*, volume 9905, pages 755 – 771. International Society for Optics and Photonics, SPIE, 2016. <https://doi.org/10.1117/12.2233634>.